UNIVERSIDAD AUTNOMA DE SAN LUIS POTOSÍ

FACULTAD DE CIENCIAS

"Study of Charge Accumulation and Kinetic Reactions on Copper Electrodes Surfaces by Electrochemical and Optical Polarization Techniques"

TESIS

PARA OBTENER EL GRADO DE

DOCTOR EN CIENCIAS APLICADAS

PRESENTA:

M.C. Saúl Vázquez Miranda

DIRECTORES DE TESIS:

Dr. Raúl E. Balderas Navarro

Dr. Christoph Cobet

San Luis Potosí, S.L.P. Junio 2020

Abstract

Understanding surface and interface processes at the atomic level occurring in metals with a crystalline structure are of scientific and technological relevances. Especially in electrochemical environments, metal surfaces play a crucial role whose primary interest lies in the physical-chemical phenomena fundamentals. Moreover, a precise knowledge of atomically controlled interfaces can be extended to cases stemming from amorphous or polycrystalline composites as in the majority of industrial applications; such as in renewable energies, pharmaceuticals, and petrochemical, to name a few. The study undertaken in this thesis tackles fundamental issues on the electronic processes taking place in both copper (110) and (111) surfaces in electrochemical environments based on hydrochloric acid (HCl) and the forming Helmholtz double layer.

This study was carried out using two linear optical spectroscopies, namely reflectance anisotropy (RAS-RDS) and ellipsometry (SE), both operating *in-situ* and real-time and in the spectroscopic mode as well. Simultaneously, measurements based on cyclic voltammetry (CV), electrochemical impedance spectroscopy (EIS) and chrono-amperometry (CA) were also performed. Clear correlations were found among the aforementioned techniques.

The outline can be summarized as i) in-depth adsorbate Frumkin (Flori-Huggins) isotherm analysis by RAS on Cu (110) in HCl, (ii) observation of HCl-induced surface states at different potentials and their correlation with electrochemical scanning tunneling microscopy (EC-STM), and (iii) a study regarding the evolution of Cl^- adsorption process using CA and SE, for both (111) and (110) surfaces.

This thesis reports for the first time, at least for the authors knowledge, a systematic optical and electrochemical study of Cu(110) and Cu(111) with several experimental tools, rendering RAS and SE as complementary probes for analytical studies in electrochemical processes.

Declaración

Yo, ***Saúl Vázquez Miranda***, estudiante del Posgrado en Ciencias Aplicadas de la Facultad de Ciencias de la Universidad Autnoma de San Luis Potosí, como autor de la tesis con nombre ***Study of Charge Accumulation and Kinetic Reactions on Copper Electrodes Surfaces by Electrochemical and Optical Polarization Techniques***, declaro que la tesis es una obra original, inédita, auténtica, personal, que se han citado las fuentes correspondientes y que en su ejecucin se respetaron las disposiciones legales vigentes que protegen los derechos de autor y de propiedad intelectual e industrial. Las ideas, doctrinas, resultados y conclusiones a los que he llegado son de mi absoluta responsabilidad.

Declaration

I, ***Saúl Vázquez Miranda***, student of the graduate program in Applied Sciences of the Faculty of Sciences in the Universidad Autonoma de San Luis Potosí, as author of the thesis entitled ***Study of Charge Accumulation and Kinetic Reactions on Copper Electrodes Surfaces by Electrochemical and Optical Polarization Techniques***, I hereby declare that this thesis is an original, undistributed, authentic, personal work for which the corresponding sources have been cited appropriately and that in their execution the legal provisions were respected that protect copyright, intellectual and industrial property. The ideas, doctrines, results and conclusions that I have reached are of my absolute responsibility.

Contents

1 Introduction

1.1 General Considerations and Goals

The transfer of electric charges between molecules, cations or anions in chemical solution is encountered in many relevant industrial processes such as electrolysis, corrosion, energy storage and conversion. For instance, important applications are found in novel electrodes used in fuel cells, dye cells, and electrolyte cells. Moreover, with increasing demands for sustainable development, the hydrogen production through splitting of water and other liquids complexes is an important way to relieve the global energy and environmental crisis. Recently, non invasive optical techniques have been of primordial importance in assessing the complex evolution in electro chemistry. Therefore, surface sensitive, non-invasive, experimental techniques are required in order to shed light the role the metallic surfaces have on the associated electrochemical reactions in a microscopic scale.

The main goal of this thesis relies on the optical response investigated by means of reflectance anisotropy spectroscopy (RAS/RDS) and spectroscopic ellipsometry (SE). We focus on both RAS and SE because these optical probes can be applied in ultra high vacuum (UHV) as well as in aqueous environments, and are able to detect surface states and their modification [1], anisotropic bulk strain [2, 3, 4], interface electric fields [5, 6], and is also possible to detect material variations with sub-monolayer sensitivity [7]. It shall be mentioned here that RAS provides a signature of the optical response of a static surface; *i.e.*, without changing the surface conditions.

Specifically, in this thesis the existence of modified surface states (SSs) is thoroughly investigated in aqueous environments; *e.g.*, by the electrochemically-induced surface reactivity enhancement near the surface-liquid (HCl) layer, and the corresponding modification of both, surface and electronic states, of the host metal (Copper single crystals in our case).

Because electrode reactions take place at the liquid solid interface, the related charge transfer needs to be understood first [8]. Despite the extremely high surface sensitivity of electron spectroscopy techniques like scanning Auger electron spectroscopy (SAES), X-ray photoelectron spectroscopy (XPS) [9], or electron diffraction (LEED, RHEED), these techniques cannot be used for in-situ electrochemical process monitoring or control. Optical probes are usually non-destructive and can be used in any environment.

Historically, RAS was the first technique which could show the presence of dimers in a low pressure metal-organic environment by comparing the resulting spectra to the ones obtained in UHV [10]. Similarly, we want to address questions regarding the existence and evolution of electronic surface states in aqueous environments, and their possible suppression or enhancement by varying external parameters; specifically the applied potential. For instance, Ref. [11] discusses the use of RAS for GaAs(001) wet etching, Ref. [12] reports GaAs dimers at the interface between GaAs and sodium sulphide liquid solutions and the two most recent reports [13, 14], are by the group of Weightman (Univ. Liverpool) on

Au(110) surfaces and protein adsorbates thereon. Within this thesis RAS and SE are operated in the photon energy range from 1 to 5.5 eV. In this energy range the penetration depth of light in water and HCl is >1 m. In the following, the main characteristics of the Cu surfaces are addressed remarking their role in our experiment, as their capability for charge transfer. Specifically, both Cu (110) and Cu(111) are considered.

1.2 Low-index Copper single crystals (111) and (110)

Fig. 1.1 depicts the ideal Cu(110), Cu(110) and Cu(111) surfaces without any reconstruction. Copper is a chemical element with atomic number 29, its electronic configuration is [Ar] $3d^{10}$ $4s^1$, and crystallizes in a face-centered cubic (fcc) structure with an atomic spacing (Cu-Cu distance) of 2.56 Å. Fig. 1.1 represents the unit cell for the fcc structure and 3 different low index surfaces, *i.e.* (100), (111), and (110). The (111) and (110) were investigated in the present work. As appreciated from the Fig. 1.1, there are several differences among these surfaces.

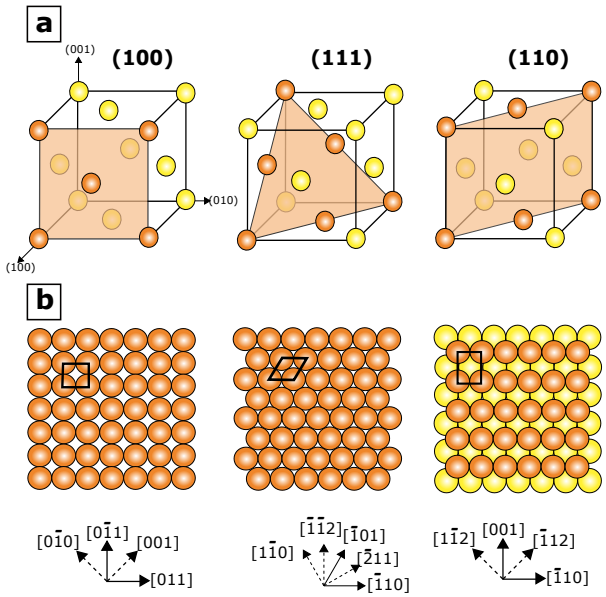

Figure 1.1: (a) fcc unit cell and the orientations of (100), (111), and (110) surfaces, (b) and their corresponding close-packed model together with the main crystallographic axis of the same surfaces.

For instance, the number of nearest neighbors for a surface atom on a terrace of (100), (111) and (110) are 8, 9 and 7, respectively There is another difference for (110) surface, which is the coordination number 11 for the atoms in the second layer. Hence, it can be considered the atoms in the 2nd layer regarded as surface atoms. Because the coordination number for a bulk fcc structure is 12, the broken bonds for the surface atoms are 4, 3, 5, respectively. In Table 1.1 a list of some of the general properties of the above mentioned fcc surfaces for copper is shown. It can be easily seen that both the number of broken bonds and density of atoms in the surface unit cell are closely related to the surface free energy. Thus, the more open (dense) the surface is, the greater (smaller) the surface energy per unit area. The reactivity of the surface can be related to the surface free energy because it is a measure of excess free energy on the surface. The last row shows that the Cu(110) surface is the more open structure compared to the other two. As it is discussed in the next sections, the morphology of the Cu(110) in 10 mM HCl apparently differ from Cu(100) and Cu(111).

Table 1.1: Low Index Copper Surfaces[15]

.

Property	**Cu (100)**	**Cu (111)**	**Cu (110)**
Symmetry	4-fold	6-fold	2-fold
Coordination Number	8	9	7
Broken Bonds	4	3	5
Density (atoms/ Å^2)	$1/a^2 = 0.153$	$2/\sqrt{3}a^2 = 0.176$	$1/\sqrt{2}a^2 = 0.108$
Number of Possible Adsorption Sites	3	3	4
Work Function (eV)	4.59	4.94	4.48
Surface Free Energy (J/m^2)	2.09	1.96	2.31

Fig. 1.2 shows the 3D-reciprocal space (Brilloun zone) of the bulk cooper, showing the different symmetry points for where optical transitions are expected [16].

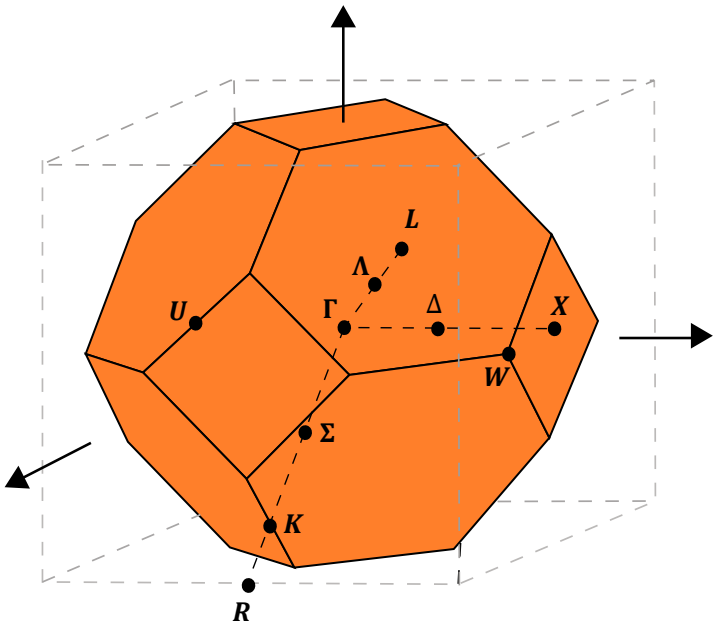

Figure 1.2: First Brillouin Zone of bulk copper.

Fig. 1.3 shows the real and reciprocal spaces of the Cu(110) surface. X and Y, are the main axes accounting for optical structure of Cu(110) surface and that is highly reactive as shown in several publications [17].

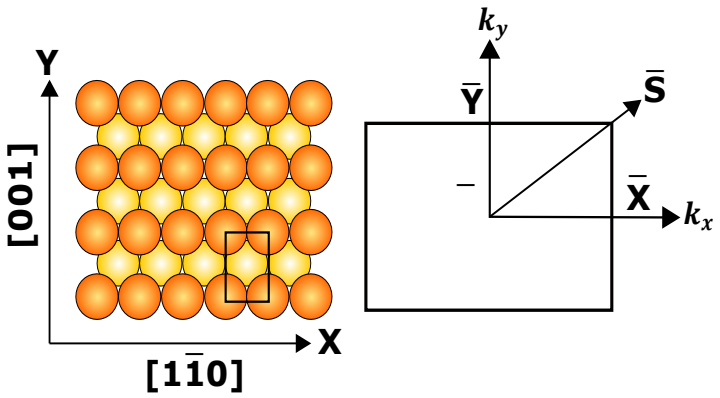

Figure 1.3: Real and Reciprocal Space of Cu (110) surface.

A band structure diagram is a 2D plot representing the allowed electronic energy levels of a solid material and is used to better understand its electrical and optical properties. Fig.1.4 shows the energy bands of the bare Cu(110) surface between the $\overline{\Gamma}$ and $\overline{Y}$ points for 23 and 24 layers.

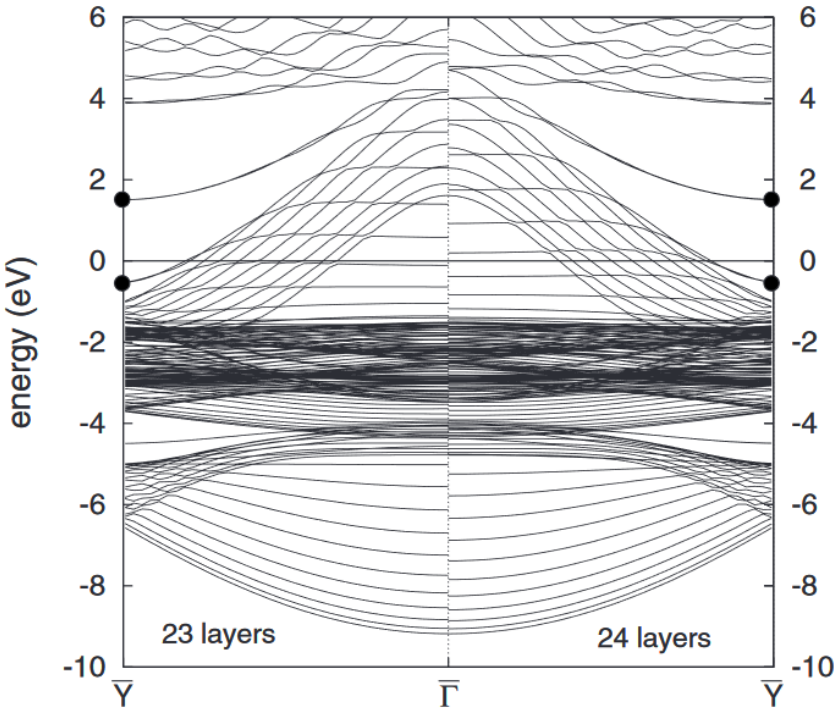

Figure 1.4: Energy bands of the bare Cu(110) surface between the $\overline{\Gamma}$ and $\overline{Y}$ point for 23 and 24 layers. The energies are given with respect to the Fermi energy. Surface bands are indicated by filled circles at the $\overline{Y}$ point [18].

In summary, the following situations are addressed in this thesis:

1. To present a systematic study comprising *in-situ* RAS-transient to assess the surface thermodynamics of the chloride adsorption on Cu(110) upon systematic variations of the applied electrode potentials in comparison to cyclic voltammetry (CV). Numerical time-derivatives of the measured RAS-transients are shown to be exclusively associated with electrical currents of those electrochemical reactions, which change the properties of the electrode surface. The recorded transient line-shapes track the Frumkin type isotherm properties related to chloride coverage. Both connections are theoretically discussed. Owing to the surface and interface specificity, RAS is shown to exhibit a high surface sensitivity. In particular, processes taking place in parallel, namely, the hydrogen evolution reaction (HER) as well as the copper dissolution as Cu^{+} and Cu^{2+}, do not contribute to the RAS response.

2. To tailor the surface states (SSs) by carefully changing the interface formed by the metal and the electrolyte, mediated by ionic species created at the forming complex interface. On a systematic study, by means of electrochemical impedance spectroscopy (EIS) jointly with *in-situ* RAS, to assess the evolution of SSs occurring at the solid-liquid-interface comprised between Cu(110) and HCl. By comparing the modeled RAS response with *in-situ* electrochemical scanning tunneling microscopy (EC-STM) measurements,to identify specific surface structures and correlate them to characteristic signatures of SR. This work renders both *in-situ* RAS and EIS as useful tools that help develop a systematic way to study and tune SR mediated by external potentials, inducing thermodynamically stable surface structures.

3. By means of both SE and chronoamperometry (CA), a comparative study of reaction kinetics of Cl adsorption between Cu(111) and (110) is carried out. Cl^{-} adsorption on Cu (111), shows a highly temporal charge transfer reaction, whereas that on Cu(110) shows a fast behavior which is attributed to a Cl-induced order - disorder transition.

The rest of the thesis is organized as follows. In chapter 2 the electrochemistry of metal-electrolyte interfaces is described. Chapter 3 details the experimental techniques used in this work, whereas in chapter 4 the experimental set-ups as well as the sample preparation are described. Chapter 5 describes the behavior of Cu (111) and (110) under HCl solution. Chapter 6 deals with the results and discussion, and finally, the main conclusions and perspectives of this work are outlined.

2 Electrochemistry of Metal-Electrolyte Interfaces

2.1 Electrochemical process at solid/liquid interfaces

Electrochemistry is the study of chemical reactions which involve production or consumption of electricity [19]. This makes it an interdisciplinary subject as it requires a good understanding of both chemistry and physics. The simplest electrochemical system consist of an electrode immersed in the solution of electrolyte. Electrodes can be made of metal or semiconductor. Electrolyte solution can be conformed by an ionic substance dissolved in a suitable solvent, like sodium sulfate ($NaSO_4$) dissolved in water. If two connected electrodes of copper and zinc are immersed in this electrolyte a current will flow coupled with the corresponding chemical reactions. On the zinc electrode the reaction taking place is:

$$Zn(s) \rightarrow Zn^{2+}(aq) + 2e^{-},$$

and on the copper electrode the chemical reaction is:

$$Cu^{2+}(aq) + 2e^{-} \rightarrow Cu(s).$$

Chemical reactions involving charges, as those written above, are called redox reactions. The value of current flowing through the system is determined by the kinetics of the redox reactions involved. In the above case, the current will flow until either zinc electrode or Cu^{2+} ions are not fully consumed. This happens because the system with a net flowing current cannot be in thermodynamic equilibrium. In the next sections the redox reactions, their thermodynamic equilibrium and their kinetics are discussed.

Figure 2.1 shows a schematic structure of a metallic surface in contact with an electrolyte solution. Atoms of the metal are shown with yellow spheres arranged in a crystal lattices, and solvent species (H_2O) are represented as tree blue spheres. Electrolyte solution is composed of solvent molecules, solvated positive ions (cations) and negative ions (anions). Cations are shown with a sphere and a '+' at the center, while anions with a '-' at the center. When a metal is brought in contact with an electrolyte different processes are likely to happen, specially under electrical potential control. These processes are described in the following subsections.

2.1.1 Adsorption/Desorption

The surface process corresponding to particle attachment is called adsorption. As shown in Figure 2.1, it is possible for some of the solvated anions in the solution to strip their water sheaths and directly

adsorb on the metal surface. This kind of process is called specific adsorption and happens when there is a chemical bonding of the ions to the metal surface atoms. Because of their bigger sizes and thus smaller charge densities, anions are usually less strongly solvated than cations; therefore their hydration sheaths are easier to break up and they are more often specifically adsorbed, particularly on positively charged metal surfaces. Adsorption generally depends on the potential, temperature, bulk concentration of adsorbed species in solution, pH and on the nature of the interactions between adsorbates and surface.

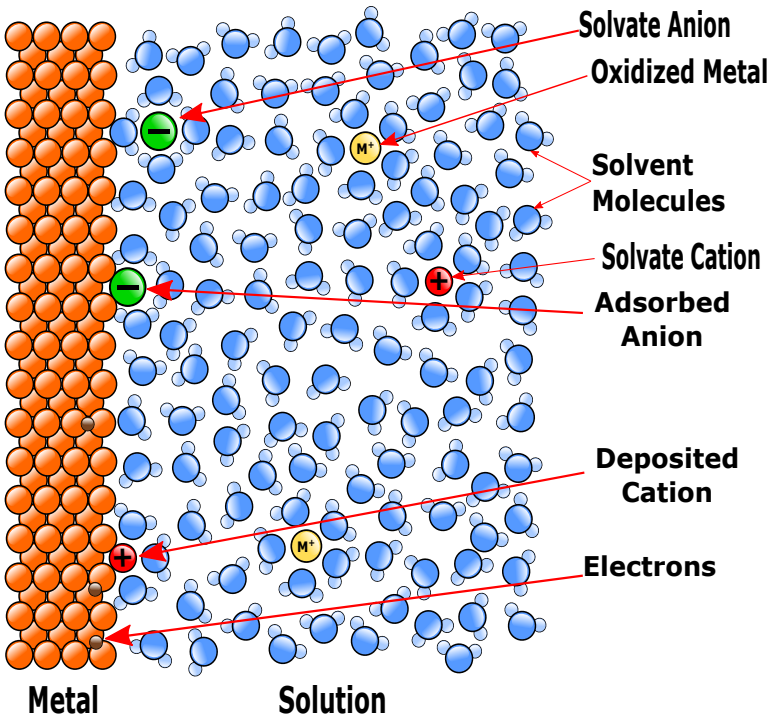

Figure 2.1: Simple Illustration of a metal-electrolyte interfaces without considering the formation of the Helmholtz layer.

The reverse process of adsorption is called desorption. For instance, at very negative potentials adsorbed anions may desorb from the surface as we will see in the following chapter.

2.1.2 Adsorption Isotherm

We consider the adsorption of a species I with concentration c_I in the bulk of the solution. The variation of the coverage θ with c_I, keeping all other variables fixed, is known as the *adsorption isotherm*.

In the simplest model, the adsorption which take place at fixed sites and the interaction between adsorbed particles is neglected. If we consider a surface that contain N adsorption sites, of which M are occupied, and let ϵ_{ad} be the adsorption energy per particle, the internal energy of the adsorbate is simply $M\epsilon_{ad}$. To obtain the free energy, we consider the entropy which according to the Boltzmann formula is: $S = klnW$, where W is the number of realizations of the system, therefore the free energy is given by:

$$F = M\epsilon_{ad} - kT \ln \frac{N!}{M!(N-M)!}. \tag{2.1}$$

We can rewrite the above Eq. 2 using Stirling's formula : $\ln n! \approx n \ln n - n$ for large n [20], gives:

$$F = M\epsilon_{ad} + \left[M \ln \frac{M}{N} + (N - M) \ln \frac{N - M}{N} \right]. \tag{2.2}$$

In equilibrium conditions, the chemical potential of the adsorbate must be equal to the chemical potential of the same particle in the solution. For the adsorbate we obtain:

$$\mu_{ad} = \frac{\partial F}{\partial M} = \epsilon_{ad} + kTln\frac{\theta}{1-\theta}, \tag{2.3}$$

where $\theta = M/N$ is the coverage. The chemical potential for an ideal solute has the form:

$$\mu_{sol} = \mu_0 + kTln\frac{c}{c_0}, \tag{2.4}$$

where c is the partial concentration, and the unit concentration c_0 makes the argument of the logarithm dimensionless.

In the following part the most common adsorption isotherms will be described.

- **Langmuir Isotherm**

  The *Langmuir isotherm* as depicted in Figure 2.2, takes into account the following considerations: (a) no interactions take place between the absorbed species on the electrode surface, (b) there is no heterogeneity of the surface, and (c) at high bulk activities, a saturation coverage of the electrode by adsorbate occurs.

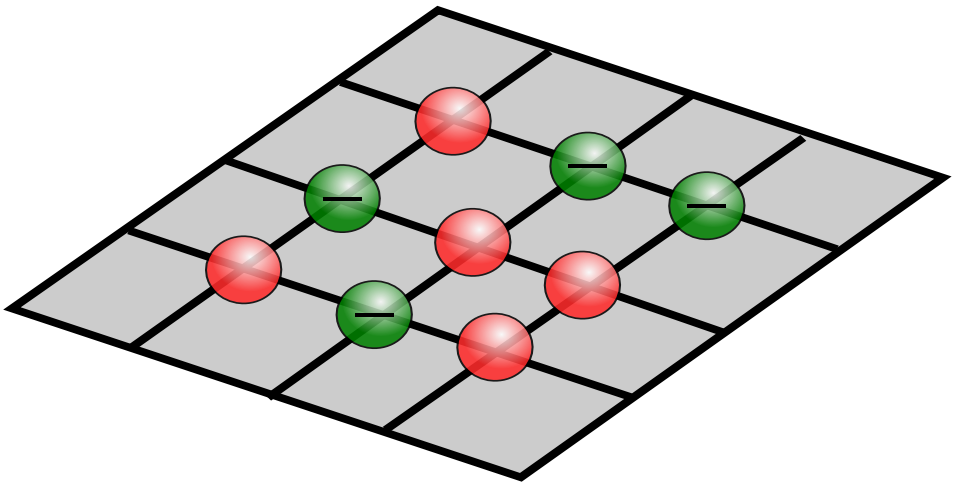

Figure 2.2: Illustration of a Lagmuir Isotherm. Red spheres describe empty sites, whereas green spheres assume that a site is already occupied; interaction between ions is neglected.

To interpret Fig. 2.2 we need to use the following equation:

$$0 = \Delta G_0 + eU + \frac{kT}{n} ln\left(\frac{\theta}{1-\theta}\right). \tag{2.5}$$

The first term ΔG_0 in Equation 2.5, contains the formation energy of the adsorption of an isolated ion, the second term is the applied potential U and e is the electron charge and the third term includes the surface coverage θ [20].

- **Frumkin Isotherm**

  A *Frumkin isotherm* deals with lateral interactions among adsorbed species. In Fig. 2.3 a reference ion green sphere with a corresponding image ion is placed and also a lateral interaction is taken into account between ions and neighboring images.

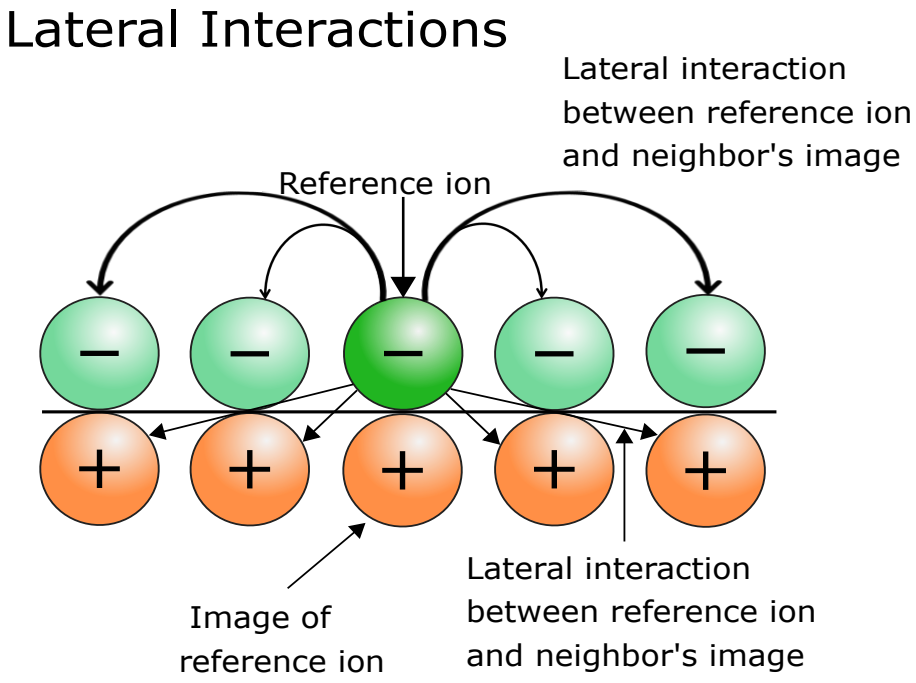

Figure 2.3: Illustration of Frumkin isotherm where lateral interactions are taken in the account.

We can account for such interactions by assuming that $\Delta\mu_{ad}$ is proportional to $\theta : \mu_{ad} = \mu^0_{ad} + \omega\theta$, where the constant ω is positive if the adsorbed particles repel, and negative if they attract each other[20]. The resulting isotherm:

$$0 = \Delta G_0 + eU + \frac{kT}{n} ln\left(\frac{\theta}{1-\theta}\right) + \omega\theta. \tag{2.6}$$

When the parameter ω is equal to zero (no interactions), the Frumkin isotherm reduces to the Langmuir isotherm.

- **Flory-Hiugyns Isotherm**

The Flory-Huggins isotherm is an extension of the Frumkin isotherm, where the process of adsorption is considered as a substitutional process (Figure 2.4). The molecule in solution that is going to be adsorbed promotes unoccupied sites on the surface of the electrode by displacing some of the water molecules that cover it [21]. This isotherm also takes into account the size of the molecules.

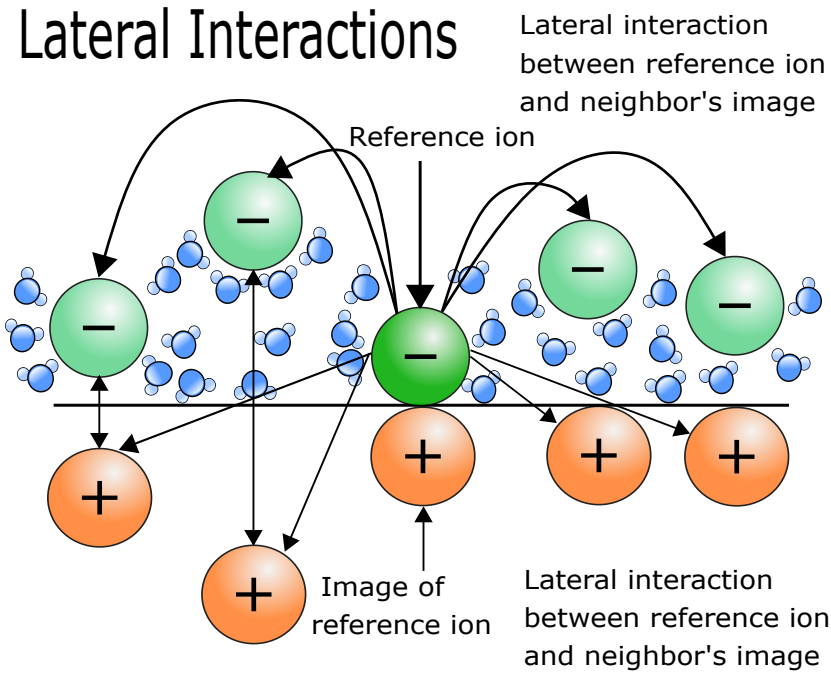

Figure 2.4: Illustration of the Flory-Hiugyns Isotherm.

We can interpret the Figure 2.4 using the following equation.

$$0 = \Delta G_0 + eU + \frac{kT}{n} \ln\left(\frac{\theta}{(1-\theta)^m}\right) + \omega\theta. \tag{2.7}$$

The main characteristic of this isotherm (Eq. 2.7) is the inclusion of the term $\frac{\theta}{(1-\theta)^m}$, where the value m is regarded as the number of water molecules which have to be desorbed from the surface upon the adsorption of one ion.

2.1.3 Electrochemical reactions

Reactions involving charge transfer mechanism through the interface and hence, a flow of a current, are called electrochemical reactions. In general two types of such reactions exist:

- **Charge-transfer reaction**

  The charge-transfer reaction is a reaction with electron transfer. It is indicated at the center of Figure 2.1 on the metal surface. One anion partially leaves its water sheath and transfers one electron into the metal surface and adsorbs on it. A well known example of charge transfer reaction is the reduction of Fe(III) to Fe(II):

$$Fe_{aq}^{3+} + e^{-}(metal) \rightarrow Fe_{aq}^{2+}.$$

For such a reaction to occur electrons tunnel over a distance of 10 Å or more, and the reacting species need not to be in contact with the metal surface [20].

- **Ion-transfer reaction**

The lower part in Figure 2.1 shows a metal atom "M" already adsorbed at the surface, which gives an example of an ion-transfer reaction. It involves the transfer of a metal ion from the solution onto the metal surface, where it is discharged by taking up electrons from the metal. Such a process can be intentionally considered for a large amount of metal ions for the purpose of metal deposition.

2.1.4 Anodic dissolution of metals

Anodic dissolution of a metals is indicated in the lower part of Figure 2.1, where one atom is dissolved as "M^+" into the solution and leaves one electron in the metal electrode. This process can be written as

$$M \rightleftharpoons M_{aq}^{n+} + ne^-.$$

The difference between the spontaneous oxidation and anodic dissolution of metals is that the latter occurs actively at the very positive (anodic) potentials, while the former one is spontaneous and occurs in small amounts depending on the electrolyte and the type of metal.

2.1.5 Under-potential deposition of metals

Under-potential deposition (UPD) in metals is the process of electrodeposition (reduction) of metal cations to another solid metal at a potential less negative than the equilibrium potential for the reduction of the metal. UPD occurs most of the time up to one monolayer, and is theoretically possible when the interaction between the metal ions and substrate is stronger than the metal-metal interactions.

2.2 Structure of electrified metal-electrolyte interfaces

In the study of metal-electrolyte interfaces, one usually deals with charged electrode (metal) surfaces or electrodes at controlled potentials. In general, the interfaces on the metal side carry an excess charge that should be balanced with an equal amount of opposite charge on the electrolyte solution side. Therefore, the interface can be regarded as an electrical double layer with opposite charges. The earliest trial to model the electrical double layer of solid liquid interfaces was introduced by Helmholtz in 1879, where he considered it as a rigid arrangement of charges one-by-one on both sides such as a plane capacitor [22]. In reality, thermal distributions of charged particles in the solution should be considered in the model, as well as the ionic radii, specific adsorption, the dependence of the structure on the concentration of solution or potential, etc. In the following sections, we will present some more realistic models; in particular, the Gouy-Chapman (GC) and GC - Stern-Graham (GCSG) models.

2.2.1 The Gouy - Chapman model (GC)

Gouy and Chapman independently proposed the diffuse double layer model [22]. In this model ions are considered to be point charges in a dielectric medium and the metal electrode is considered as a perfect conductor. The Boltzmann statistics is employed to describe the distribution of the ions in the interface for which the Poisson's equation for electrostatics potential φ is written as follows:

$$\frac{d^2\varphi}{dx^2} = -\frac{\rho(x)}{\varepsilon\varepsilon_0} = -\frac{ze[n_+(x) - n_-(x)]}{\varepsilon\varepsilon_0}, \tag{2.8}$$

where

$$n_+(x) = n_0 \exp\left(-\frac{ze\varphi(x)}{kT}\right), n_-(x) = n_0 \exp\left(\frac{ze\varphi(x)}{kT}\right), \tag{2.9}$$

denote the thermally distributed positive and negative ionic concentrations based on Boltzmann's formula, respectively. Here we consider the so called $z-z$ electrolyte solution; *i.e.* $A^{z+}B^{z-}$, which means equally charged anions and cations in the solution. Here, the planar metallic surface has been located at $x = 0$, and the solution extends over $[x = 0, \infty]$, z stands for number of charges, e is the electron charge; ε is the dielectric constant of the solvent, ε_0 is the permittivity of vacuum; k is the Boltzmann's constant, T is the absolute temperature in Kelvin, and n_0 describes the equilibrium concentration. By considering that $\varphi(+\infty) = 0$, the solution of equation 2.8 can be expressed as [20]:

$$\varphi(x) = \frac{4kT}{ze} tanh^{-1}\left(\frac{\sqrt{1+(\alpha\sigma)^2} - 1}{\alpha\sigma} exp(-\kappa x)\right), \tag{2.10}$$

where κ is the inverse Debye length denoted by:

$$\kappa = \sqrt{\frac{2(ze)^2 n_0}{kT\varepsilon\varepsilon_0}}, \tag{2.11}$$

σ is the surface charge density, which was first extracted by Grahame (or according to Gauss's theorem $\mathrm{E}(x = 0) = \sigma/(\varepsilon\varepsilon_0)$) as

$$\sigma = \sqrt{8kTn_0\varepsilon\varepsilon_0}\sinh\left(\frac{ze\varphi(0)}{2kT}\right), \tag{2.12}$$

and $\alpha = 1/\sqrt{8kTn_0\varepsilon\varepsilon_0}$. The consideration of the Poisson-Boltzmann equation (Eq. 2.8) is useful when $\frac{ze\varphi(x)}{kT} \ll 1$. In this limit instead of Equation 2.8, a linearized form is valid as follows:

$$\frac{d^2\varphi}{dx^2} = -\kappa^2\varphi(x), \tag{2.13}$$

with a solution

$$\varphi(x) = \frac{\sigma}{\varepsilon\varepsilon_0\kappa}\exp(-\kappa x), \tag{2.14}$$

$$\rho(x) = -\sigma\kappa\exp(-\kappa x), \tag{2.15}$$

which describes an exponential shielding of the applied potential of the metal ($\varphi(0) = \sigma/\varepsilon\varepsilon_0\kappa$) in the solution over a characteristic distance of $1/\kappa$, or equivalently a volume distribution of opposite charges over the Debye length $1/\kappa$ in the solution; thereby balancing the excess charge on the metal. The Debye length here defines the thickness of the electric double layer. If one calculates the linear (based on Equations 2.14, 2.15) and full (based on Equation 2.12) capacity per unit area of the double layer, with $C = \frac{\partial\sigma}{\partial\varphi}$ one finds:

$$C_{GC}(\varphi) = \varepsilon\varepsilon_0\kappa \cosh\left(\frac{ze(\varphi - \varphi_{PCZ})}{2kT}\right). \tag{2.16}$$

In Equation 2.16 the term (φ_{PZC}) is generally described as the potential where the net charge of total particle surface (*i.e.*, absorbent's surface) is equal to zero, at this potential the Equ.2.16 has a minimum. Usually the GC theory is valid only at low electrolyte concentrations (mM) non-adsorbing electrolytes. In fact, the experimental values conform to the following equation for the capacitance:

$$\frac{1}{C} = \frac{1}{C_H} + \frac{1}{C_{GC}}, \tag{2.17}$$

where C_{GC} is given by Equation 2.16, and C_H is considered as Helmholtz capacitance. Equation 2.17 gives an experimental tool for calculating C_H. The plot of the inverse measured capacitances at different concentrations *versus* the calculated inverse GC capacitance should yield a line with slope 1 and intercept at $1/C_H$ (regarded as Parsons and Zobel plot). Straight line with the unit slope support the GC theory for the diffuse double layer, and the corresponding intercept determines the Helmholtz layer capacitance ($1/C_H$). Slopes lower than 1 are usually attributed to the geometrical roughness factor. Deviations from the straight line are regarded as an indication for specific adsorption or non-complete dissociation of electrolyte [23, 20].

2.2.2 The Gouy-Chapman - Stern-Graham (GCSG) model

In 1924, Stern combined the idea of Helmholtz and GC model in a way that he supposed there would be a layer of adsorbed ions near the electrode surface. These ions fully or partially leave their hydration sheaths. This happens because of the strong electrostatic field at the surface which is able to polarize the ion-hydration complexes and force the ions to leave their hydration sheaths. He proposed that the ions have finite sizes so they can not increasingly accumulate at the surface. By these considerations, the electric double layer bears two parts: (1) an inner layer (Stern layer) and (2) a diffuse layer (GC layer). In a Stern layer adsorbed ions are fixed, while in diffuse layer they are mobile because of thermal vibrations.

Figure 2.5 specifies details of different layers on a positively charged metal surface. The inner Helmholtz layer extends from the electrode surface to the center of specifically adsorbed ions (inner Helmholtz plane). In this layer, the potential drops drastically. The outer Helmholtz layer extends from the inner Helmholtz plane to the center of second layer of hydrated ions (outer Helmholtz plane). In this Stern layer, the potential drops linearly but not as drastic as the Helmholtz layer. Both inner and outer Helmholtz layers are compact where ions are immobile. The last part is the diffuse double layer, where ions are allowed to move or even to rotate. The potential drops exponentially to a constant value within the electrolyte.

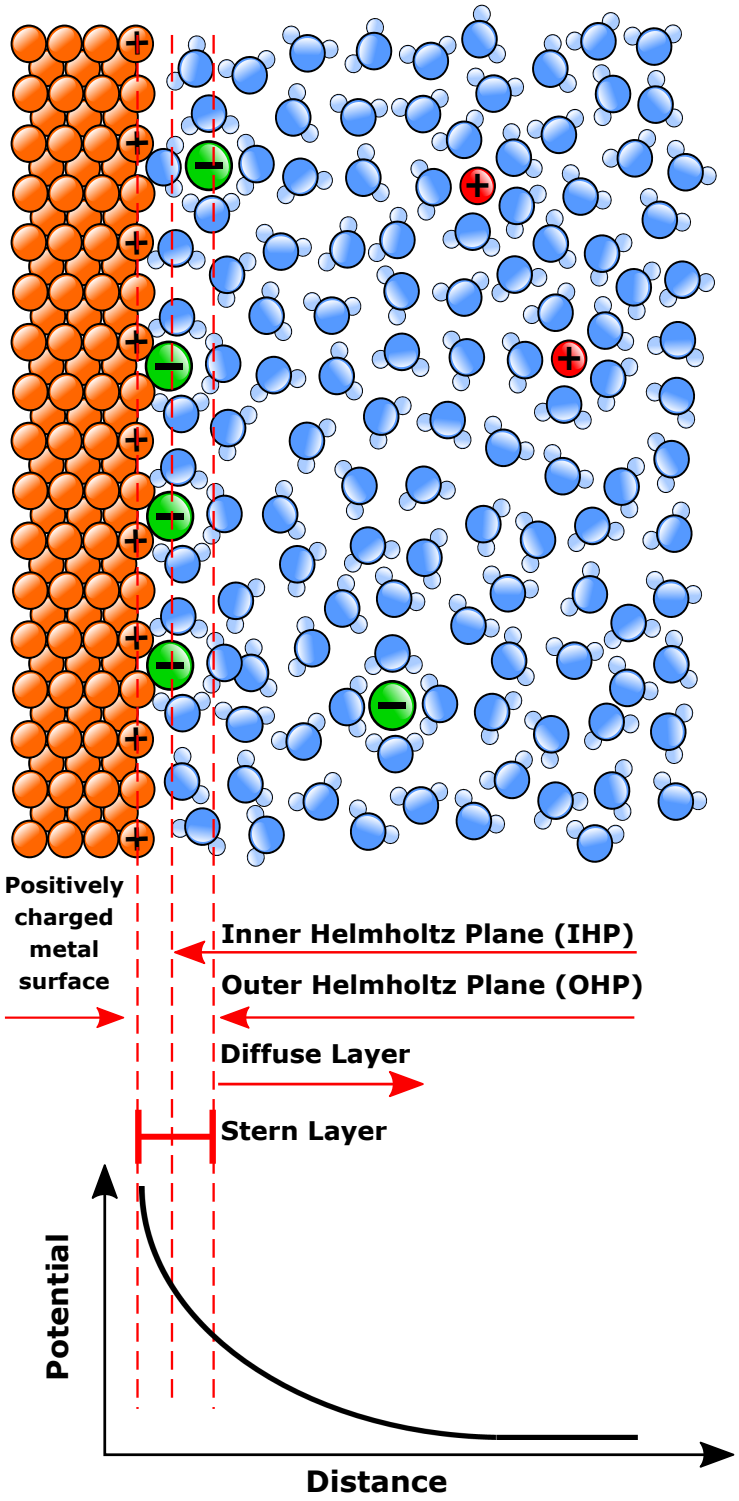

Figure 2.5: Schematics of a metal-electrolyte interface with different planes and layers. The potential drop versus distance plotted in different layers as indicated.

3 Experimental Techniques

3.1 Ciclyc-Voltammetry

Cyclic Voltammetry (CV) is an electrochemical probe that measures the current developing in an electrochemical cell under equilibrium conditions where the applied voltage is in excess of that predicted by the Nernst equation. CV is performed by cycling the potential of a working electrode and measuring the resulting current. The working principle is discussed as follows.

The potential of a working electrode is measured against a reference electrode which is maintained at a constant potential, and the resulting applied potential produces an excitation signal such as that represented in Fig. 3.1. In the forward path in Figure 3.1 the scanning starts first from a lower potential (a) and ends up at a higher potential (d). Such extreme (d) is called the switching potential and is the point where its value is sufficient high so as to cause an oxidation or reduction process of an analyte. The reverse process occurs from (d) to (g) and it is where the potential scans more negatively. Furthermore, Figure 3.1 shows a typical oxidation occurring from (a) to (d) and a reduction occurring from (d) to (g). It is important to note that some analytes undergoes throughout reduction first, for which the potential would first scan negatively. This cycle can be repeated and the scan rate can be varied. The slope of the excitation signal gives the scan rate used during the experiment.

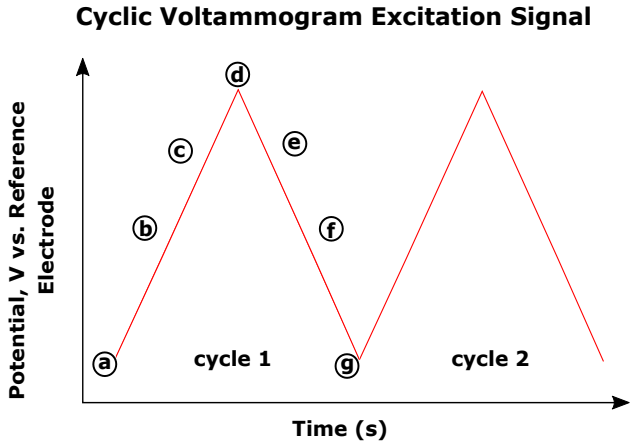

Figure 3.1: Cyclic volatmmetry Signal. From a to d is regarded as *anodic direction*, while from d to g is the *cathodic direction*.

A cyclic voltammogram is obtained by measuring the current developing at the working electrode during the potential scans. Figure 3.1 shows a cyclic voltammogram resulting from a single electron reduction and oxidation and considering the following reversible reaction:

$$M^+ + e^- \rightleftharpoons M.$$

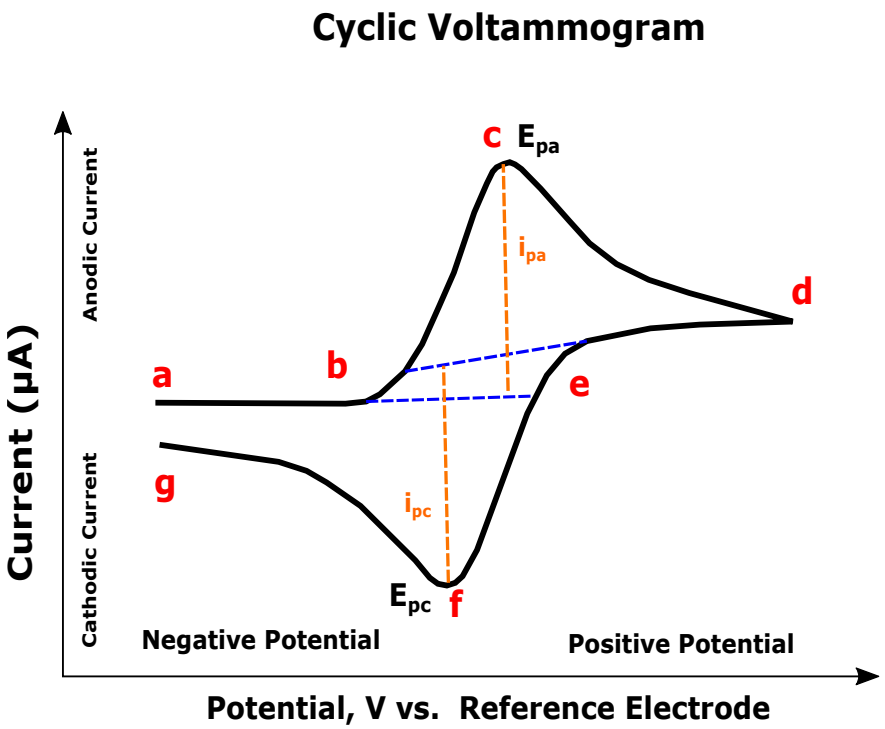

Figure 3.2: Voltammogram of a single electron oxidation-reduction.

In Figure 3.2, the oxidation process occurs from (a) the initial potential to (d) by switching the potential direction. In this region the potential is scanned in anodic direction so as to promoting an oxidation. The resulting current is called anodic current (i_{pa}). The corresponding peak potential occurs at (c) and is called the anodic peak potential (E_{pa}). The E_{pa} is reached when all of the substrate at the surface of the electrode has been oxidized. After the switching potential has been reached (d) the potential scanned in cathodic direction from (d) to (g), resulting in a cathodic current (i_{pc}) and a reduction occurs. The peak potential at (f) is called the cathodic peak potential (E_{pc}) and is reached when all of the oxidation at the surface of the electrode has been reduced.

3.2 Chrono-Amperometry

Figure 3.3 a) is a diagram of the waveform applied in a basic potential step in the experiment. Let us consider its effect on the interface between a solid electrode and an unstirred solution containing electro active species. As an example, take anthracene in deoxygenated dimethylformamide (DMF) as a typical example. It is commonly accepted that there exist a potential region where Faradaic processes do not occur; let V1 be in this region. On the other hand, we can also find a more negative potential at which the kinetics for reduction of anthracene becomes so rapid that no anthracene can coexist with the electrode, and its surface concentration goes nearly to zero. Consider V2 to be in this "mass-transfer-limited" region. Fig. 3.3 b) depicts the current response at V1 and V2 and the corresponding Equation 3.1, that describes the current response proportional to the square root of the time. Here it is more convenient the

use the Cottrell equation to describe the behavior of the current response after switching the potential from V1 to V2.

$$i \propto \frac{1}{\sqrt{t}} \tag{3.1}$$

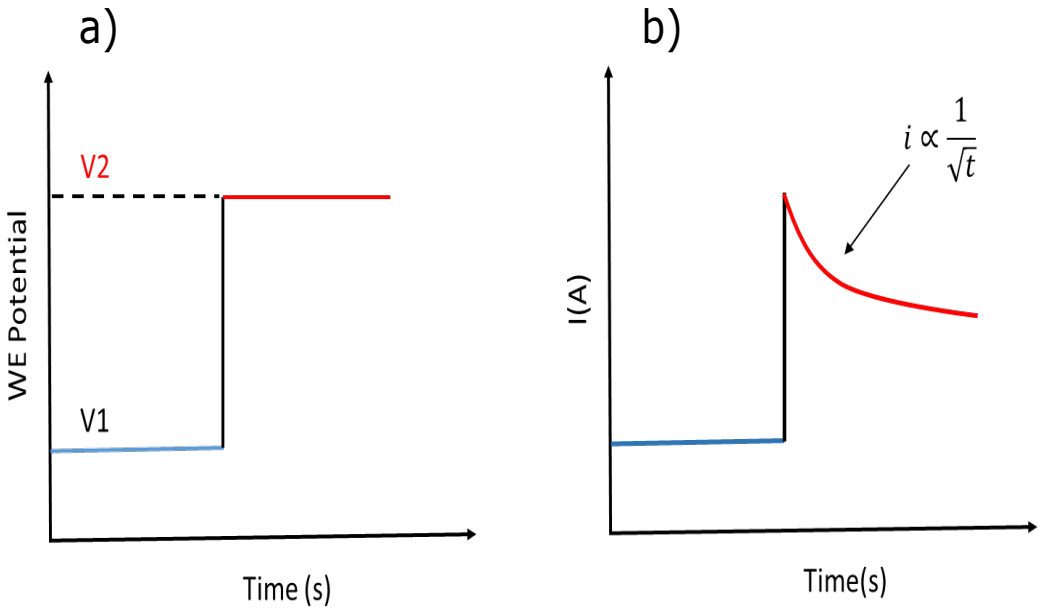

Figure 3.3: Illustration of a) voltage applied to cell begins at V1, where no reaction occurs and is stepped up to V2, causing electrode process to begin, and b) a current spike results.

As illustrated in Fig. 3.3 b) the current drops off with time according to the Cottrell equation 3.2, since material must diffuse to the electrode surface in order to react.

$$\mid i \mid = \frac{nFA[O]_{bulk}\sqrt{D}}{\sqrt{\pi}\sqrt{t}}, \tag{3.2}$$

where A is the area of the electrode, F is the Faraday constant, $[O]$ is the bulk concentration of an species O, D is the diffusion rate and it is the time.

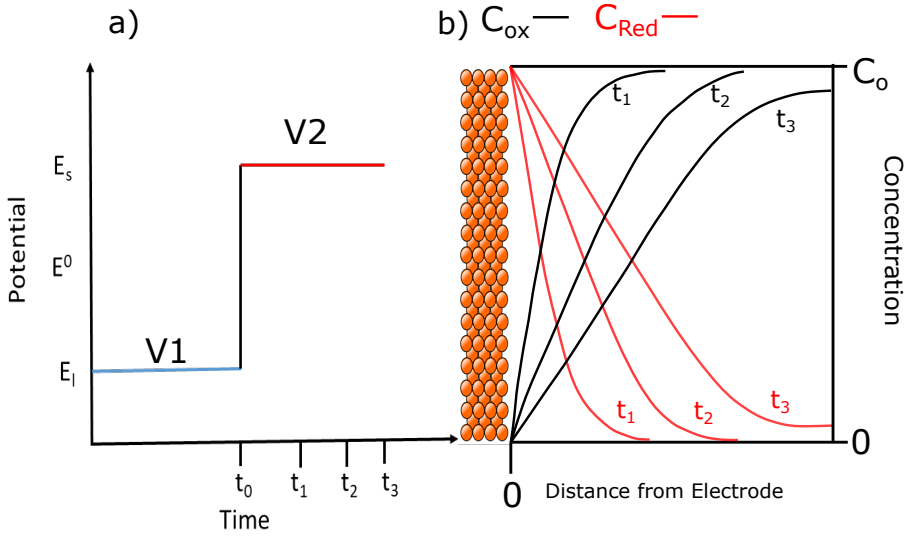

Figure 3.4: Illustration of a) Voltage applied to cell begins at V1 where no reaction occurs and is stepped up to V2 causing electrode process to begin, and b) a current spike results and a change in concentration near the surface an oxidation or reduction process.

The double potential step method provides a very comprehensive view of the rate constants of the chemical reaction, especially in the by product occurring in adsorption systems [24].

As an example of the use of CA, Pawar *et al*, have shown the capabilities of cooper oxide electrodes for supercapacitors and electrocatalyst in direct methanol fuel cell applications [25]. In their study they used CA to investigate the electrochemical energy conversion properties of the films via methanol electro-oxidation.

3.3 Electrochemical Impedance Spectroscopy

The electrochemical impedance spectroscopy (EIS) technique is a simple, fast, and non invasive measurement technique. Impedance refers to a physical variable that examines the characteristics of the resistance of an electrical circuit in presence of an alternating current (AC) applied between the electrodes. In this system, the current flow response is measured by applying a small sinusoidal potential and detecting changes in frequency (f) from the applied potential over a wide frequency range. Examination of the mathematical relations obtained by varying the excitation frequency, the impedance response appears as a complex number in function of the frequency. EIS is capable in assessing the intrinsic material properties and the particular processes involved in the conductivity/resistivity or the capacitance of the electrochemical system. These techniques serve as very useful tools for the characterization and analysis of wide gamut of materials.

The four quantities regarded as ohmic resistance, capacitance, constant phase element, and Warburg impedance (W) are used in the EIS analysis of electrolyte-based systems to investigate the impedance behavior of each particular system, and it is necessary to select an appropriate equivalent circuit (based on the elements defined in Table 3.1). Equivalent circuits are employed for approximating experimental impedance data as they provide good descriptions of impedance components in parallel and/or in series. Randles circuit is most commonly used for electrodes immersed in electrolytes; it includes solution resistance (R_s), charge (electron) transfer resistance(R_{ct}), capacitance of double layer (C_{dl}), and mass

transfer element, shown as Warburg impedance (W) [22].

Components	Equivalent Element	Current vs. Voltage	Impedance
Resistor	R[ohm]	$V = RI$	R
Capacitor	C[F, or $ohm^{-1} * s$]	$I = C\frac{dV}{dt}$	$\frac{1}{j\omega C}$
Inductor	L[H, or $ohm * s$]	$V = L\frac{di}{dt}$	$j\omega L$
Infinite Diffusion	Z_w[ohm]		$\frac{R_w}{\sqrt{j\omega}}$
Finite Diffusion	Z_o[ohm]		$\frac{R_D \tanh(\sqrt{(j\omega L_D^2)/D})}{\sqrt{(j\omega L_D^2)/D}}$ $\frac{R_D \coth(\sqrt{(j\omega L_D^2)/D})}{\sqrt{(j\omega L_D^2)/D}}$
Constant Phase Element	Q[$ohm^{-1}s^{\alpha}$]		$\frac{1}{Q(j\omega)^{\alpha}}$

Table 3.1: Impedance Components.

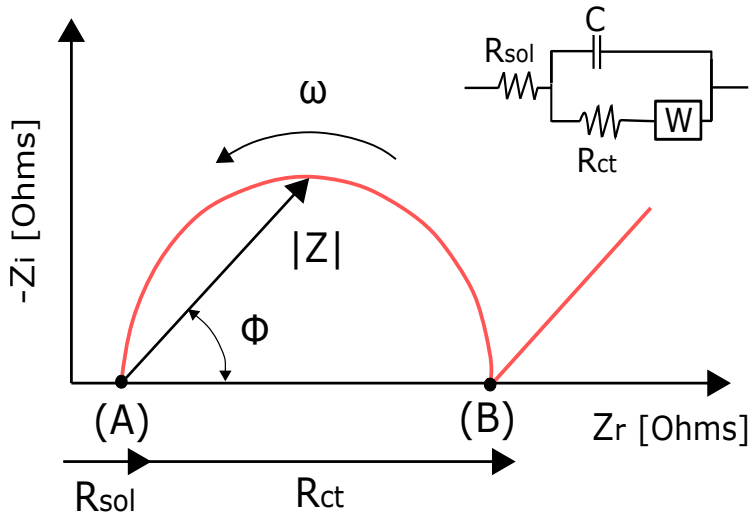

Figure 3.5: Typical Nyquist Plot of an electrochemical cell and the inset is the Randle's equivalent circuit.

As can be appreciated in Fig. 3.5, in a typical Nyquist plot the equation $\omega = 2\pi f = 1/R_{ct}$ is used to calculate the double-layer capacitance based on the frequency located on the maximum point of on the semicircle. A line at an angle of 45 degrees represents the Warburg limited behavior, which can be extrapolated from the real axis. Also, the interception at this section is equal to $R_s + R_{ct} - 2\sigma C_{dl}$, were σ represents the diffusion coefficient whose value can be subsequently calculated. In this method, R_s and R_{ct} can be readily obtained from the points (a) and (b), respectively. EIS widely used to investigate procedures for fabrication of several biosensors.

3.4 Reflection Anisotropy Spectroscopy

3.4.1 Operation principle and experimental set up

Reflection Anisotropy Spectroscopy (RAS) measures the difference of the complex reflection coefficients r_x and r_y for light being polarized along two orthogonal surface directions x and y, respectively. In contrast to spectroscopic ellipsometry, the incident and reflected light is always oriented along the surface normal. For an optical isotropic (cubic) crystal, the bulk contribution to Δr is zero. RAS signal thus arises from

the surface or interface. This makes RAS a highly surface sensitive optical technique. The complex reflection anisotropy is defined as the difference of the reflectance normalized to the mean reflectance:

$$\frac{\Delta r}{r} = 2\frac{r_x - r_y}{r_x + r_y}. \tag{3.3}$$

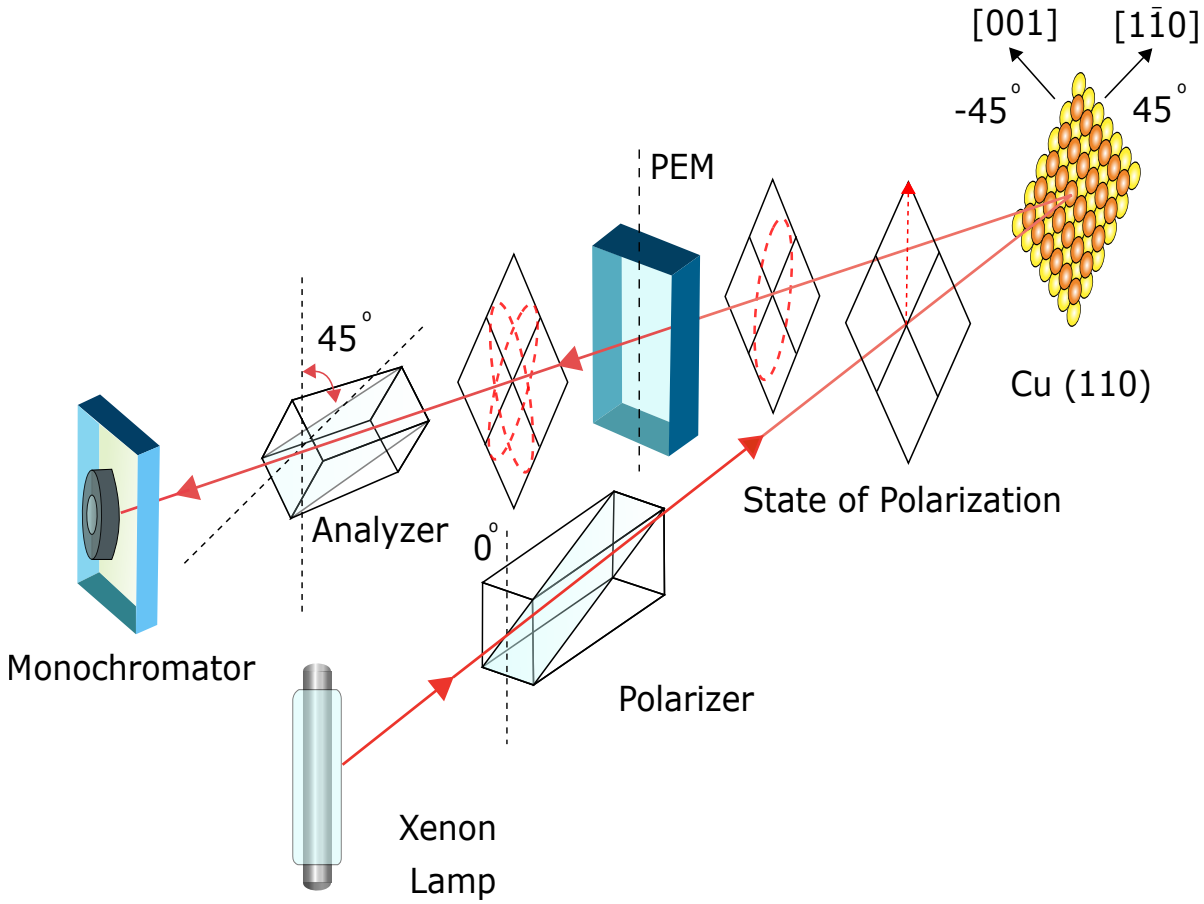

Figure 3.6: Typical set-up for reflectance anisotropy spectroscopy measurements [26].

In the next section, an equation that describes the signal related to the associated optical anisotropies of the sample under study is presented. Artifacts related to the optical viewports and mechanical miss alignment are neglected. The experimental RAS set up includes a photo-elastic modulator (PEM) operating at resonant frequency of 50 KHz. In brief, the heart of the PEM is a rectangular fused silica which is mechanically coupled to a piezoelectric transducer. A periodic mechanical strain renders the silica bar anisotropic, with two orthogonal refraction indexes. Therefore, a linear polarizer entering the PEM with an angle of 45° switches its polarization states along the two in-plane eigen-axes of the sample under study. Such modulation has a frequency of 100 KHz [27], see fig. 3.7.

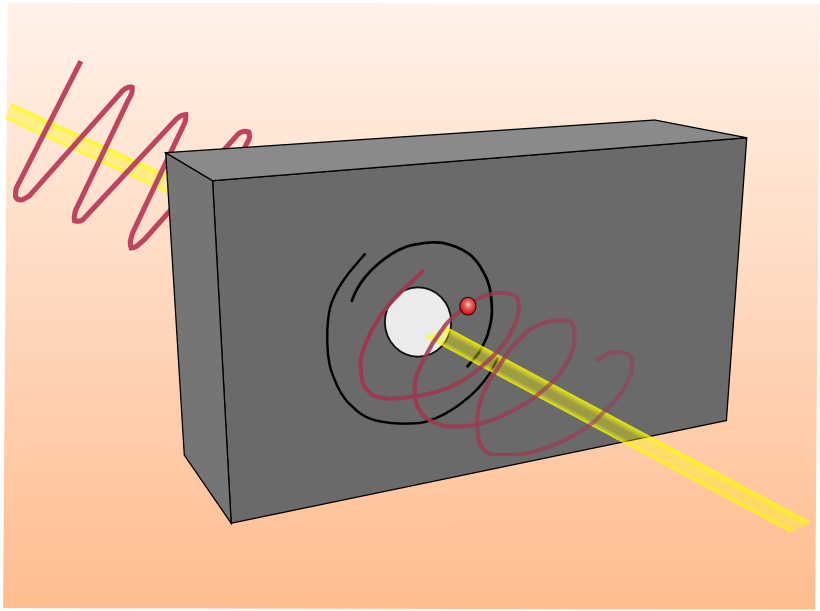

Figure 3.7: Schematic diagram of the photo elastic modulator. The input light is linearly polarized oriented 45 degrees with respect to the fast optical axis of the silica bar. The output polarization switches between two orthogonal polarizations with both circular and elliptical states in between.

The radiation source consists of a stable Xenon lamp which provides good intensity and is sufficient for our spectrometer to work in a range of 1.5 to 5.5 eV. The light before being focused onto the sample is polarized and after the reflection is modulated. The linear polarization is carried out using either a Woollanston or Rochon polarizer, oriented at an angle of 45 with respect to the plane of incidence.

The use of PEM offers high modulation speed, low noise and with an optimal polarizer and analyzer alignments, reduces the introduction of parasitic components that could affect the performance of the RAS system. The light reflected off the sample passes through a perpendicular analyzer with respect to the optical axis and with another arrangement of mirrors, the beam is again focused towards an optical fiber. After passing through the polarization optics, the intensity of the modulated transmitted light is processed using signal processing techniques. All the optical analysis of RAS is shown in the AppendixA.

3.4.2 The Three Phase Model

The difficulty to carry out a full first−principle calculation, rely on empirical approaches for the interpretation of the experimental RAS spectra. A simple way of interpreting the surface anisotropy is provided by the so-called three phase model[28], that divides the sample under study and its surrounding into 3 parts:

- The ambient atmosphere or liquid (liquid in our case).
- The surface (anisotropic) region.
- The underlaying bulk isotropic of the sample.

The model is illustrated in Fig. 3.8. Both the surface region (of thicknes d) and the semi-infinite bulk are modeled as continuous media with homogeneous dielectric functions, $\epsilon_s = \epsilon_{s1} + i\epsilon_{s2}$ and $\epsilon_b = \epsilon_{b1} + i\epsilon_{b2}$,

respectively. For vacuum, the dielectric function is unity: ($\epsilon_a = \epsilon_{a1} = 1$). Within this model, the relation between the measured RAS signal and the anisotropy of the surface dielectric function is given by

$$\frac{\Delta r}{r} = \frac{4\pi i d}{\lambda} \frac{\Delta \epsilon_s}{\epsilon_b - \epsilon_a} = \frac{4\pi i d}{\lambda} \frac{\Delta \epsilon_s}{\epsilon_b - 1}, \tag{3.4}$$

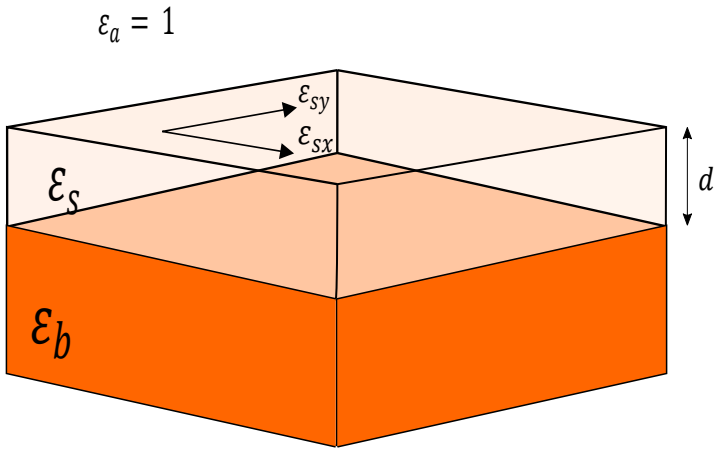

Figure 3.8: Illustration of the three phase model. $\epsilon_a$represents dielectric function of the ambient atmosphere or liquid, ϵ_s the dielectric function of the surface layer of thickness d which can be anisotropic. ϵ_b. Isotropic dielectric function of the bulk. $\epsilon_{sx}, \epsilon_{sy}$ are along the *in-plane* crystallographic axes.

where $\Delta\epsilon_s = \epsilon_{sx} - \epsilon_{sy}$ is the difference of the surface dielectric function along the two orthogonal symmetry directions x and y within the surface plane and λ is the wavelength of the light. The bulk dielectric function ϵ_b is assumed to be isotropic. In spite of this crude approach, such a model has been proven to be very useful for the interpretation of the experimental results [29, 30, 31]. The model is valid for small anisotropies and within the thin-film approximation $d \ll \lambda$, where λ is the photon wavelength [28].

3.5 Spectroscopic Ellipsometry

Spectroscopy Ellipsometry (SE) measures the change in polarization state that a linearly polarized light incident at an oblique angle experiences upon reflection (or transmission) by an optical medium of interest. The incident light is linearly polarized in such a way that it can probe, in principle, the three principal optical axes of the sample under study. The polarization state reflected off the medium is in general elliptical. For the analysis of the polarization states, the light is mathematically decomposed into projections along and perpendicular to the plane of incidence of the light, and such components are termed p- and s- polarizations, respectively. An ellipsometry experiment works then by measuring the relative changes of amplitude and phase of the p and s-polarizations (see Fig. 3.9). Its advantages over direct reflection and transmission experiments are double. First, as SE measures simultaneously two parameters (Ψ, Δ) obtained from $\rho = tan(\Psi)e^{i\Delta}$, it has access to both the real and imaginary parts of the optical properties of the medium in a single experiment without elaborate mathematical post-treatment of the results, and second, SE has no need of reference measurements that can easily be altered and thus, rendered useless (by lamp instabilities, for instance). The optical analysis of SE is shown in Appendix A.

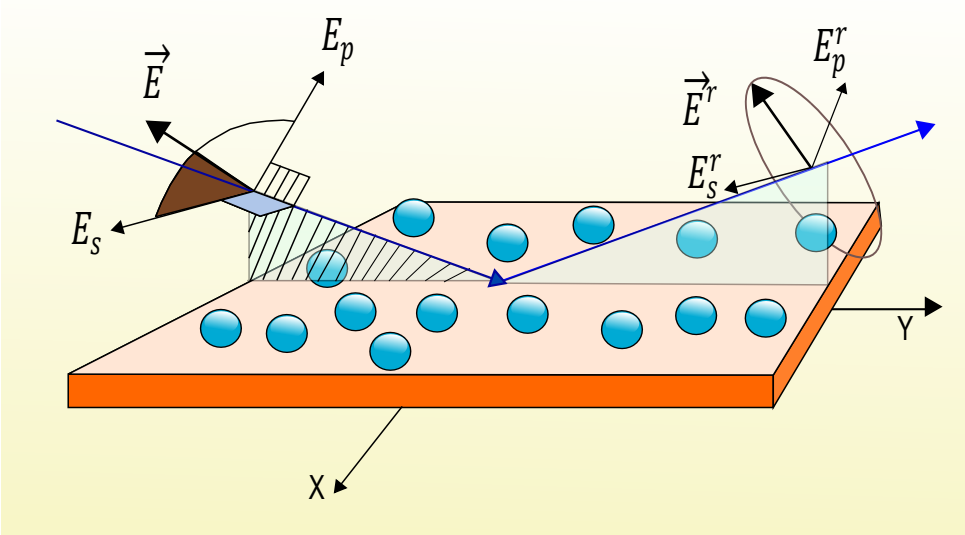

Figure 3.9: Typical schematic diagram employed for ellipsometry

3.5.1 Data Analysis

In order to retrieve the optical constants and thickness of samples from spectroscopic ellipsometry measurements, it is necessary to perform an analysis that consists of three major parts; i.e., dielectric function modeling, the construction of an optical model, and fitting to measured (Ψ, Δ) spectra. In the next section some dielectric function models of individual layers are reviewed. This section also addresses the effective medium approximation (EMA), which is commonly employed for surface roughness analysis. Here, we first discuss variations of (Ψ, Δ) in transparent and absorbing films and the fitting procedure for ellipsometry data analysis.

Angles Ψ and Δ represent the amplitude ratio and phase difference between p- and s-polarizations, respectively. However, Ψ and Δ generally show complicated variations with changes in optical constants and film thicknesses. In this section, variations of (Ψ, Δ) in transparent and absorbing films are described in some detail. The understanding of these behaviors is helpful, not only for the interpretation of measured spectra but also for the construction of optical models. Some of the most common models to interpret (Ψ, Δ) are listed next:

- Variations of (Ψ, Δ) with optical constants.
- Variations of (Ψ, Δ) in transparent films.
- Variations of (Ψ, Δ) in absorbing films.

In the experiments there is always a part that is needed to be considered in ellipsometry which is related to the presence of a small roughness, which is either an intrinsic part of the samples or extrinsic as in the case of external deposit by, *e.g.,* chemical vapor deposition , atomic layer deposition, etc, or as in our case, induced by adsorbing Cl^- ions on the surface. One of the most common model that describes it, is the so-called Effective Medium Approximation (EMA).

3.5.2 Effective Medium Approximation

Spectroscopic ellipsometry is quite sensitive to surface and interface structures. Thus, it is necessary to incorporate these structures into an optical model of data analysis. If we apply the effective medium approximation (EMA), the complex refractive index of surface roughness and interface layers can be calculated relatively easily. Furthermore, from ellipsometry analysis using EMA, we can characterize volume fractions in composite materials. This section will review various effective medium theories and explain modeling of surface roughness layers. It is anticipated that most of the content described it in this section is adopted from ref [32].

Effective Medium Theories

The dielectric constant represents the magnitude of dielectric polarization formed in a dielectric by an external ac electric field. Now consider a spherical dielectric inserted into a capacitor Fig. 3.10(a). If an external electric field is applied to this capacitor, polarization charges will be created on the outer surface of the dielectric by dielectric polarization. Consequently, the atoms inside the dielectric will react to an electric field induced by the polarization charges (E') in addition to the external electric field (E). In other words, by dielectric polarization, the electric field inside the dielectric (cavity) becomes stronger than the electric field applied to the capacitor. In particular, the electric field generated by the polarization charges is referred to as the Lorentz cavity field [33]. If we use the notation of Fig. 3.10(b), the Lorentz cavity field(E') is given by the following Equation [33]:

$$E' = \int_0^{\pi} (L^{-2})(2\pi L sin\theta)(Pcos\theta)(cos\theta)(Ld\theta) = \frac{4\pi P}{3}. \tag{3.5}$$

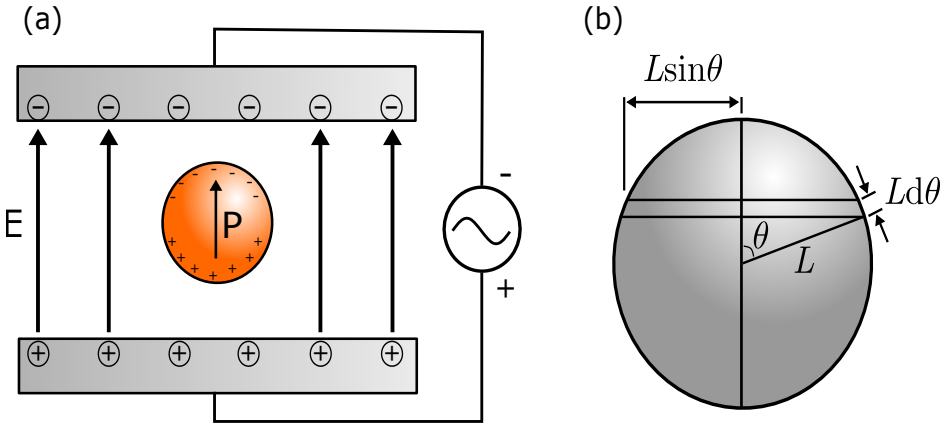

Figure 3.10: (a) Spherical dielectric inserted into a capacitor, and (b) calculation model of the polarization charges generated on the outer surface of a spherical dielectric. (b) L and θ represent the radius and the angle from the center of the sphere, respectively adapter from [32].

Here, P is the dielectric polarization. In the above equation, $Pcos\theta$ represents the polarization charge density on the surface of the circle shown in Fig. 3.10(b), and $Ecos\theta$ describes the electric field formed in the center of the sphere. Eq. 3.5 assumes that E' is independent of the size of L. The result shown in Eq. 3.5 indicates the one in CGS units and, in SI units, we obtain $E' = P/(3\epsilon_0)$ from the conversion of $4\pi \longrightarrow 1/\epsilon_0$ [33]. Thus, the local field $E_{loc} = E + E'$ in SI units is expressed by

$$E_{loc} = E + \frac{P}{3\epsilon_0}. \tag{3.6}$$

From Eq. 3.6 it is clear that E_{loc} in cases with increasing dielectric polarization. Here, we assume an electric polarization and N_e as the number of electrons in the dielectric. In this case, the dielectric polarization is given by $P = N_e \alpha E_{loc}$, where α represents the polarizability, accounting for the proportion of the dielectric polarization. Substituting Eq. 3.6 into $P = N_e \alpha E_{loc}$ yields:

$$P = N_e \alpha E / \left(1 - \frac{N_e \alpha}{3\epsilon_0}\right). \tag{3.7}$$

If we substitute Eq. 3.7, we arrive to the well-know formula, known as the Clausius-Mossoti relation:

$$\frac{\epsilon - 1}{\epsilon + 2} = \frac{N_e \alpha}{3\epsilon_0}. \tag{3.8}$$

When the above dielectrics is composed of two phases (components) a and b. we obtain

$$\frac{\epsilon - 1}{\epsilon + 2} = \frac{1}{3\epsilon_0}(N_a \alpha_a + N_b \alpha_b). \tag{3.9}$$

The Lorentz-Lorenz (LL) relation is expressed from Eqs. 3.8 and 3.9 as [34]:

$$\frac{\epsilon - 1}{\epsilon + 2} = f_a \frac{\epsilon_a - 1}{\epsilon_a + 2} + (1 - f_a)\frac{\epsilon_b - 1}{\epsilon_+ 2}, \tag{3.10}$$

where ϵ_a and ϵ_b represents the dielectric constants of the phase a and b, respectively, and f_a and $(1 - f_a)$ show each volume fraction. In this effective medium theory, ambient surrounding the dielectric is vacuum or air, similar to Fig. 3.10(a). When this spherical dielectric is present in a host material with a dielectric constant ϵ_h, Eq. 3.10 is rewritten as

$$\frac{\epsilon - \epsilon_h}{\epsilon + 2\epsilon_h} = f_a \frac{\epsilon_a - \epsilon_h}{\epsilon_a + 2\epsilon_h} + (1 - f_a)\frac{\epsilon_b - \epsilon_h}{\epsilon_b + 2\epsilon_h}.. \tag{3.11}$$

In an effective medium theory, known as the Maxwell Garnett (MG) model, the dielectric constant of mixed phase materials is described by assuming $\epsilon_a = \epsilon_h$ in Eq. 3.11 [34]:

$$\frac{\epsilon - \epsilon_a}{\epsilon + 2\epsilon + a} = (1 - f_a)\frac{\epsilon_b - \epsilon_a}{\epsilon_b + 2\epsilon_a}. \tag{3.12}$$

As shown in Fig. 3.11(a) the MG model assumes a structure in which the phase of ϵ_b is surrounded by the phase of ϵ_a, and their volume ratio determines f_a [35]. In the case of the MG model, however, if we exchange ϵ_a with ϵ_b, the resulting ϵ varies. On the other hand, Bruggeman assumed $\epsilon = \epsilon_h$ in Eq. 3.11 and proposed the effective medium approximation (EMA) expressed by the following equation [34]:

$$f_a \frac{\epsilon - \epsilon}{\epsilon_a + 2\epsilon} + (1 - f_a)\frac{\epsilon_b - \epsilon}{\epsilon_b + 2\epsilon} = 0. \tag{3.13}$$

In the EMA shown in Fig. 3.11, f_a and $(1 - f_a)$ represents the probabilities of finding ϵ_a and ϵ_b in a spherical space [35]. This model can be extended easily to describe a material consisting of many phases:

$$\sum_{i=1}^{n} f_i \frac{\epsilon_i - \epsilon}{\epsilon_i + 2\epsilon} = 0. \tag{3.14}$$

There are other models in which two dielectrics are placed in parallel Fig. 3.11(c) and in series Fig. 3.11(d). The dielectric constant ϵ of Fig. 3.11(c) is given by

$$\epsilon = f_a \epsilon_a + f_b \epsilon_b. \tag{3.15}$$

The above equation is quite similar to the formula used for capacitance calculation. In the parallel configuration, there is no interaction between ϵ_a and ϵ_b, and the screening factor becomes q =0 ($0 \leq q \leq 1$). On the other hand, ϵ in Fig. 3.8(d) is calculated from

$$\epsilon^{-1} = f_a \epsilon_a^{-1} + f_b \epsilon_b^{-1}. \tag{3.16}$$

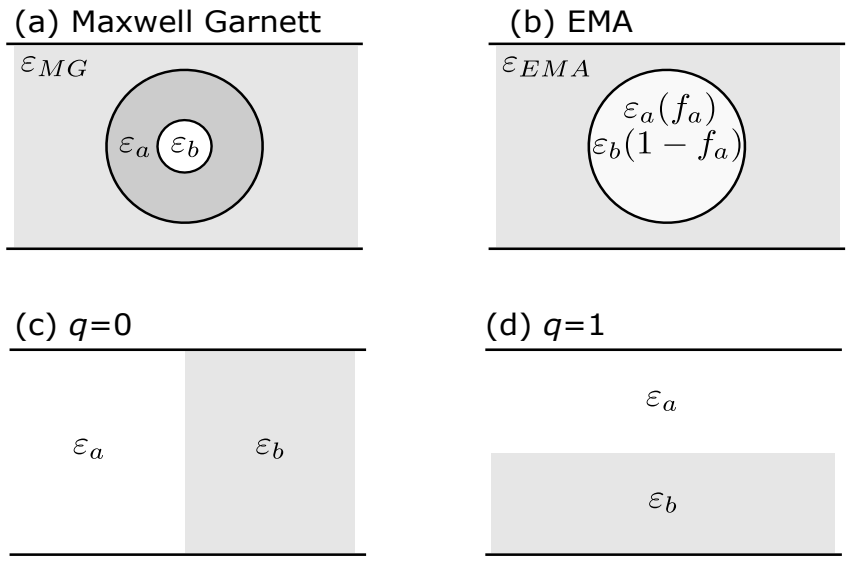

Figure 3.11: Physical models for effective medium theories: (a) Maxwell Garnett, (b) effective medium approximation (EMA), (c) $q = 0$, and (d) $q = 1$.

In this configuration, the screening effect is maximized (q=1). In case of a two-phase material, all effective medium models shown in 3.11 can be expresed by a single formula [34]:

$$\epsilon = \frac{\epsilon_a \epsilon_b + k\epsilon_h (f_a \epsilon_a + f_b \epsilon_b)}{k\epsilon_h + (f_a \epsilon_b + f_b \epsilon_a)}. \tag{3.17}$$

Here, k is defined as $k = (1 - q)/q$ using the screening factor q. In models assuming spherical dielectrics (*i.e.,* the MG and EMA models), the screening factor is given by $q = 1/3$. In Eq. 3.17, the MG and EMA models are described by setting $\epsilon_h = \epsilon_a$ and $\epsilon_h = \epsilon$, respectively. Eqs. 3.15 and 3.16 can also be expressed by inserting $q = 0$ and $q = 1$ into Eq. 3.17, respectively. Figure 3.12 shows the dielectric constant of two-phase composite (a and b), plotted as a function of the volume fraction of the component $b(f_b = 1 - f_a)$. In this example, the dielectric constants of the phases a and b were assumed to be $\epsilon_a = 2$

and $\epsilon_b = 4$, respectively, and ϵ for EMA, $q = 0$, and $q = 1$ were calculated. Naturally, when $f_b = 0$ and 1, we observe $\epsilon = \epsilon_a$ and $\epsilon = \epsilon_b$, respectively. In the case of $q = 0, \epsilon$ increases linearly with increasing f_b, since there is no interaction between the two components. In the model of $q = 1$, however, the values obtained at $0 < f_b < 1$ are always lower than those for $q = 0$ due to the screening effect. In other words, when there is a screening effect, ϵ is more influenced by the phase having a lower dielectric constant. As confirmed from Fig. 3.12, the values of EMA are intermediate between $q = 0$ and $q = 1$, but are closer to those of $q = 0$ since the screening factor of EMA is $q = 1/3$. Quite interestingly, even when $f_b < 0$ and $f_b > 1, \epsilon$ can be calculated from the above models and we sometimes obtain these volume fractions in actual data analyses. Although the volume fractions $f_b < 0$ and $f_b > 1$ are unphysical, their meanings are straightforward; *i.e.,* we obtain $f_b < 0$ when dielectric constants used in an analysis are too high and, conversely, we obtain $f_b > 0$ when dielectric constants are too low.

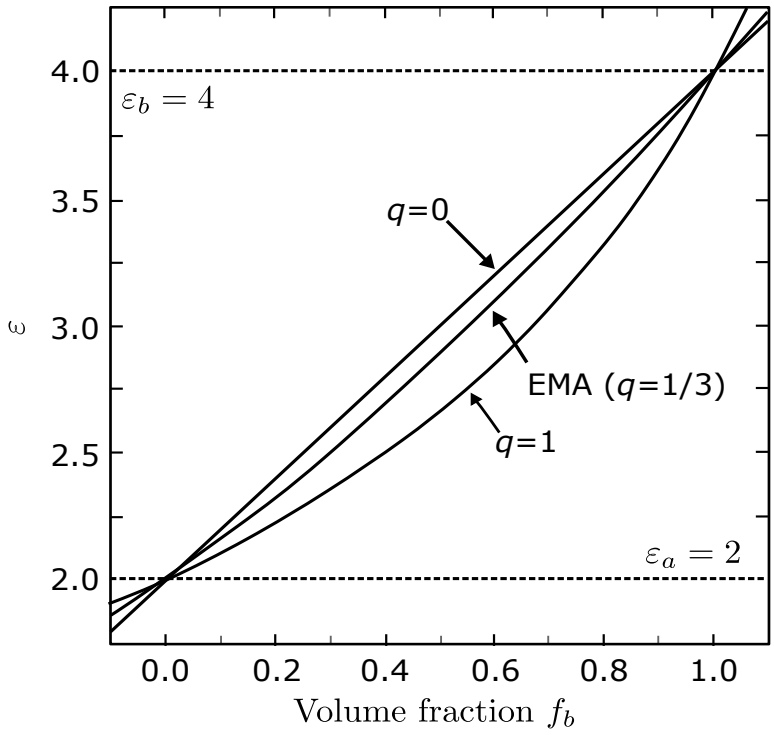

Figure 3.12: Dielectric constant ϵ of a two-phase composite (a and b) calculated from EMA for $q = 0$ and $q = 1$, plotted as a function of the volume fraction of the component b. In this calculation, the dielectric constants of the phases a and b were assumed to be $\epsilon_a = 2$ and $\epsilon_b = 4$ with their volume fractions of f_a and $f_b = 1 - f_a$, respectively adapted from [32].

When value ϵ in Fig. 3.12 is determined from an ellipsometry data analysis, f_b can be estimated by applying an effective medium model, if ϵ_a and ϵ_b are known. We can also employ f_b as an analytical parameter in data analysis. Among various effective medium theories, the effective medium approximation has been reported to provide the best fit to (Ψ, Δ) spectra, with respect to the analysis of surface roughness layers [36, 37]. Nevertheless, although physical values estimated from the analyses vary, similar results can also be obtained using other models [37]. Accordingly, ellipsometry results are basically independent of effective medium theories used in data analyses [37]. At present, the effective medium approximation has mainly been applied to ellipsometry analysis. In some materials, however, the best result has been obtained from the model of $q = 0$ [38]. Thus, an appropriate effective medium model may vary according to the optical properties of composite materials.

4 Experimental set-up

4.1 Sample Preparation

Sample preparation is one of the critical issues prior any electrochemical and optical experiment for *in - situ* measurements, specially with samples such as copper where a native oxide film is formed in ambient conditions. Such an oxide film, of a few nm thicknesses, is no conductive and should be removed with great care so as to avoid introducing new residual compounds, like organic residuals, and resulting in an acceptable flatness for the optical experiments see Fig. 4.4a. This copper samples, were cut for (110) termination from a 99.999% pure copper crystal, polished mechanically with different abrasives graded from μm down to nm scales so that the roughness scaled better than 30 nm as delivered from Mateck GmbH, Germany.

After several experiments, the sample gets rough and the following steps are need in order to recover a smooth, mirror like surface:

- **Mechanical Polishing**
  - Sample polishing with sand paper (grain size 2000)
  - Sample polishing with sand paper (grain size 4000)
- **Sample cleaning to remove organic residuals**
  - Aceton for 3 minutes in a sonication Bath
  - Isopropanol for 3 min in a sonication Bath
  - HCl 1M for 3 min in a sonication Bath
  - Ultra-Pure Water for 3 min in a sonification Bath
- **Electropolishing in Ortho-Phosphoric Acid 85%**
  - Perform a Linear sweep from -500 mV ut to 1.2 V
  - Determine the potential where the Cu dissolution is even on the surface
  - Carry out a chrono-amperometry transient for 1800 seconds until the sample looks mirror like).

In the next subsection the electro-polishing procedure will be describe owing to its importance to prepare the sample prior any experiment.

4.1.1 Electro-polishing

Prior each experiment the native oxide is removed by electrochemical polishing at +0.5 V (anodic potential) in ortho-phosphoric acid (H_3PO_4 85%) during 20 min after mechanical polishing; however, if the sample does not require mechanical polishing then the electro-polishing can be done from 5 to 10 min 4.4b. Fig. 4.1 shows the current-voltage plot as measured during the copper electro-etching process. The applied potential on copper sample was ramped from -0.5 up to 1.2 volts (vs. the Pt wire) set to 20 mV/s. The active dissolution of copper occurs after the maximum peak is reached around -0.1 volts as depicted in Fig. 4.1; after the maximum current peak the copper dissolution is removed evenly, thereafter a small flat region is reached where the copper oxidation starts at around +1 volt. At this potential the linear sweep needs to be stopped. To remove the copper from the surface in a evenly rate it is necessary to subtract -500 mV from the flat region (see Fig. 4.1). All the measured potentials are referenced to the Pt wire. Due to the formation of oxygen bubbles at the copper surface, the sample needs to be put in parallel position in front of the counter electrode (CE) (Pt plate) as can be appreciated in Fig. 4.3. Residues of the electro-polishing process are purged by deaerated ultra pure water in Ar ambient. Purging with the sample solution is possible too. However, in case of HCl, since it is corrosive it is not recommended. To avoid the oxygen effect on copper during the assembling of the cell and transfer to the chamber, a protective droplet of deaerated water is placed on top of the crystal. The sample preparation should be fast enough so as to avoid re-contamination of the sample before the assemble. Over long time use of copper a contamination is unavoidable mainly from the air, such as carbon or sulfur residuals. Thereafter, to remove carbon or sulfur contaminants one must consider annealing the sample in hydrogen atmosphere prior to any other cleaning step.

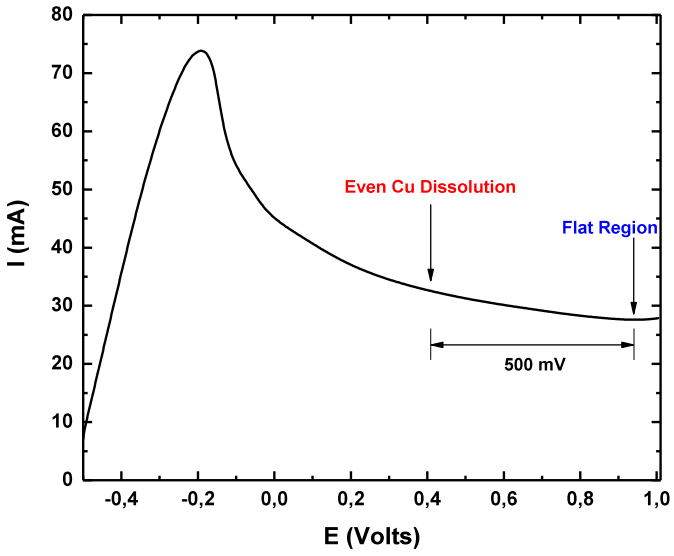

Figure 4.1: Typical voltammogram of a linear sweep of Cu samples in H_3PO_4 from - 500mV up to 1 V, in order to detect the potential where dissolution of Cu is homogeneous.

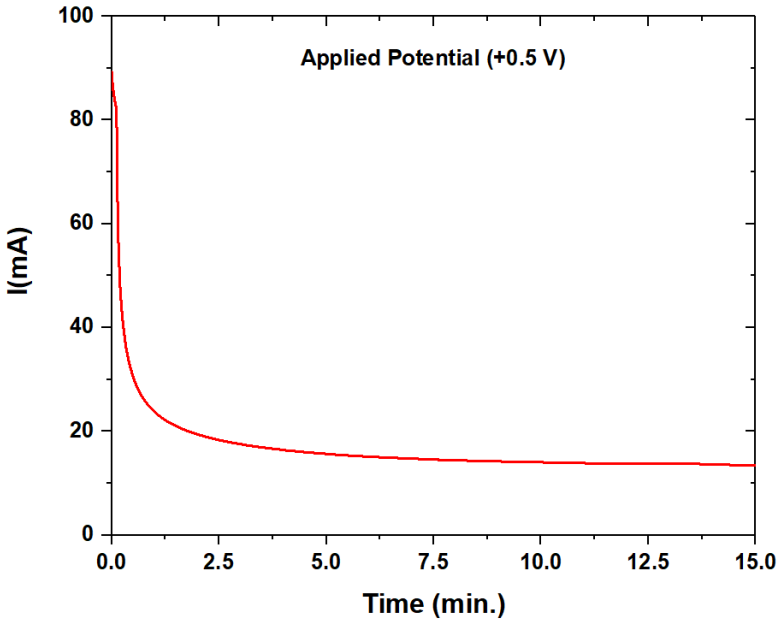

Figure 4.2: Chrono-amperometry transient at applied potential between +300 and +500mV, during 5 to 10 minutes for samples with no mechanical polishing; otherwise, the time for the transient must be for up to 30 minutes.

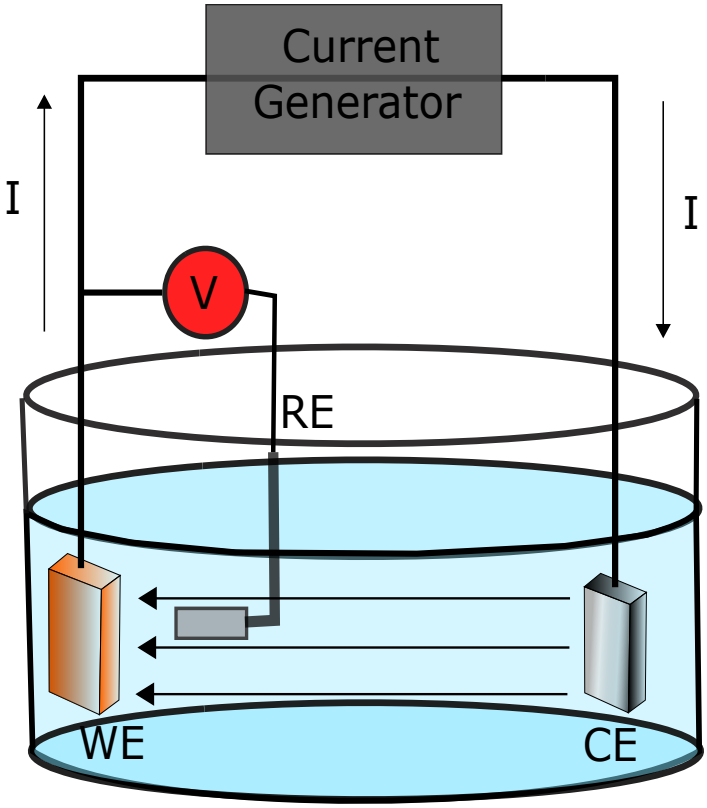

Figure 4.3: Electro-Polishing setup RE, CE and WE, are reference electrode, counter electrode (both made of platinum) and working electrode, respectively [39].

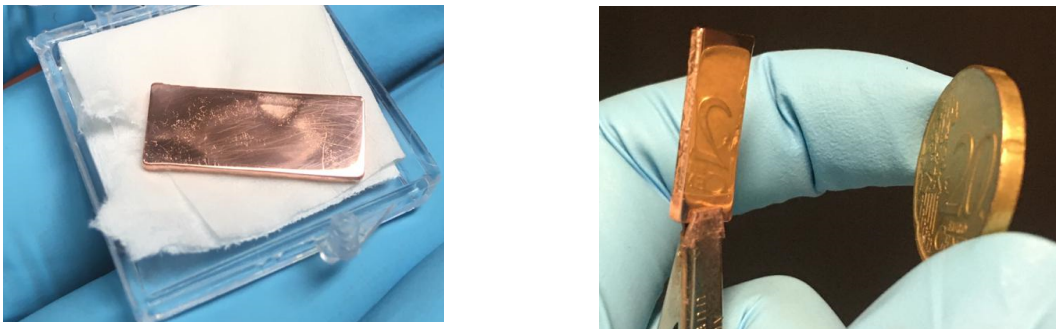

(a) (b)

Figure 4.4: Copper sample before a) and after b) electropolishing.

As it was mentioned above, it is necessary to remove the remaining H_3PO_4 after electro-polishing procedure, and the following steps are need:

- Fill a container with argon prior the electropolishing.
- Place 3 beakers with deaereted water inside the container already filled with Ar.
- Remove the sample from the container with H_3PO_4, and immerse it inside one beaker for 1 minute to remove the residuals of H_3PO_4.
- Repeat the same procedure as before in the next beaker for one minute.
- Remove te sample from the beaker and put a droplet of deaereted water on the sample to avoid oxidation before the assemble with the cell.

After the procedure outlined above and the Cu sample is attached to the cel. The cell must be filled with argon, then with HCl 10mM. all this must be done 2 hrs before the experiment to remove oxygen on the solution).

The last procedure is crucial in every experiment because if a small residue of contamination is present, like oxidation, the subsequent experiments (SE, RAS or EIS) are not reliable.

4.1.2 Reference Electrode (RE)

The RE is connected through a high-impedance element to the potentiostat. This ensures that no current flows through the RE. However, in electrochemistry the situation is significantly more complex. In a normal circuit, the voltage probe is assumed to be stable. However, in the case of a RE in electrochemistry the measured potential might be different depending on the electrolyte concentration on the RE material itself and its reactivity in the solution, and therefore the RE cannot be reliable during the experiment. To solve this problem electrochemists have been envisaged reliable REs for different experiments.

The idea is to have a durable non-reacting electrode with the possibility of using it in different experiments, thus most of the REs contain an isolated inner part which comprises a metal mesh (or a wire) dipped in an electrolyte solution with a well defined concentration. This inner part is placed encapsulated in a vessel (a tube) which is made of a non-dissociative material (normally a glass vessel). The inner part has an electrical connection and the glass has at its bottom an ion permeable porous section allowing ion exchange in one direction into the immersed solution for the electrical potential sensing. By using this RE configuration in a glass vessel, it is expected that the RE to be stable with a stationary double layer enclosing the metal part. Hence, it is possible to assign a constant potential with such a structure

since based on the Nernst Equation, a redox reaction in a defined solution concentration the RE has a constant standard potential at defined temperature and pressure (see, for instance, Eqs. 4.1 and 4.2).

Because the measurements in this work were done in HCl solution, it was decided to use a RE made of a Ag/AgCl wire. This was produced by electrodeposition of Cl on the Ag wire. The preparation of such a Ag/AgCl wire will be explained in the following section.

Such AgCl-coated Ag wire exhibits more durability in HCl and yields a minimum shift of the measured potential over long periods of time. The AgCl coating is fragile upon heating or UV illumination, and its solubility in water or diluted acids is low (520 μg/100 g H_2O at 50^{o}C).

The calibration for the Ag/AgCl wire was made in 10 mM HCl as follows. The potential of the Ag/AgCl wire in 10 mM HCl was measured against a commercial Ag/AgCl/3M NaCl (and/or against the micro-RE Ag/AgCl/saturated KCl). The potential shift was (+130±2) mV. This value has a good agreement with the calculation based on the Nernst equation,

$$AgCl + e^- \rightleftharpoons Ag + Cl^-, \qquad E^0_{Ag/AgCl} = 0.0V, \tag{4.1}$$

$$E_{Ag/AgCl} = E^0_{Ag/AgCl} + 0.059log\frac{[AgCl]}{[Ag][Cl^-]} \quad = \quad 0.0 + 0.059log\left(\frac{1}{10^{-2}}\right) = +0.118V. \tag{4.2}$$

4.1.3 Preparation of a Ag/AgCl reference electrode

The preparation of a Ag/AgCl wire is a straightforward procedure [40]. A silver wire soaked and cleaned in nitric acid should be connected as the WE. Another noble metal (platinum or gold) is used as counter electrode(CE) while the RE should be employed to read and ensure the applied potential; for this purpose a commercial Ag/AgCl/3M NaCl solution was selected and 1 M HCl is used as the electrolyte solution. The potentiostat runs 10 CVs from -300 to 300 mV. In this range the silver wire adsorbs chloride in anodic potentials and desorbs it at cathodic potentials. Repeating the cycles of adsorption/desorption produces a rough surface on silver that increases the surface area on the Ag−wire. After completing 10 cycles, chloride ion deposition should be done by polarizing at -100 mV for 2 minutes and then at +100 mV for 10 minutes. Finally, the electrode is taken out and rinsed with ultra pure water and dried in air. If this wire is used as the RE (as it is common in the RAS Electrochemical cell), the potential of the electrode should be calibrated based on each solution concentration by measuring with a potentiostat or a voltmeter against a known electrode. The calculation from the Eq. 4.1 should give the same shift as the measured one. Figure 4.5 shows the related voltammogram of a silver wire in 1M HCl related to the experiment for preparation of the Ag/AgCl RE.

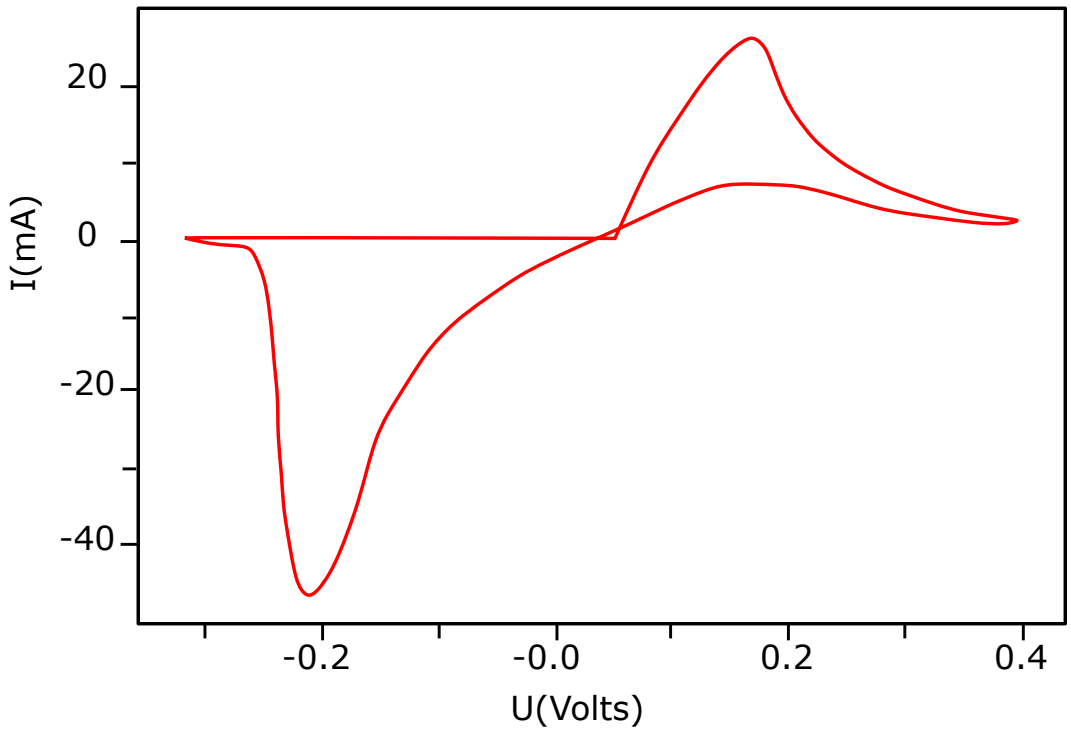

Figure 4.5: Typical voltammogram of a Ag wire immersed in 1 M HCl. The potential is measured against a commercial Ag/AgCl/3M NaCl reference electrode.

4.1.4 Electrolyte preparation

All electrolyte solutions were prepared from highly pure chemicals produced by Merck KGaA. The purity grade is called Suprapur ®. For the desired concentrations, the solutions were diluted using ultra pure water (18.2 MΩcm) from Smart2pure 12 UV TKA, which reduces the total organic contents to less than 5 ppb and the amount of the particles bigger than 0.2μ m to less than 1/ml. The purity of solutions is a crucial issue for the optical experiments. Unlike UHV, in solutions the mass transport, particles interactions, and electric fields within the electrical double layer near the surface are enhanced. Any measurable traces of constituents in the solution can be transported through the solvent molecules and interact with the surface; moreover, ions in the solution might be interacting with each other. Under the influence of the potential, it is likely to have oxidations/reductions which introduce new cations/anions complexes. In general, cations/anions make different complexes with solvent molecules. Prior to any experiment, all solutions must be deaerated for a couple of hours. By purging the solutions with 99.999% pure argon (argon grade 5.0), which promotes oxygen removals away from the solution. Note than argon is heavier than oxygen and removes it out of the solution.

The containers and volumetric flasks were cleaned before the first use based on the common rules of the chemistry lab and restrictions imposed by Electrochemical-Optical experiments demands. Therefore, the cleaning procedure for tools and glasswares were done on three different levels: (1) Soaking in piranha solution, which is a 3:1 (or 1:1) mixture of concentrated sulfuric acid and hydrogen peroxide solution. More than 50% hydrogen peroxide in the mixture is highly explosive. The Piranha is highly oxidative and removes metals and organic contamination. (2) Rinsing with deionized water to remove the etching products. (3) Several steps of sonification and rinsing in between with ultra pure water (18.2 MΩcm).

4.2 Cyclic Voltammetry set-up

In-situ cyclic voltammetry and RAS experiments were performed in a home-made electrochemical cell (ECC) based on polyetheretherketon with an opening end at the top for optical experiments. The Cu sample was attached from the bottom with an o-ring so that only the (110) surface was in contact to the electrolyte. The ECC is introduced into a gas-tight chamber filled with Ar to provide an inert atmosphere. The 10 mM/L solution of HCl is supplied to the cell after mounting it inside the chamber. CV measurements were performed in a three-electrode configuration using a potentiostat (Ivium Technologies B.V., CompactStat). A Pt and Ag/AgCl wire [40] were used as counter and quasi-reference electrode, respectively .

All measured potentials are calibrated against a classical Ag/AgCl reference electrode in 3 M/L NaCl. CV scans, measured before and after any experimental run, indicate the successive protection of the electrolyte and the sample against (oxygen) contaminations. The Cu(110) single crystal is set as the working electrode with a rectangular area of ≈ 0.72 mm^2 exposed to the electrolyte. All the solutions introduced into the system were deaerated by bubbling with Ar for 2 hours prior the experiment. The Cu(110) sample was supplied by MaTeck GmbH, with an orientation accuracy better than 1°. As received samples have a 99.999 % purity with a surface roughness less than 30 nm. Native oxides were removed by electropolishing in a 85% ortho-phosphoric acid for several minutes at an applied voltage of +0.5 V until the surface appearance became mirror like [7, 39]. The residues of electropolishing process were removed by dipping the sample into an ultrasonic bath with deaerated ultrapure water (18.2 MOhm) under Ar ambient. Hydrochloric and phosphoric acids were supplied by Merck KGaA (Suprapur® grade) and ultrapure water was used to prepare the electrolyte solutions.

4.3 Reflectance anisotropy spectroscopy set-up

The optical arrangement of the RAS system is a home made instrument according to the design by Aspnes *et al.* [26]. The core of the system comprises three optically active elements: a linear polarizer, a 50 KHz photoelastic modulator (PEM) and an analyzer. The sample was oriented in a way that x and y axes corresponded to the $[1\bar{1}0]$ and [001] crystallographic directions, respectively. The measured in-plane optical anisotropies are averaged over the area of the light spot, which was half the size of the sample area exposed to the electrolyte. The covering electrolyte is optically isotropic and the back reflection from the air-water interface was avoided by a small tilting of the ECC. All the measurements were performed at room temperature (22 °C).

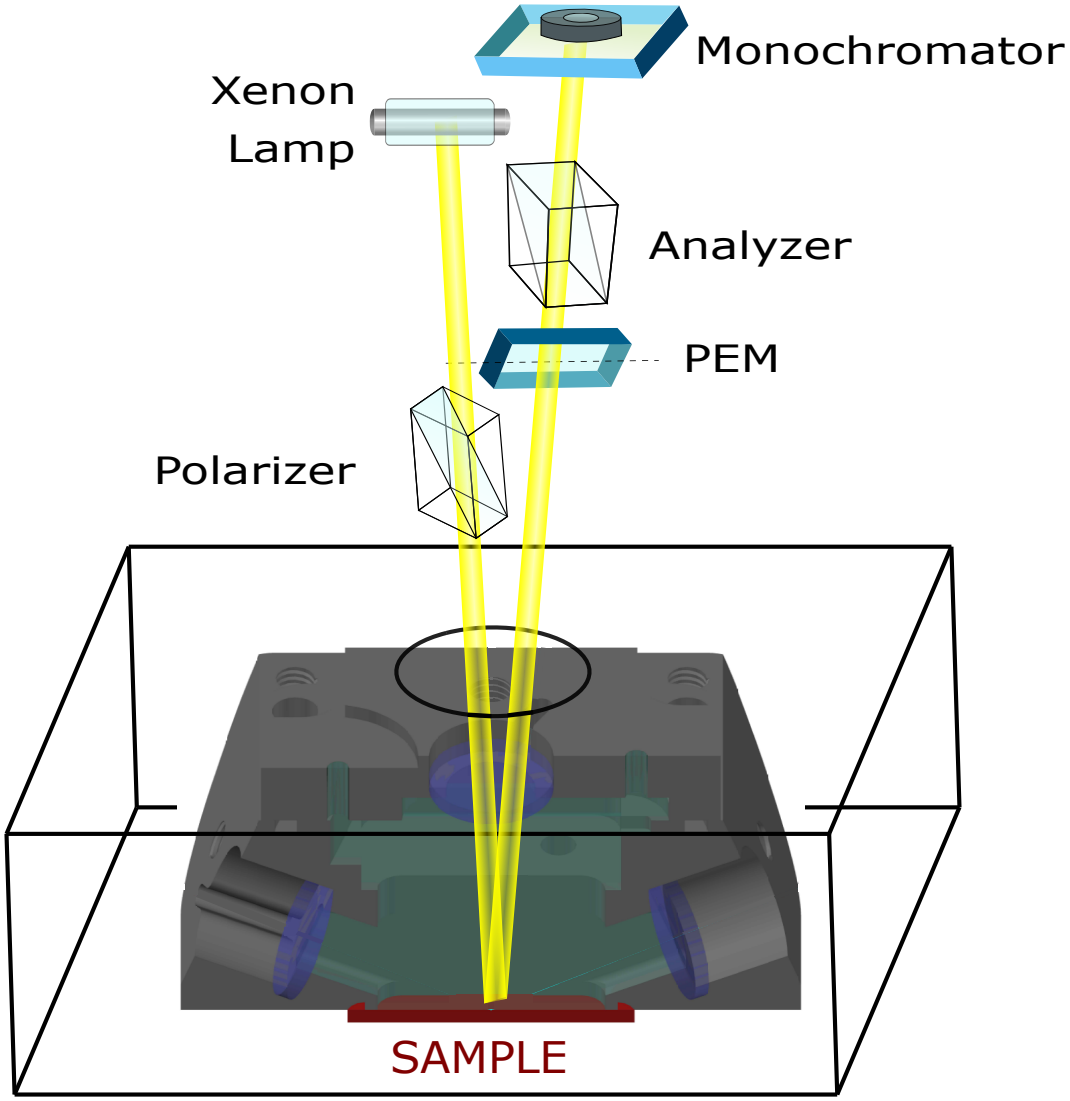

Figure 4.6: Reflection anisotropy spectroscopy adapted to the electrochemical Cell, PEM stands for photo elastic modulator operated at 50 kHz.

4.4 *In - situ* spectroscopy ellipsometry

For the *in- situ* ellipsometric measurements a spectroscopic rotating compensator instrument (J. A. Woollam Co., Inc., M-2000DI) was used. An incident angle of 68° was predefined by the electro-chemical cell geometry. The change in the light polarization upon reflection on the sample is recorded by means of the ellipsometric angles Ψ and Δ which account for a polarization rotation and the phase shift between polarization components parallel and perpendicular to the plane of incidence. The rotating compensator (PCRSA) configuration of the instrument enables a full-range determination of Δ with uniform sensitivity [41]. A possible strain-induced birefringence in the fused silica cell windows was determined with a standard Si wafer before each experiment, and all presented results are corrected to that effect. Two spectrographs as well as a combination with tungsten-halogen and deuterium light sources allows for a parallel measurement of 700 wavelengths covering a spectral range from 193 to 1690 nm (6.4 to 0.76 eV). The ellipsometric spectra were recorded synchronized with CV to obtain real-time in situ optical responses for variable electrochemical potentials. The integration time for each spectrum was set to 5

sec. The latter intervals still allow a time-resolved monitoring of interface processes if we regard potential sweep rates around 5 mV/s. All measurements were performed at room temperature. The Cu(110) sample was mounted with the [001] in-plane surface direction 45 ° rotated against the intersecting line of the surface plane and the plane of light incidence.

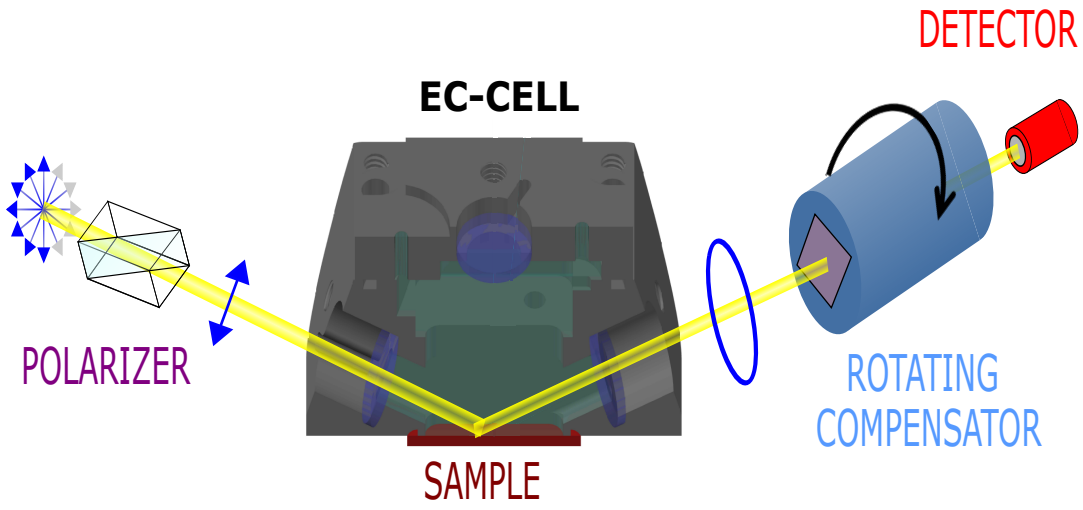

Figure 4.7: Spectroscopy Ellipsometry adapted to the Electrochemical Cell.

5 Cu single crystals in HCl solution

This chapter discusses the Copper-chloride complexes as well as the mechanical and kinetic reactions that occur in the Cu(111) and Cu(110) surfaces.

5.1 Copper-Chloride complexes

Most theoretical and experimental studies have been done for copper surfaces exposed to eletrochemical reactions in hydrocloric solutions and the obtained results indicate the occurrence of different Cu-Cl complexes in the solution and mainly at the interface region. Generally speaking there are exist several types of ionizations of Cu, both cupric (Cu(II)) and cuprous (Cu(I)) chloride complexes have several forms. For Cu(II) there exist at least five possible species: Cu^{2+}, $CuCl^{+}$, $CuCl_2$, $CuCl_3^{-}$, and $CuCl_4^{2-}$, whereas for Cu(I) there are at least six possible complexes: Cu^{+}, CuCl, $CuCl_2^{-}$, $CuCl_3^{-2}$, $Cu_2Cl_4^{2-}$, and $Cu_3Cl_6^{3-}$. The distributions and ratios of such complexes depend strongly on the concentration of copper ions and the free chloride concentration [42]. For systems under electric potential control, such potential can influence the ratio of the complexes as well. J. J. Fritz [43], calculated the concentration of Cu(I)-Cl complexes *vs.* HCl concentration as the solvent for the solid CuCl. As a result, Fig. 5.1 (from J. J. Fritz[43]) represents the pertinent fractions of those complexes. Therefore, one can conclude that under thermodynamic equilibrium, in a system of Cu in dilute HCl solution the predominant complex is $CuCl_2^{-}$. The relative stability of Cu(I)-Cl and Cu(II)-Cl complexes at different temperatures have been discussed further in [42, 44, 45].

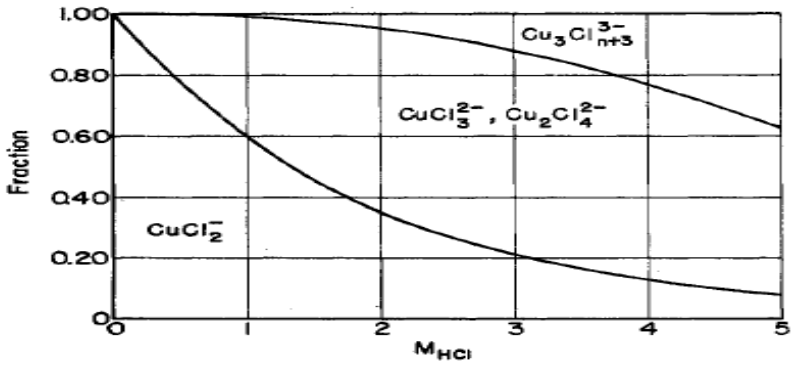

Figure 5.1: Distribution of dissolved CuCl between single, doubly, and triple charged complexes as a function of the HCl molarity at 25 °C (graph taken from J. J. Fritz [43]).

Another relevant fact about copper-chloride species is that the coordination by chloride ions stabilizes the Cu(I) species so that the oxidation/reduction of Cu is done in the following steps (Cu $\longleftrightarrow$ Cu(I) $\longleftrightarrow$ Cu(II)) rather than direct. Under potential control, however, the occurrence and stability of Copper-chloride compounds can be considered in more detail by the so called Pourbaix diagrams[45, 46]. Pourbaix diagrams are representatives of different stable phases over the specific ranges of applied potential with respect to the pH of the electrolyte solution. The Pourbaix diagram for the aqueous copper-chloride ([Cl^-] = 355 ppm) system is shown in Fig. 5.2. The chloride concentration of 355 ppm is exactly the same as the concentration of a 10 mM HCl solution, which was used in the experiments of the present thesis. For pH = 2, at negative potentials, there is a range where Cu is stable. Moving to potentials more positive than the hydrogen evolution potential, $CuCl_2^-$ occurs and becomes more stable related to metallic Cu. Further, a solid CuCl phase might form from the metallic Cu or from the Cu^+ species. If the potential is set more positive than +0.4 V, copper starts to dissolve as Cu^{2+}. It is important to note the possible stability range for each component that might not be readily deduced from a Pourbaix diagram.

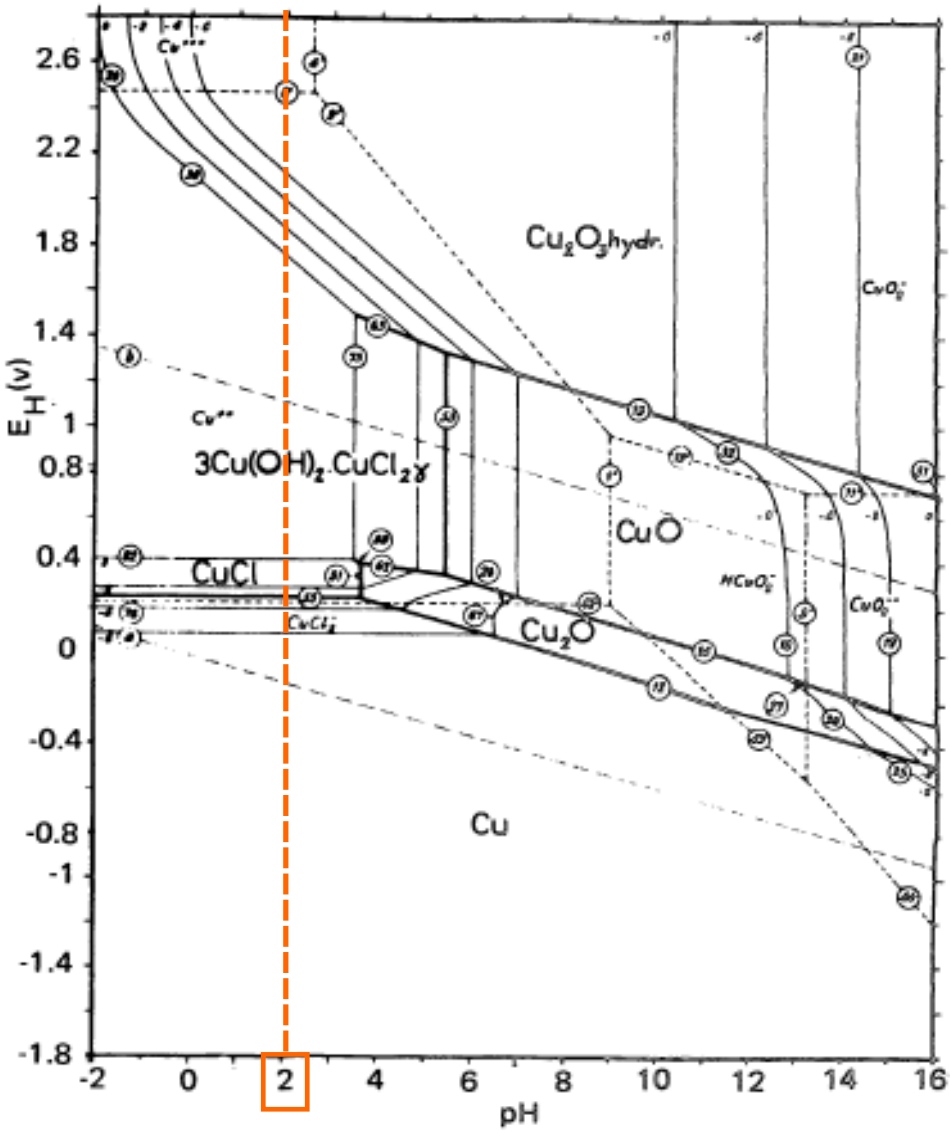

Figure 5.2: Pourbaix diagram for the aqueous copper-chloride ([Cl^-]= 355 ppm) system. The chloride concentration of 355 ppm is the same as the concentration of a 10 mM HCl solution, which was used for the present Thesis. Figure taken from [47].

Based on the Nernst equation for any redox couple there is a standard potential E^0 which describes the relative concentrations of the redox species and the applied potential E as follows:

$$ox + ne^- \rightleftharpoons red,$$

$$E = E^0 + \frac{0.059}{n} log \frac{[ox]}{[red]}, \tag{5.1}$$

where the parameters inside the square brackets account for the related activities (or equivalently, the concentrations for diluted solutions) of the species. This means that at the standard potential E^0, the relative concentration (or activity) of the redox couple is 1, and if the potential is shifted from the standard potential, the relative concentrations of the redox couple change as well. The regions where metallic Cu is stable are called immunity regions, corresponding to more negative potentials. On the

other hand, there are potential ranges where Cu(I) or Cu(II) are stable with respect to Cu. These are called corrosion regions. At higher pH values copper oxides form and passivate the surface. These areas in the Pourbaix diagrams are classified as passivity regions.

5.2 Cyclic voltammogram of Cu (111) and Cu (110)

Figure 5.3 shows the cyclic voltammogram (CV) results for Cu(111) in 10 mM/L HCl solution measured at a rate set to 20 mV/s. The potential window is limited between −10 and −730 mV, thus avoiding Cu^{2+} dissolution in the anodic direction and the hydrogen evolution reaction (HER) in the cathodic direction. The characteristic peaks of the specific adsorption and desorption of Cl are labeled in Figure 5.3 with A in the anodic and with A' in the cathodic scans, respectively. These assignments are based on previous studies of the Cu(111) HCl system. The potential range above peaks A and A' is related of a double-layer region with a geometry ($\sqrt{3}$ x $\sqrt{3}$) R30° Cl^- adsorbate-induced structure as confirmed previously by electro-chemical scanning tunneling microscopy (EC-STM)[48]. At more negative potentials before peak A and after A' a (1x1) bare Cu(111) surface is observed[48]. The overall integrated charge transfer in A is almost the same at different scan rates as can bee seen in figure 5.5. An ideal ($\sqrt{3}$ x $\sqrt{3}$) R30° coverage on the Cu(111) surface with Cl^- comprises 5.87×10^{14} Cl-ions per cm^2, which corresponds to an ionic charge in the inner Helmholtz layer(IHL) of $Q = 94 \mu C/cm^2$. Respective calculations for the charge transfer in the case of the Cl desorption in peak A' require a decoupling of the overlapping Faraday current of the HER. The charge transfer remained, nevertheless, roughly a factor of 2 larger than that in the Cl adsorption peak A. In order to observe this, the exponential Faraday current needs to be subtracted from the total cathodic current.

The difference between electron charge transfer (Cl^- adsorption and Cl^- desorption) was already observed in previous studies of the Cu surface in acidic environments [48]. This difference is attributed to the so-called Frumkin effect [20], which describes a charge inversion at the electrode surface resulting from specific anion adsorption at cathodic potentials. The latter case creates a negative proximity effect and thus an enhancement of the adsorption and catalytic reduction of hydrogen. The attraction of cations like H^+ or H_3O^+ to the Cu(111) surface thus increases the exchange current density of the HER. Conversely, a desorption of the Cl^- reduces also the exchange current density of the HER, which explains the apparent discrepancy in the amplitude of peak A' even after having subtracted the measured exponential increasing Faraday current at more cathodic potentials.

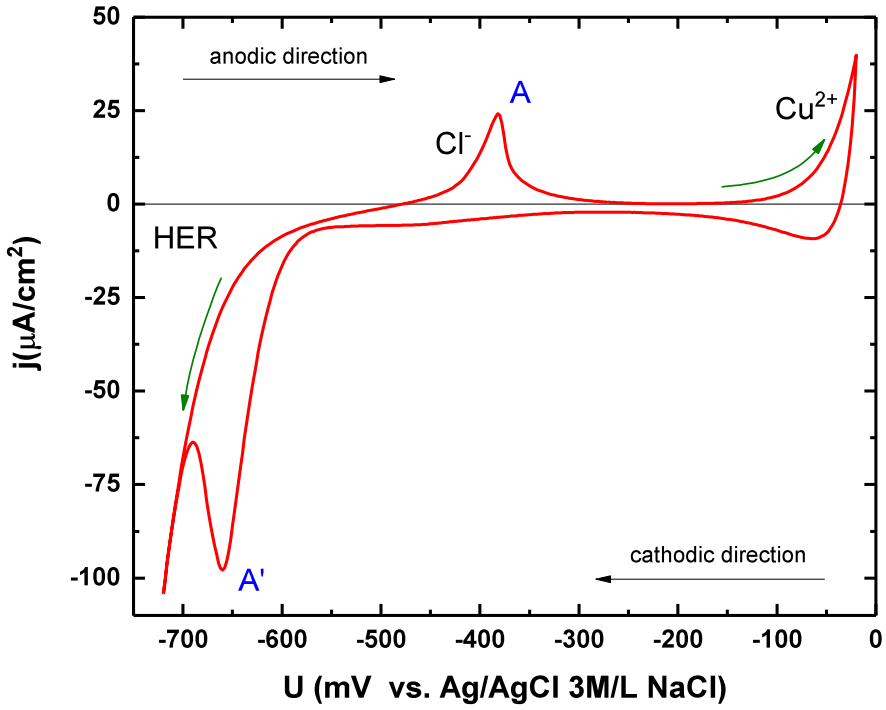

Figure 5.3: Cyclic voltammogram for Cu(111) in 10 mM of HCl recorded at scan rates of 20 mV/s a ($\sqrt{3}$ x $\sqrt{3}$)$R30^\circ$ is seen between -600 and -450 mV in anodic direction.

Figure 5.4 shows a CV recorded for the Cu(110) surface with a scan rate set to 20 mV/s. The scanning range from -60 to -600 mV is again limited by the Cu^{2+} dissolution in the anodic and by the hydrogen evolution reaction (HER) in the cathodic scan, respectively. In the case of the Cu(110) surface, high Cu^{2+} dissolution as well as hydrogen evolution rates are avoided to prevent irreversible surface modifications [49]. In between are observed two characteristic peaks in the anodic as well as in the cathodic scan direction in agreement with previous studies [50, 7] These both relate to the Cu(110)-surface reactions with Cl ions and are labeled with A/A' and B/B', respectively (Figure 5.4). A and A' are assigned to a Cl-adsorption and desorption, respectively. Both amplitudes and shapes of the peaks labeled as B and B' depend strongly in contrast to A and A', on the scan speed. B and B' as well as the plateau region with elevated Faraday current at potentials more positive than B and B', result from reactions where Cu-Cl precipitates near the surface. The following reaction steps are commonly accepted :

1. $Cl^-_{aq} \rightleftharpoons Cl_{(ad)}$

2. $Cu_{(bulk)} + Cl_{(ad)} + Cl^-_{(aq)} \rightleftharpoons [CuCl_2]^2_{(aq)}$

3. $Cu_{(bulk)} + Cl_{(ad)} \rightleftharpoons CuCl_{(s)}$

Reaction 3 creates the passivating aggregate layer that covers the Cu surface and thus inhibits the further Cu-Cl interactions. It was also shown in reference [50], that the adsorption of Cl^- initiates a sequence of morphology transformations at the Cu (110) surface.

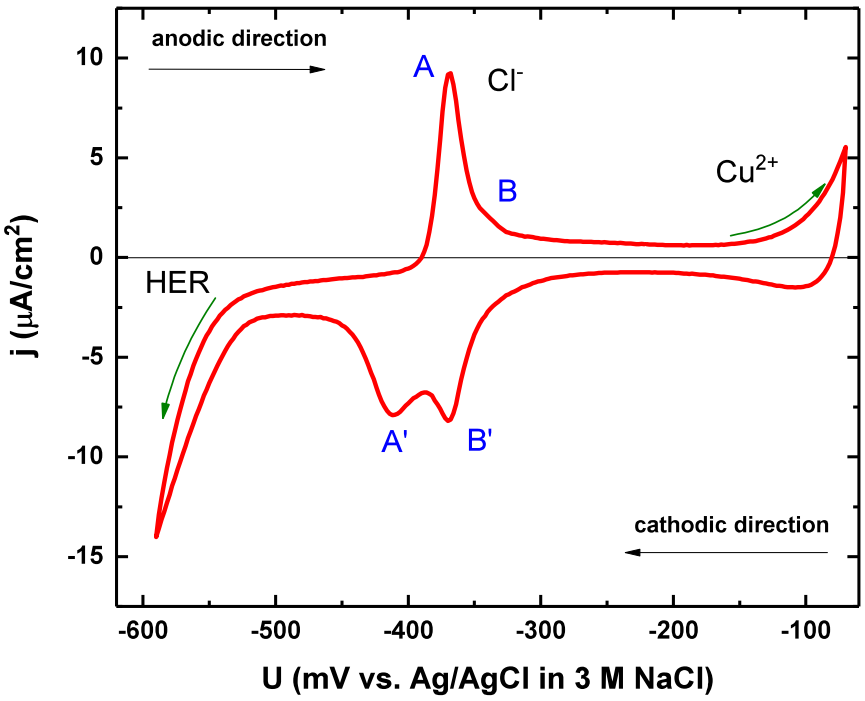

Figure 5.4: Cyclic voltammogram for Cu(110) in 10 mM/LHCl recorded at a scan rate of 20 mV/s.

The description of the peaks in the cyclic voltammogram of Cu (110) is significantly more complicated than the above description, however all the respective reactions take place. A more detailed description is carried out in chapter 6 where, with the aid of RAS and with half cycles in both cathodic and anodic directions, the mixing up of the corresponding reactions at certain applied potentials is shown.

5.2.1 Importance of the Scan Rate

As it is shown in Figs. 5.5 and 5.6, as the scan rate is variated from 20 mV down to 2 mV per second, there is clear a shift in peak A in copper (111) from -360 up to -450 mV and for copper (110), for peaks A and B there is a shift around 40 mV at more negative potentials. Note that the change for (110) is not as big as for (111). This shift in the peaks is due to different scan rates.

Therefore, the scan rate of the experiments controls how fast the applied potential is scanned. Faster scan rates lead to a decrease in the size of the diffusion layer; as a consequence, higher currents are observed [22]. For ideally electrochemically reversible electron transfer processes involving diffusing redox species, the Randles-Sevcik Eq. 5.2 describes how the peaking currents in our copper single crystals could increase linearly with the square root of the scan rate $v(Vs^{-1})$:

$$i_p = 0.446nFAC^0 \left(\frac{nFvD_0}{RT}\right)^{1/2}, \tag{5.2}$$

where n is the number of electrons transferred in the redox processes, A(cm^2) is the electrode surface area, D_0 (cm^2s^{-1}) is the difussion coefficient of the oxidized analyte, C^0 (mol cm^{-3}) is the bulk concentration of the analyte, and F F is the Faraday constant.

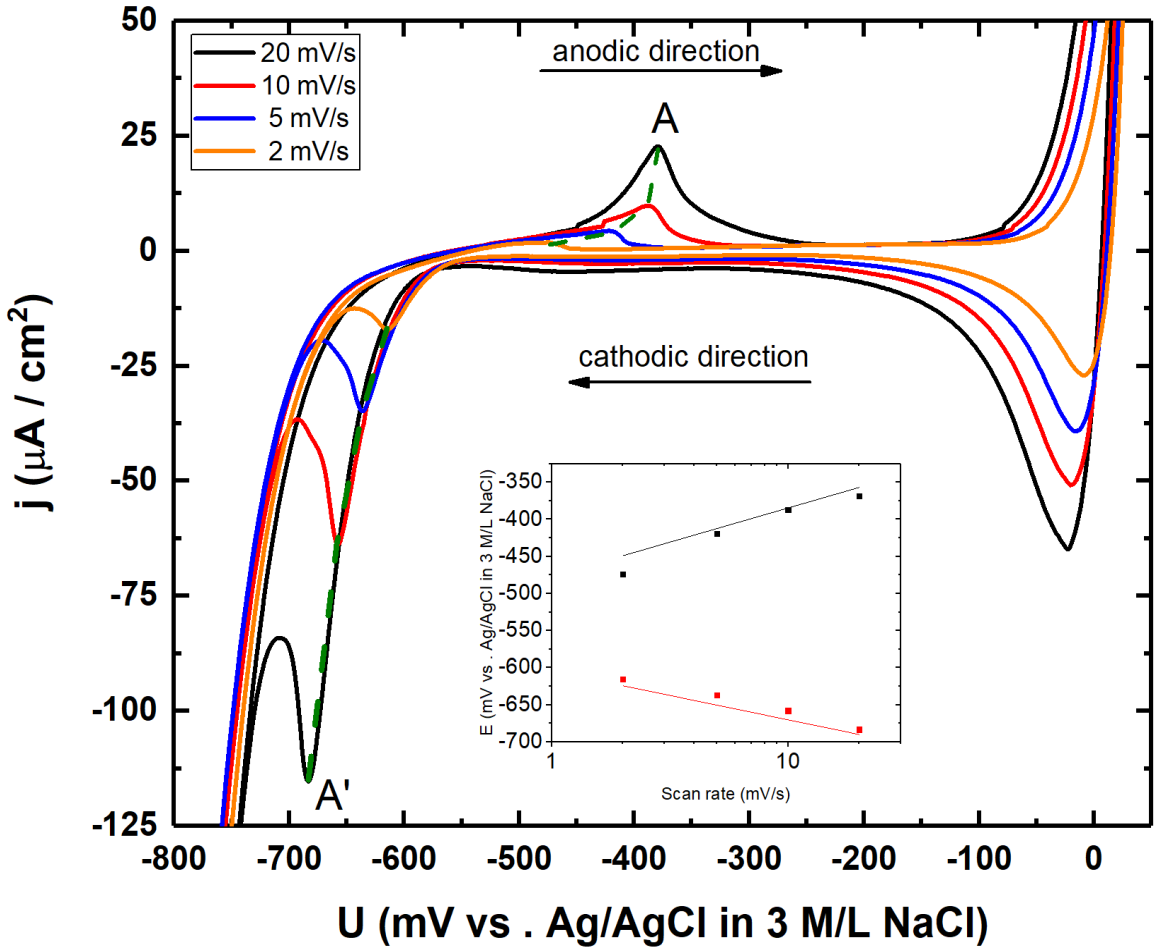

Figure 5.5: Cyclic currentpotential plots for Cu(111) in 10 mM/LHCl recorded at different scan rates (2 mV/s, orange; 5 mV/s, blue; 10mV/s, red; and 20 mV/s, black). The inset shows the shifts in peaks as a function of the scan rate.

The Randles-Sevcik equation can hints indications as to whether an analyte is freely diffusing into the solution. As analytes can sometimes adsorb to the electrode surface, it is essential to assess whether an analyte remains homogeneous in solution prior to analyzing its reactivity. In addition, to verify that the analyte is diffusing freely the RandlesSevcikequation may be used to calculate the diffusion coefficients.

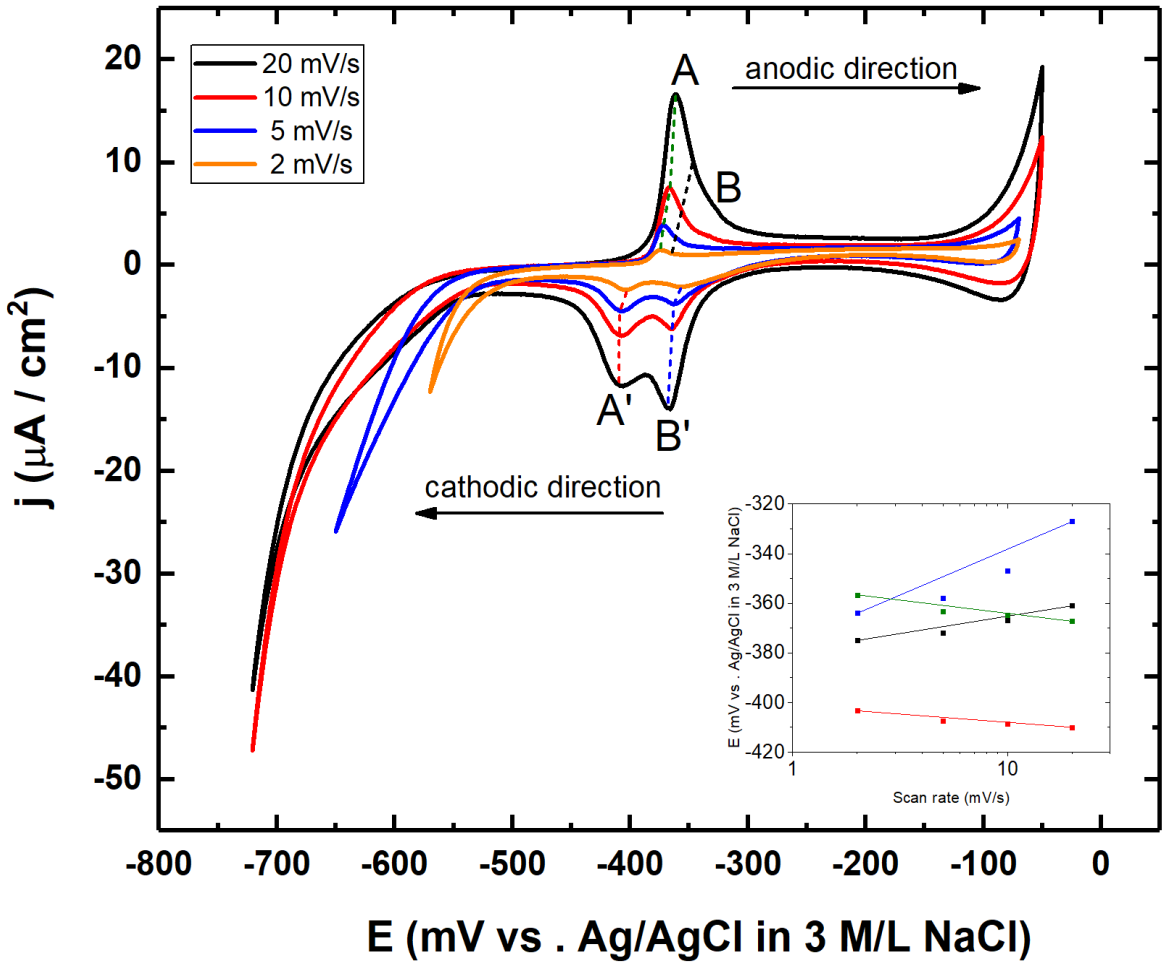

Figure 5.6: Cyclic currentpotential plots for Cu(110) in 10 mM/LHCl recorded at different scan rates (2 mV/s, orange; 5 mV/s, blue; 10mV/s, red; and 20 mV/s, black). The inset shows the shifts in peaks as a function of the scan rate.

All these reactions related to peak shifts are related to a change in scan rate, but the mechanism that controls this process is not yet described.

5.2.2 Mechanism for overpotentials

In the literature the activation overpotential is mentioned in connection with:

- Surface conversions preceding the electron transfer; including rearrangements of reactant molecules, adsorption to the electrode surface, chemical reactions such as protonation or complex disassociation, etc.
- Electron transfer at the electrode surface.
- Surface conversions following the electron transfer; including chemical reactions, desorption from the electrode surface, insertion of metal cations into the crystal lattice, etc.

The use of the term overpotential in this thesis, in general, corresponds to a specific type of overpotential (activation overpotential). As will be mentioned in the following chapter, concentration changes in the bulk of the electrolyte are not expected. All currents measured in the CV experiments are those from sub-monolayer adsorption, dissolution, etc; therefore the mechanism that controls our system is by an

activation barrier. The assumption was tested already before by correcting our CV measured at different scan speeds. Therefore, we assume that the overpotential n is connected to the measured current by:

$$j = j_0 exp(\alpha F \frac{n}{RT}). \tag{5.3}$$

Equation 5.3 corresponds to the Butler-Volmer equation. As shown in Fig. 5.7, below the maximum current peak at potential around -375 mV, this peak match for all CVs after a respective shift of the potential U which was calculated by adapting only j_0 and α.

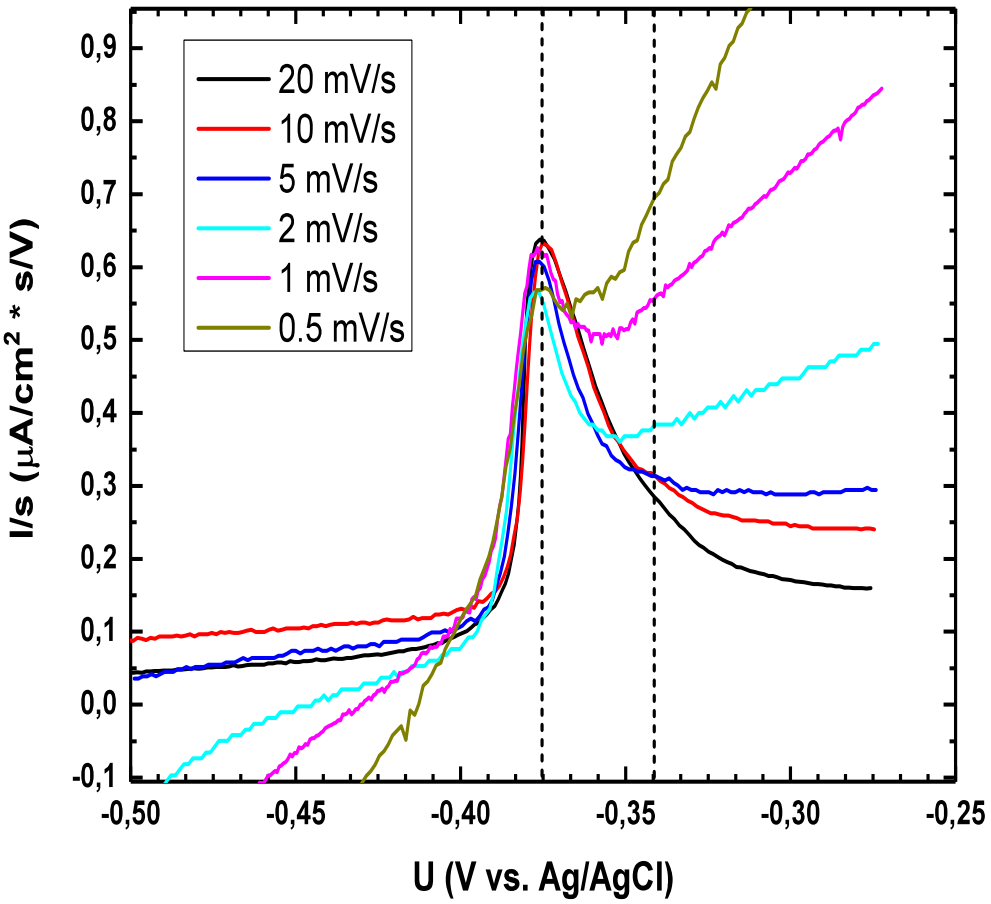

Figure 5.7: CVs of Cu (110) of the correction overpotential for different scan speeds given by the Butler-Volmer equation 5.3, the dashed lines are a guide to the eye to distinguish the potential at which the peaks of different scan speed match.

In Fig.5.8 shows the shift of the peak potential with different scan speeds rates. At the lowest scan speeds, the peak potentials tend to convert to the equilibrium potential as it was found with the ButlerVolmer equation 5.3 above, and also with impedance experiments.

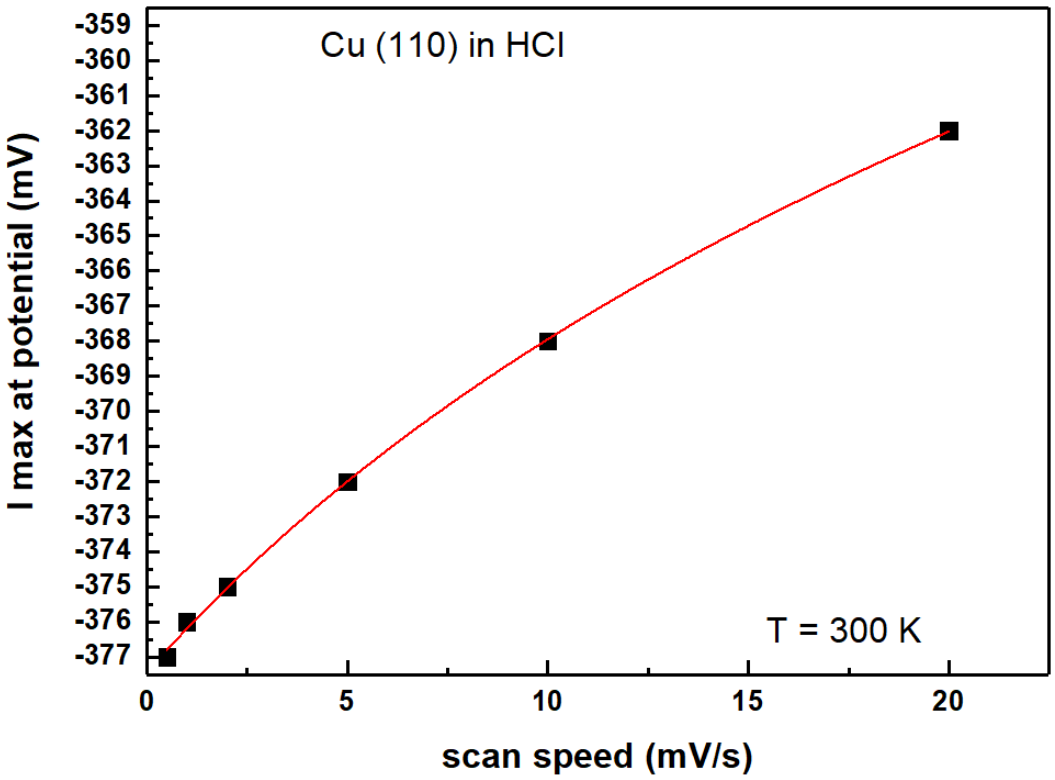

Figure 5.8: Black squares track the maximum of peak A appearing in CV experiments for Cu(110) in HCl solution at different scan speeds. The fit is indicated with a red line.

6 Results and discussion

6.1 Adsorbate Isotherm Analysis by Reflection Anisotropy Spectroscopy of Cl^- on Copper (110) in Hydrochloric Acid

When foreign ions or molecules adsorb on metals they cause changes in their surfaces. Such surface modifications are complex and deserve detailed studies in any environment. As a matter of fact, in ultra-high vacuum (UHV), molecular chlorine (Cl_2) adsorption on Cu(110) has been extensively studied with scanning tunneling microscopy (STM) and low energy electron diffraction (LEED) [51, 52]. In liquid environments, atom species are prone to alter the liquid-metal interface in a different way; *i.e.,* ions are adsorbed instead of neutral atoms and molecules. In electrochemical conditions, for instance, electron-based probes (like LEED) are clearly incompatible, and therefore non-invasive analytical techniques are much preferred

Specifically, we demonstrate the power of RAS as an analytical probe capable to measure the complex reaction of chlorine ions Cl^- adsorption on low index metal surfaces. A special attention is paid on the possibility to quantify certain surface structures and to derive respective thermodynamic potentials. In a previous work we could show by EC-STM that the Cu(110) surface structures change in several steps due the anodic adsorption of cloride [50, 53]. Most prominent is the formation of a stripe/groove-structures in the [001] surface direction. The latter are about 2.6 nm wide and keep a minimum distance of the same order. A second major surface oxidation step results in a faceting of the surface. When using the appropriate photon energy, *in operando* kinetic RAS is able to detect electrosorption isotherms of Frumkin type for these Cl^- induced structuring.

The relationship between the polarization optical response as determined with RAS and the adsorbate induced surface structures on one hand, and to the currents measured (*e.g.,* in cyclic voltammetry (CV)) on the other hand, needs to be clarified first.

6.1.1 RAS - a measure of surface adsorbates

Chemical bonds, whether they are of ionic, covalent, or even weaker of Van der Waals type, increase the concentration of species (ions) at an electrochemical interface. In the picture of the electrochemical double layer structure, such species are transferred either from the bulk electrolyte or from the outer to the inner Helmholtz layer to the surface during the adsorption process [54]. The amount of adsorbed

species is usually given in terms of the relative coverage:

$$\Theta = \frac{\Gamma_I}{\Gamma_{I,max}}, \tag{6.1}$$

which describes the fraction of the electrode surface coverage Γ_I with respect to the maximum value $\Gamma_{I,max}$ of the respective adsorbate type at a certain absorption site.

RAS measures at normal incidence, as a function of photon energy, the difference in reflectivity between two orthogonal in-plane directions, r_x and r_y:

$$\frac{\Delta r}{r} = 2\frac{r_x - r_y}{r_x + r_y}. \tag{6.2}$$

The two reflectivities r_x and r_y are in general; *i.e.,* in case of absorbing materials, complex entities leading to relative amplitude and phase changes. In our experiments we measure both the real and imaginary parts of $\Delta r/r$. For a planar interface between two isotropic media, r_x and r_y can be calculated with the Fresnel equations [55]. Our angle of incidence is $\phi \approx 0$. For an isotropic interface between the cubic copper and the electrolyte (water), we would obtain $\Delta r/r = 0$. The Cu(110) surface, however, appears to be intrinsically anisotropic due to the reduced symmetry of the respective surface unit cell. Such a situation can be approximated by a so called optical "3-phase model". From now on, the interface is represented by the half infinite substrate (our cubic single crystal $Cu_{(bulk)}$), by the half infinite ambient (electrolyte in our case), and in-between by an anisotropic interface layer of thickness d. The substrate and ambient dielectric functions (DF) are ε_s and ε_a, respectively. The latter is a real number since the ambient is assumed to be transparent ($\varepsilon_a = n_a^2$). With the approximation $d \ll \lambda$ ($d \lesssim 1$ nm) one can show that [56, 57]:

$$\frac{\Delta r}{r} = -\mathrm{i}\frac{4\pi\sqrt{\varepsilon_a}}{\lambda(\varepsilon_s - \varepsilon_a)} d(\varepsilon_{o,x} - \varepsilon_{o,y}). \tag{6.3}$$

For solid-liquid interfaces we derived the latter expression including the ambient DF ε_a which is set equal to one in the majority of cases. For our purpose of low concentration hydrochloric acids, we use the DF of pure water (ε_a=$\varepsilon_{H_2O} \approx 1.33$) [58]. For the substrate DF, we use the Cu-DF measured *in-situ* in hydrochloric acids at electrochemical potentials where no surface adsorbates are detectable by EC-STM. The Cu Bulk-DF has been obtained with an optical layer model where surface charges are take into account in a separated layer contribution [7]. The term $\Delta(\varepsilon d) = d(\varepsilon_{o,x} - \varepsilon_{o,y})$ is regarded as the surface dielectric anisotropy (SDA).

Accordingly, $\Delta r/r$ as measured by RAS, is proportional to the SDA. The complex proportionality factor that includes the bulk dielectric properties is a constant, as we will consider only changes in the anisotropic surface response at a single wavelength. Note that the amplitude of the optical anisotropies measured during the chemical reaction are larger than the respective experiments performed in air or vacuum for the substrates, because of the higher refractive indexes of the surrounding liquids.

The connection between the coverage Θ of a certain adsorbate and the change in the SDA requires a critical analysis. Two major scenarios are conceivable. Surface adsorbates can change global surface properties as a function of the surface coverage Θ. Likely is, *e.g.,* a change in the electron excess Γ_e on the metal side of the interface. Such assessment is generally accepted because the Mott criterion remains always satisfied, and the copper surface maintains its metallic properties [7]. Indeed, spectroscopic ellipsometry experiments have shown this proportionality by means of the ellipsometric angle Δ and the electron excess Γ_e [7].

A second part concerns local changes of the surface due to the adsorbed (Cl^-) ions. The latter could generate, for example, new electronic resonances at adsorbate sites or in-between them. Local morphology changes like surface stripes, grooves, and facets which were reported for Cu(110)[50, 52], fall into the same category. In the long wavelength limit, where lateral structures are assumed to be much smaller than the wavelength, the measured SDA is an "average" between covered and uncovered surface areas. Without screening effects the effective SDA becomes a linear combination between two different surface dielectric

functions:

$$\Delta(\bar{\varepsilon d}) = \Theta\Delta(\varepsilon d)_2 + (1-\Theta)\Delta(\varepsilon d)_1, \tag{6.4}$$

where $0 < \Theta < 1$ denotes the surface coverage. In the maximum screening situation the two states add up reciprocally:

$$\frac{1}{\Delta(\bar{\varepsilon d})} = \Theta\frac{1}{\Delta(\varepsilon d)_2} + (1-\Theta)\frac{1}{\Delta(\varepsilon d)_1}, \tag{6.5}$$

which are the so called Wiener bounds [59, 60] and the actual value of the effective dielectric properties appears between these two extreme cases depending on the geometry of the structure. Nevertheless, the reciprocal averaging given by eq 6.5 is actually obtained only for a bulk structures consisting of 2D layers. For 1D structures on a surface, the effective dielectric relationship tends to be linear. Furthermore, one should note that Eq. 6.5 attains a linear dependency for the limit $\Delta\varepsilon_0 \ll \varepsilon_0$.

6.1.2 The adsorption isotherm kinetics in RAS-transients

A comprehensive discussion of the physics and chemistry of adsorption isotherms was presented for example by J.O'M. Bockris, *et al.* [21]. For the interpretation of our *in-situ* optical results, it is important to bear the following aspects in mind.

The adsorbed (Cl^-) ions may have a concentration c_I in the bulk of the solution. The variation of the coverage Θ, depending either on c_I or the applied electrode potential, is known as the adsorption isotherm. A typical surface has 10^{14} - 10^{15} cm^{-2} atoms in the uppermost layer, whereas the number of adsorption sites is typically less. The used electrochemical cell employed in the present work, on the other hand, has a volume of 1 cm^3. By using an concentration of $c_I = 10$ mM, the number of ions in the solution is about 6×10^{18} and is thus $(3-4)$ orders of magnitude higher than the number of possible adsorption sites. Therefore, we regard the concentration c_I in the bulk of the electrolyte as a constant. The change in the Gibbs energy G of the electrochemical adsorption/desorption of an ion in equilibrium is thus:

$$0 = \Delta G = \Delta G_0 + eU + \Delta G_X(\Theta). \tag{6.6}$$

The first term (ΔG_0) in eq 6.6 contains the constant formation energy of the adsorption of an isolated ion, and also includes the constant activity of the respective ion in the solution, $kT\ln(c_0/c_I)$. The second term accounts for the applied working electrode potential U *versus* the reference electrode. In a rigorous discussion it depends on the vertical position of the ion in the outer Helmholtz layer before and in the inner Helmholtz layer after adsorption as well as on the water molecule configuration near the surface. The third therm adds all contributions dependent on Θ. For $T = 0$ K and for the adsorption of isolated ions it would be constantly zero and the surface coverage depending on the applied potential would change as a step like function. However, at temperatures different from zero, at least an entropy related continuous potential change has to be considered because the number of possible surface coverage realizations has a maximum at $\Theta = 0.5$ [20]. The simplest possible model, in which adsorption occurs, is thus the so called Langmuir isotherm:

$$0 = \Delta G_0 + eU + \frac{kT}{n}\ln\left(\frac{\Theta}{1-\Theta}\right), \tag{6.7}$$

where n is the number of ions and e is electron charge. RAS-transients should resemble the hereby defined dependency of Θ on the applied potential U if we consider a linear relation between the SDA and Θ (eq 6.4). A relatively simple extension of the Langmuir isotherm is the Frumkin isotherm where the interaction between ions is taken in to account by an additional linear term in Θ [61]:

$$0 = \Delta G_0 + eU + \frac{kT}{n}\ln\left(\frac{\Theta}{1-\Theta}\right) + w\Theta. \tag{6.8}$$

Positive and negative values of w considers repulsive and attractive interaction between the adsorbed species, respectively. Figure 6.1a shows a Langmuir isotherm (solid line) and two Frumkin isotherms (dashed and dotted lines) in order to illustrate the connection to the RAS-Transient measurements which will be discussed in section 4.

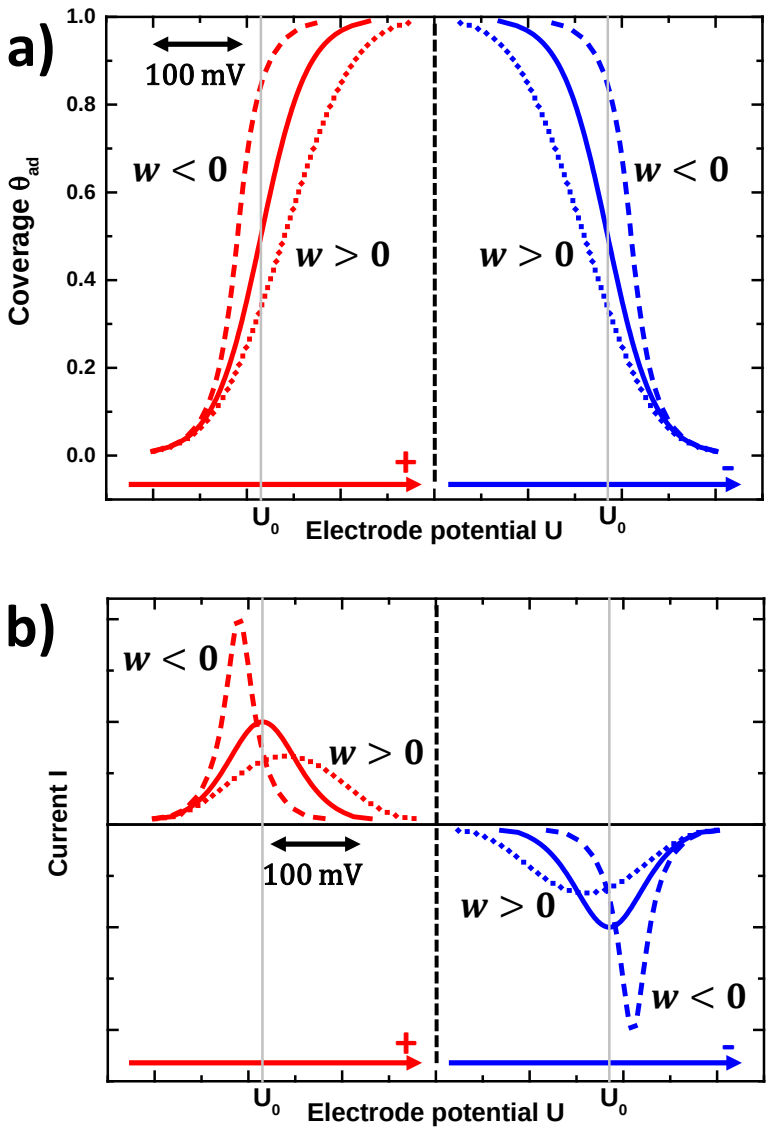

Figure 6.1: Langmuir isotherm (solid line) and two Frumkin isotherms ($w = -50$ meV dashed and $w = +50$ meV dotted lines) at room temperature ($n = 1$). a) depicts the coverage Θ and b) the derivative of Θ, which is proportional to the current, both as a function of the changing potential.

At this point, the contributions due to the presence of the solvent has not yet included. The energy required to desolvate the ion and to desorb water from the surface is kept unchanged and hence is included in ΔG_0. The entropy-related term changes if the number m of water molecules, which have to desorbed from the surface upon the adsorption of one ion, is different from one. The latter aspect is considered in the so called Flory-Huggins isotherm (statistics) [21]. Accordingly, eq 6.8 now reads:

$$0 = \Delta G_0 + eU + \frac{kT}{n} ln\left(\frac{\Theta}{(1-\Theta)^m}\right) + w\Theta. \tag{6.9}$$

Values $m > 1$ induce a broadening of the Frumkin isotherms while values $m < 1$ yield in a compression. The value of m for the adsorption of Cl^- ions on Cu(110) in electrolyte is unfortunately unknown. To provide an informative basis, STM experiments for water molecules adsorbed on Cu(110) in UHV environment [62] as well as with *ab-initio* calculations for the water absorption in equilibrium with water in gas phase [63] are considered. Accordingly, the water molecule concentration at the surface is about 0.5-0.7 times the number of the upper most Cu atoms per unit area. The lattice constant of the Cu(110) surface unit cell is 0.363×0.256 nm. The ionic diameter of Cl^- is 0.362 nm. As mentioned already the true configuration is unknown for the solid liquid. Therefore, we use in the following discussion value of m =1 and 0.6 as upper and lower boundaries.

J.O'M. Bockris, *et al.* [21] pointed out that Frumkin isotherms are probably not sufficient to represent the adsorption of ions. They describe two different interactions upon ion absorption. The first one is a lateral repulsive component due to coulomb interactions which for small coverages is proportional to $\Theta^{1/2}$. A second component is an attractive lateral dispersive interaction which is for small coverages proportional to Θ^3. However, the underlying model suppose a homogeneous distribution of the adsorbed ions at the surface which is, as we will discuss later, questionable in case of the Cl^- adsorption on Cu(110). Nevertheless, repulsive as well as attractive potentials are conceivable and deviations from the Frumkin-like isotherm are possible. The Langmuir isotherm, however, has a benchmark character. At room temperature, for instance, an electrochemical adsorption process will extend over 150 mV if we consider: (i) only one type of adsorption site, (ii) a non-dissociative desorption/adsorption process, (iii) a vanishing overall lateral interaction ($w = 0$), (iv) $m = 0.6$, and (v) a quasi static change of the electrode potential. As depicted in Figure 6.1, an overall repulsive lateral interaction results in a broadening of the process, while attractive interactions compress it. A similar effect is obtained for different values of m. Quantities bigger or smaller than one induce broadening or compression, respectively.

6.1.3 Relation to electric currents in CV

Several processes at the solid-liquid interface contribute to the measured currents over the applied electrode potential range in CV. For Cu(110) in hydrochloric acid the electrochemical window is limited at negative cathodic potentials by the hydrogen evolution reaction (HER) and at positive anodic potentials by the copper dissolution as Cu^{++}. In-between these potential ranges a number of Faradaic and non Faradaic processes including the adsorption of Cl^- ions take place. The total electrical current is approximated by three principal contributions:

$$I[U(t)] = \underbrace{C\frac{dU}{dt}\bigg|_{\Theta}}_{(1)} + \underbrace{n\Gamma_{I,max}A\frac{\delta\Theta}{\delta U}\frac{dU}{dt}\bigg|_{\Gamma_{free}}}_{(2)} + \underbrace{\frac{A}{R_{CT}}f(U(t)-U_{0'})\bigg|_{\Theta,\Gamma_e}}_{(3)}. \tag{6.10}$$

In eq 6.10, term (1) considers the charging of the interface due to the applied potential. The capacitance C is a constant only in the very simple Helmholtz double layer model, which implies that any charge excess on the metallic face and the counter-charge in the solution resides planar at the interface; otherwise, it is a function of the charge density σ and thus depend on the applied potential. In the latter case the constant C has to be replaced by $C + U(t)(\delta C/\delta U)$. In CV experiments the potential sweep is linear in time and dU/dt is constant. The related change in the electron excess $d\Gamma_e \propto C$, which could show up as a continuous background in RAS-transients, are small compared to the respective changes during the adsorption of ions [20, 7].

Term (3) in eq 6.10 represents a Faradaic (charge transfer) current due to a redox reaction of diluted ions. This term considers, for example, the HER or the dissolution of the electrode at the edge of our potential window. The measured current depends on the applied potential U, the surface area A and the charge transfer resistance R_{CT} (the exchange current density $J_0 \propto 1/R_{CT}$). In contrast to the hetero-epitaxial adsorption and desorption of ions, the HER and the copper dissolution as Cu^{++} remains in a non-equilibrium state within the experimental time frame. In the Butler-Volmer theory the function $f(U - U_{0'})$ is an exponential relation, where $U_{0'} = \Delta G_0/e$ is the standard equilibrium potential of the respective reaction. In the limit of small currents, the electrode surface does not change upon such reactions and the optical response remains constant. The copper dissolution in our particular case, appears in EC-STM as an step flow and the general appearance of the surface does not change. At higher dissolution currents, however, roughening sets in and causes clear changes in the RAS response.

Contribution (2) in eq 6.10 takes into account the adsorption and desorption of an ion (Cl^-). The measured current and thus the change of the electronic excess Γ_e, is proportional to the change of the surface coverage Θ. Note that the sum of all charges on both sides of the interface has to be zero. "The countercharge to the electronic charge can be divided into the charge stored in the diffuse double layer

and the charge stored in the adsorbate" (Schmickler and Santos [20]). The charge stored in the adsorbate is obviously proportional to the number of adsorbate ions $\Gamma_I = \Theta\Gamma_{I,max}$ (eq 6.1). The number of ions in the diffuse double layer we call Γ_{free}. In term (2) of eq (6.10), Γ_{free} is kept constant because the relative small capacitive currents were already considered in term (1).

We can conclude that the surface optical anisotropy measured by RAS changes in proportion to the surface coverage, whereas the current measured in CV contains the time derivative of the surface coverage. The time (potential) derivative of the RAS-transients should therefore selectively resemble all such peaks measured in CV which relates to adsorption and desorption processes changing the surface anisotropy. The measured amplitude depends on the type of absorption and the chosen photon energy (wavelength).

The potential evolution of the surface coverage and thus the RAS transient is finally determined by the respective isotherm (Figure 6.1b). The latter correlation is only correct for quasi static potential changes. Under such conditions the current maximum appears in anodic and cathodic scan direction at the same potential without overpotentials. In case of a vanishing lateral interaction ($w = 0$), the standard equilibrium potential is $U_0 = \Delta G_0/e$. In real experiments, however, currents can only be measured at finite scan speeds. In our particular case it turned out that the Cu(110) surface is additionally irreversibly harmed at very low scan speeds (<0.5 mV/s) after a few cycles, therefore we have chosen a scan speed of 1 mV/s for the experiments. The resulting overpotentials were determined by means of CV experiments with different sweep rates (not shown here). For 1 mV/s we found activation overpotentials smaller than 2 mV.

6.1.4 Results and Discussion

Figure 6.2 shows a sequence of CV's with a common scan rate of 10 mV/s for Cu(110) in a HCl solution (10 mM). The potential window spans a range from -90 to -516 mV limited by the copper disolution as Cu^{++} in the anodic and hydrogen evolution reaction (HER) in the cathodic direction. The full range CV depicted by the solid blue line confirms the typical line shape of Cu(110) [50, 7] with two quasi redox coupled peaks. Two oxidation peaks in anodic direction are labeled A and B/C. In reference 50 we have discussed in detail by means of EC-STM results the correlation of these peaks with changes in the structures. With the assumed Cl^- adsorption occurring at peak A, we observe the formation of stripes/grooves extending in the [001] surface direction (upper EC-STM inset in Figure 6.2). At more negative potentials from peak A, the surface appears adsorbate-free and we could resolve the 1×1 Cu(110) unit cell. At more positive potentials the surface undergoes a complete faceting (lower EC-STM inset in Figure 6.2). Possibly at the same time a $[CuCl_2]^-$ dissolution as well as the formation of a CuCl aggregate film sets in. It extends as a plateau-like current due to kinetic limitations in the mass transport through the aggregate film or of the $[CuCl_2]^-$ complex in the electrolyte [50, 64].

The two reduction peaks in cathodic direction are denoted with D and E/A', respectively. In this potential range the surface returns in the pristine state with wide terraces showing EC-STM again the 1×1 Cu(110) unit cell. As will be discussed further, these peaks are more complex in a sense that they do not reverse as ordinary redox couples peak A, B, and C.

In this work we have studied the surface properties by RAS and CV under quasi static potential changes (regarding the Cl^- adsorption) with a scan rate of 1 mV/s. Kinetic effects due to diffusion and activation barriers are thereby almost omitted for all surface modifications. As pointed out before, even lower sweep rates could damage the sample but peak positions do not change further. In this regard, extended anodic dissolution would cause surface roughening, and at cathodic potentials hydrogen may creep into the copper bulk inducing irreversible changes. For the single wavelength RAS-transients we have chosen a photon energy of 2.3 eV (539 nm). It was selected from spectral resolved RAS measurements at fixed potentials [50] where the real part of $\Delta r/r$ at 2.3 eV turned out to be very sensitive to the Cl^- adsorption.

Figure 6.3 shows a CV as a function of time/potential measured at 1 mV/s together with the parallel

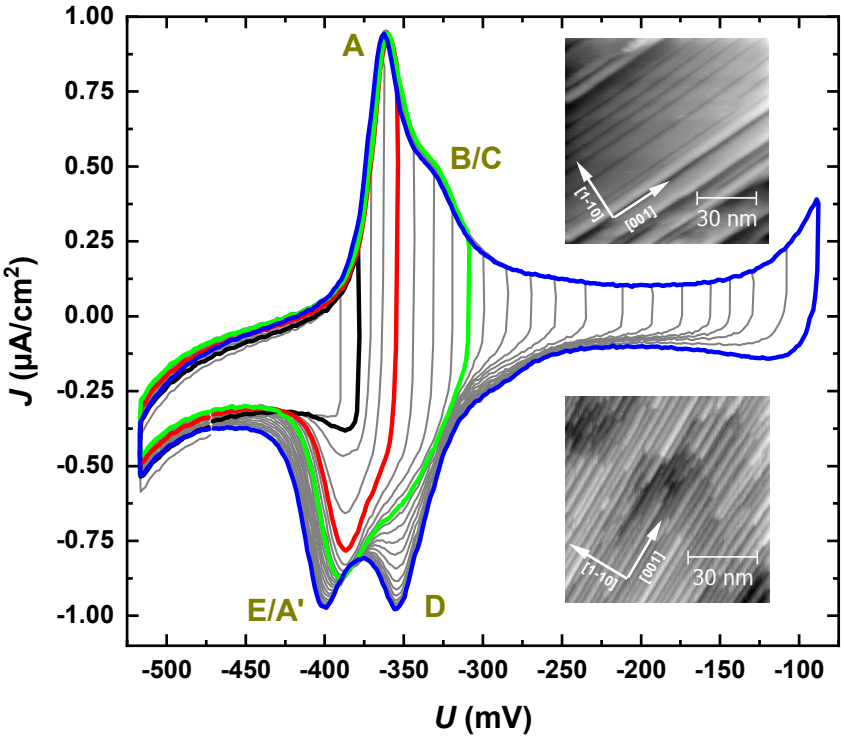

Figure 6.2: Sequence of cyclic voltammograms of Cu(110) in 10 mM HCl recorded at a the sweep rate of 10 mV/s. The potential is referenced vs. Ag/AgCl in 3 M NaCl. The upper EC-STM image shows the typical surface structure in the potential range of peak A, whereas the lower EC-STM image shows the faceted surface structure as it is found for potential more positive than peak B/C and D [50].

recorded real part of $\Delta r/r$. In the CV response shown in (Fig. 6.3a), the HER appears now with higher relative currents and peaks B and C seem to be quenched or redistributed. As shown by EC-STM experiments, the peaks B/C depend very much on the scan speed indicating different kinetic properties of the contributing processes [50]. The currents measured at potentials more anodic than peak A, include a diffusion limited dissolution of $[CuCl_2]^-$ [64]. The solubility of this cooper-cloride complex is low but still higher than that of the bare copper dissolution as Cu^+ ion and, at even more positive potentials above about -150mV, it vanished by the copper dissolution as Cu^{++}.

The currents measured in the first half of the subsequent cathodic scan (blue line) are interpreted as a superposition of the partial redeposition of copper (Cu^{++}) and the ongoing $[CuCl_2]^-$ dissolution and therefore the overall current remains positive. In the second half the diffusion limited redeposition of copper clearly overlaps with defacetting which was detected in connection with the two cathodic peaks D and E/A'. Basically, the CV resembles all the features known from higher scan rates. Note that are slightly shifted in potential due to the vanishing activation overpotentials.

The temporal RAS transient of the real part of $\Delta r/r$ at 2.3 eV (Figure 6.3b) nicely resembles the step wise change as expected for a Frumkin isotherm like adsorption/desorption (section 2); (Figure 6.1a). The RAS transient exhibits four sections in anodic as well as in cathodic direction. It is worth to mention that the kinetic behavior of the RAS signal remains basically unaltered also for measurements with faster scan speeds.

The first section from -450 up to -400mV in anodic direction corresponds to the HER with relatively strong Faradaic current. The RAS signal at 2.3 eV is not at all affected by this process. It is not shown here, but this independence is observed also at all other accessible photon energies between 1.5 and 5 eV (825-248 nm). Deviations, which emerge at 3.5 eV in this potential range, are clearly independent from the Faradaic current of the HER and are not further discussed here. Note that the capacitive charging of the interface due to the potential variation (term 1 in eq 6.10) is also not detectable - neither at potentials below -400 mV or at potentials higher than -300mV.

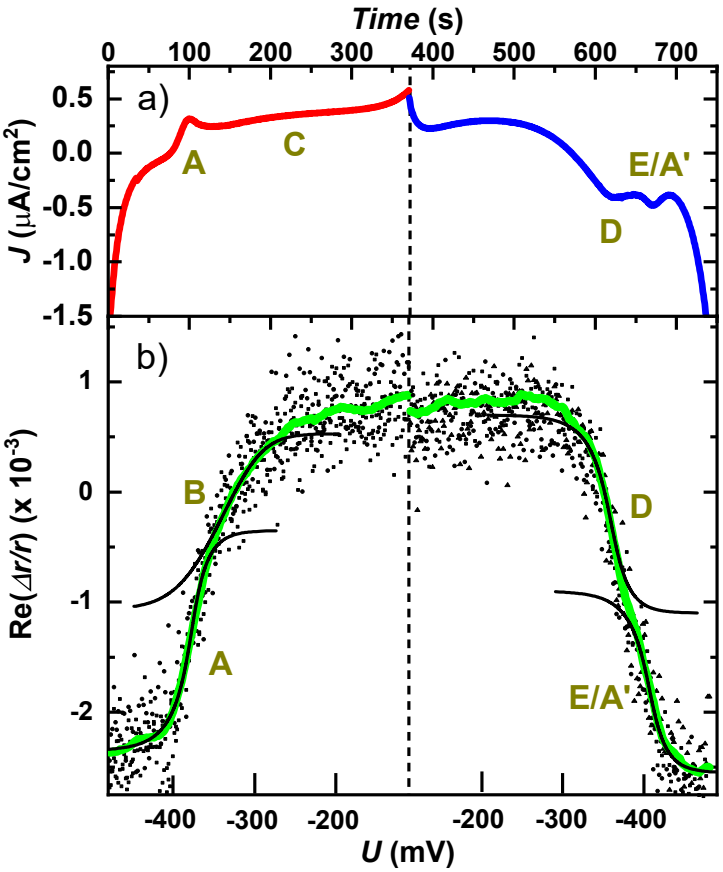

Figure 6.3: Comparison of the current (red and blue line in panel a) and the real part of $\Delta r/r$ measured in a RAS transient at 2.3 eV (black squares in panel b) over a CV loop with 1 mV/s. The green line in panel b was smoothed with a Savitzky-Golay smoothing algorithm in order to highlight the potential dependency of the RAS transient. The black lines in panel b are adapted as a guide to the eye, and represent the Frumkin isotherm line shapes based on the fitting shown in Figure 6.4. The potentials are referenced vs. Ag/AgCl in 3 M NaCl.

The second part in the anodic scan direction from -400 up to -350mV is characterized by a rapid change of the RAS signal from (-2.1 to -0.5) x 10^{-3}. This change of the optical anisotropy matches to peak A in CV and appears at potentials where the adsorption of Cl^- induce the formation of stripe like structures at the surface. The respective oxidation process completes in a remarkable narrow potential range of $\approx$ 50 mV. Considering the Frumkin isotherm-like line shape this would indicate a negative w-value.

The third part from -350 up to -270 mV differs from the previous one by a shallower slope of the RAS-transient. The real part of $\Delta r/r$ changes here from (-0.5 to 0.5)x 10^{-3}. The potential range matches with the formation of the surface facets. But in CV we can not recognize an oxidation peak at these potentials anymore. The faceting process recorded in RAS and the current maximum, which is now shifted to higher potentials, are thus denominated with two different labels B and C. At scan speeds of 10 mV/s they are merging together.

In the fourth part, from -270 up to -150 mV, the RAS response almost stabilizes at a value of 0.7 x 10^{-3}. In particular, we cannot recall any connection between the broad current maximum C and the remaining slope of the RAS transient. The $\Delta r/r$ signal changes only due to modifications in the surface properties; for instance, as induced by the adsorption of Cl^- ions. The current at maximum point C, which shows up only in CV (Figure 6.2 and Figure 6.3a), is attributed to the diffusion hindered copper dissolution of $[CuCl_2]^-$ while the surface properties do not change. The same argument applies for the copper dissolution as Cu^{++} at the positive end of the investigated potential range. The RAS signal does not change, although the current exponentially increases. The very small positive slope in the real part of $\Delta r/r$ above -300 mV continues in the following cathodic scan direction. We attribute this slope to a

marginal roughening or to an accumulation of the CuCl aggregate film at the surface.

The local minimum in the current, after changing the potential sweep direction due to the partially redeposition of copper as Cu^{++}, is again not changing the RAS signal. Thereafter follow two section where the RAS signal step wise changes back to negative values. The two changes in RAS are labeled with D and E/A'. The process D and E/A' reverses in a way the changes induced by B and A. The overall appearance resembles again a Frumkin isotherm like behavior. On the other hand, slopes, amplitudes and potential positions deviate from the line shape of B and A. The most obvious difference, however, is that both coincide now with respective negative peaks in the CV. The chemical pathway, which finally restores the smooth pristine Cu(110) surface, obviously differs significantly from the reaction steps in the anodic scan.

According to eq 6.10, the first derivative of the potential dependent RAS signal should equal the measured currents for all those reaction which change the electrode surface anisotropy. Figure 6.4 shows a respective comparison between the numerical derivative of the RAS transient *vs.* potential (green line) to the anodic (red) and cathodic (blue) currents. In this representation the strong correlation between the RAS response and the currents of peak A and the two reduction peaks D and E/A' becomes clear. Note that the process contributes with different proportionality factors; hence the relative amplitudes can not be correct. Nevertheless, the derivative of the RAS transient recalls precisely all sharp current peaks in CV. In case of the HER and the copper dissolution as (Cu^{+}/Cu^{++})/re-adsorption, the surface appears quasi static. These processes superimpose only the currents measured in CV but the derivative of the RAS signal is constantly zero. The latter fact again underlines that term (1) in eq 6.10 does also not contribute to the changes in the RAS signal either.

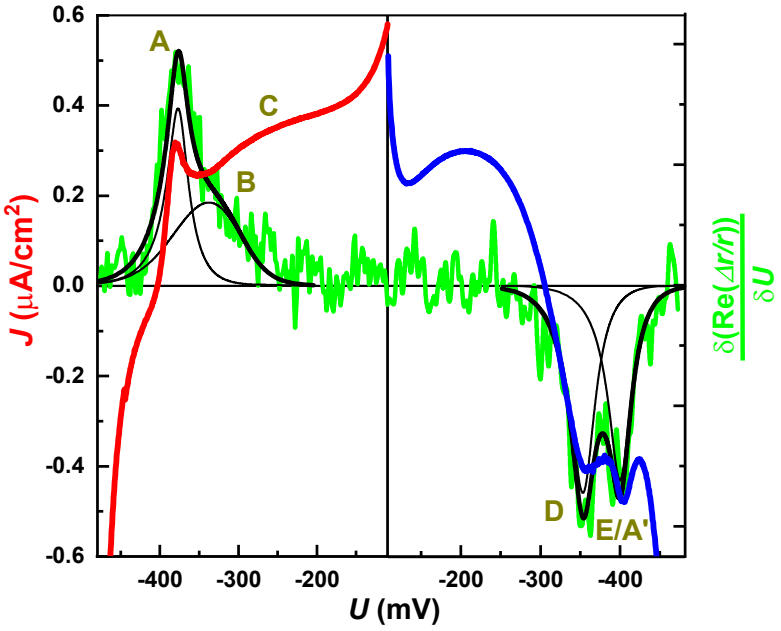

Figure 6.4: Derivative *vs.* potential of the real part of the RA transient measured at 2.3 eV (green line) and the CV-current (red and blue line) both measured parallel with a sweep rate of 1 mV/s. The black lines represent a numerical fit with Flory-Huggins isotherms. The potential is referenced *vs.* Ag/AgCl in 3 M NaCl.

In particular, it becomes clear in such comparison that the anodic B/C current peak, which is measured in CV's at higher sweep rates, has two components. The first part, denoted with B, corresponds to an adsorption induced faceting. The second part is related to the diffusion limited dissolution of *e.g.* $[CuCl_2]^{-}$.

The selective sensitivity of the RAS signal to surface modifications is used to analyze the underlining adsorption/desorption processes concerning their thermodynamic properties. Assuming Frumkin (Flory-Huggins) type isotherms we apply a parametric fit of eq 6.9 to the derivative of the RAS-transient.

Peak	w in meV	ΔG_0 in meV
A	-40 (-50)	-354
B	+25 (+15)	-349
D	-35 (-45)	-379
E/A'	-38 (-48)	-428

Table 6.1: Parameters w and $\Delta G_0 = U_0 e$ obtained by a numerical fit of the first derivative of the RAS transient (Figure 6.3 with Flory-Huggins isotherms ($n = 1$, $m = 0.6$ ($m = 1$)). The error of all values is estimated with ±5 mV. The potentials are referenced vs. Ag/AgCl in 3 M NaCl.

Therefore we numerically solved eq 6.9 for Θ and calculated the derivative according to the potential. By fitting the derivatives it is not necessary to consider absolute anisotropies and the individual processes separate. Each of the four peaks is fitted with a single Flory-Huggins isotherm and adapted with an individual proportionality factors. The Amplitude values have right now no physical significance and will not be discussed further. For all processes we have assumed $n = 1$ and $m = 0.6$ ($m = 1$). The obtained w and ΔG_0 values are summarized in table 6.1. The fit result with the four different contributions for $m = 0.6$ is shown in Figure 6.4 with black lines. For demonstration, the result is added by black lines also to Figure 6.3. Note, amplitudes and offsets of the different contributions are arbitrarily chosen in Figure 6.3.

For peak A we obtain with the fit a lateral attractive interaction of w_A =-40 meV (-50 meV) between the adsorbed Cl^- ions or thereby formed Cu-Cl^- complexes. The formation potential is $\Delta G_{0,A}$ =-354 meV. Note that the latter value do not coincide with the peak maximum. Just in case of a vanishing lateral interaction ($w = 0$) both the ΔG_0 and current maximum match. The integrated current of peak A discloses that the amount of adsorbed ions is less than a mono-layer [50] and EC-STM has shown that the starting point of the adsorption of Cl^- coincides with the formation of stripe like structures in the [001] surface direction. To form these structures, attractive forces along the rows are conceivable, regardless of their type.

The second surface oxidation step -peak B- appears much wider and overlaps strongly with process A. According to the EC-STM experiments [50], the faceting finishes right after peak A. Afterwards, the surface structure, as imaged by EC-STM, is left without changes. The isotropic dissolution may result in the movement of the facets but the integrative appearance probed by optics remains constant. A closer inspection of the EC-STM images near peak A, however, shows already the parallel evolution of surface stripes and facets. In the upper inset in Figure 6.2 one can already observe first facets while the stripe structures in the middle of the EC-STM image are not yet fully formed. A separation of both processes in quasi static experiments is thus only at reduced temperatures possible. The adsorbate which induce the faceting at process B is clearly of repulsive type (w_B =+25 meV). Obviously the lateral Coulomb repulsion is getting stronger as more negative ions are collecting at the surface. Together with attractive forces to the Cu substrate, the faceting becomes comprehensible.

The absence of a respective peak B in the CV could have several reasons. The facets could require a relatively small number of ions or a redistribution in terms of a phase transition. Furthermore conceivable is also an exchange of the adsorbed Cl^- ions by an oxygenated species as described in reference 65.

The fit results for the peaks D and E/A' underline again the mentioned differences compared to peak A and B. Neither the formation potentials nor the values for the lateral interaction w coincide as expected for redox pairs. Additional insights are obtained from Figure 6.2, which shows a sequence of cyclic voltammograms (10 mV/s) with different anodic turning points. From this sequential scan it becomes evident that oxidation peak A and reduction peak E/A' form at least a "quasi" redox pair. These two peaks depend on each other and the w value matches within the approximated error limits. But the potential of the maximum current depend on the time in which the copper electrode was in the "$[CuCl_2]^-$ " dissolution range before.

Peak D, on the other hand, emerge always at the same potential alongside to the defaceting, but its

amplitude is maximized just after the scan evolves to the constant current region. In another experiment, which is not shown here, both the potential positions and shape of the current peaks D and E/A' are the same, whether a 10 mV/s sweep up to -80 mV is made or by keeping potential constant at -250 mV for the respective time. D and E/A' current peaks on one hand and the defaceting and the disappearance of the surface stripes/grooves on the other hand both belong to the same processes if we keep in mind the perfect match of the current and the derivative of the RAS-transient. Furthermore the RAS signal reverses in a way the respective changes. But the chemical process behind seems to be different and involves the reduction of the before dissolved $[CuCl_2]^-$ or the CuCl aggregate film or other species.

6.2 Cloride induced surface states at the solid-liquid interface of Cu (110)

The identification of specific surface states (SS) on noble metals in ultrahigh vacuum (UHV) was first achieved with photoemission experiments and respective *ab-initio* calculations [66, 67]. In addition, the ability of some optical spectroscopies to exploit polarized light in place of electrons is giving researchers a new way of probing fundamental interactions of SS in non UHV conditions. In this regard, the subject of SS at the copper (110) surface was discussed in several previous publications. In particular, we mention here the pioneering work of E. E. Barritt, P. Weightman, *et al.* They have shown that reflection anisotropy spectroscopy (RAS) is a versatile optical probe to assess the formation of anisotropic surface properties of Cu (110) in electrolyte environments [1, 68]. However, the proposed interpretation of their experimental results poses some challenges. *In-situ* RAS is a complementary method applicable during sample preparation and complies the advantage that surface transformation can be monitored in a relatively easy way. Spectral features in RAS have been addressed as specific SS [69, 70, 18] in the framework of all these experiments and theoretical approaches. An unambiguous identification of related electronic properties interfaces is considerable more difficult in solid-liquid interfaces due to the limited applicability of electron-based techniques and also theoretical *ab-initio* approaches are demanding. In connection with our work on Cu (110), we should mention also the controversially discussed results for Au (110) in electrolyte [71, 72] as well as the early work of M. Kolb, *et al.,* on Ag(100) [73].

Results from *in-situ* electrochemical scanning tunneling microscopy (EC-STM) [74, 50, 53] and impedance spectroscopy measurements presented in the following, indicate that the Cu(110) surface in hydrochloride acid (HCl) show a complex behavior depending on the applied potentials. It is therefore necessary to clarify the current interpretation in the literature [1], [68]. Possible reasons for misinterpretations arise from the high sensitivity of the surface to oxygen [65] which will be considered in more detail in a subsequent publication. In Ref. [50] we have discussed by means of EC-STM the step wise transformation of the Cu(110) surface from the pristine state, showing the 1×1 upper most copper surface atoms as due to a chloride induced faceted surface with increasing anodic potentials. The latter facets were also observed upon Cl^- deposition in UHV [52]. At intermediate potentials, we have observed groove- or chain-like structures oriented along $[1\bar{1}0]$ [50]. Unfortunately, it was not possible to obtain atomic resolution of the chain structure. Wan and Itaya reported the same interface with EC-STM and they observed a Cu-Cl ad-row structure also parallel to $[1\bar{1}0]$ but with much smaller distance to each other [74]. Whether these findings share the same origin remains an open question, despite both structures are obviously induced by anion adsorption. As a matter of fact, quasi static experiments show that Cl adsorbs with an attractive lateral interaction, which is seemingly responsible for the chain-like structures[49].

In this work, impedance spectroscopy is used in order to obtain precise information about the potentials related to thermodynamically stable surface structures. Furthermore, based on the RAS results, we identify characteristic surface resonances at potentials of the previously measured self ordered surface stripes and grooves. A simple scheme based on a lateral surface quantum well is proposed to explain the observation of bands at specific intermediate potentials.

6.2.1 Experimental

Impedance Spectroscopy

Electrochemical impedance spectroscopy (EIS) is widely used in electrochemistry to study solid/liquid interfaces processes [75]. EIS determines, at a fixed electrode potential, the complex impedance Z as the ratio between a superimposed alternating electrode potential and the respective current, for different frequencies ω. Nyquist plots, where the imaginary part Im[Z] is plotted against the real part Re[Z] for all measured frequencies ω, allow for an intuitive analysis of the interface properties. The resulting curves start at high frequencies typically with a real value; namely, that of the ohmic resistance of the electrolyte R_{SOL}. Straight downward pointing curves arise due to the capacitive properties of the surface double layer. An upward bending occurs, roughly speaking, due to a charge transfer upon the solid/liquid interface and thus indicate and electrochemical reaction [75]. More specific information about the interface processes are retrieved by a numerical fit of the impedance at each potential with an equivalent electrical circuit model (ECM). We have used for this purpose the "EIS Spectrum Analyser" software [76].

The impedance was measured at Cu electrode potentials between -550 mV and -100 mV *vs.* Ag/AgCl in 3 M/L NaCl. The boundaries of the process are at the cathodic side, the onset of the hydrogen evolution reaction (HER) and at the anodic side, the Cu^{++} dissolution [49]. The frequency range was selected on the basis of the observed relaxation times between 1 Hz and 10 kHz. The amplitude of the applied alternating potential was 10 mV, small enough so as to avoid contributions of higher harmonics [75].

Reflection Anisotropy Spectroscopy

A home made RAS setup was used for the *in-situ* optical analysis based on the design by Aspnes, *et al.* [26]. RAS measures, at near normal incidence, the optical anisotropies which are given by means of the normalized difference of complex reflectivities between two orthogonal in-plane directions, r_x and r_y, as:

$$\frac{\Delta r}{r} = 2\frac{r_x - r_y}{r_x + r_y}. \tag{6.11}$$

The sample is orientated with x and y corresponding to the $[1\bar{1}0]$ and [001] crystallographic axis, respectively. The measured anisotropy is an average over the area of the light spot of about 4 mm in diameter. The electrolyte is optically isotropic and the back reflection from the air-water interface is avoided by a small tilting angle between the investigated copper electrode and the horizontal electrolyte surface.

6.2.2 Results and Discussion

Fig. 6.5 shows the 3D diagram of Nyquist plots recorded step wise at different potentials starting from -550 mV to -100 mV. Three main areas can be distinguished and are highlighted with orange, green and blue colors. The potential range with orange lines resembles the condition with vanishing electrochemical reactions. At very low potentials the onset of the hydrogen evolution reaction (HER) shows up by an upward bending of the impedance trajectory. The prominent behavior at -390 mV, marked with a thick red line, corresponds to the formation of grooves or stripes whose appearance has been attributed to the adsorption of Cl^- [50, 49]. For slightly higher potentials, at -350 mV, we find another peculiarity highlighted by another thick red line. It is around this potential that EC-STM measurements have shown a faceting of the surface [50]. In reference [49] these two processes have been denoted as "A" and "B", and both are superimposed with the onset of the so called "constant current" region associated to Cu^+ dissolution [49]. The respective area is marked by olive lines in Fig. 6.5. Previous EC-STM and RAS experiments suggest that the appearance of the Cu (110) surface does not further change upon this dissolution process. The Cu^{++} dissolution/redeposition dominates the measured impedance at the most

anodic potentials (blue lines in Fig. 6.5).

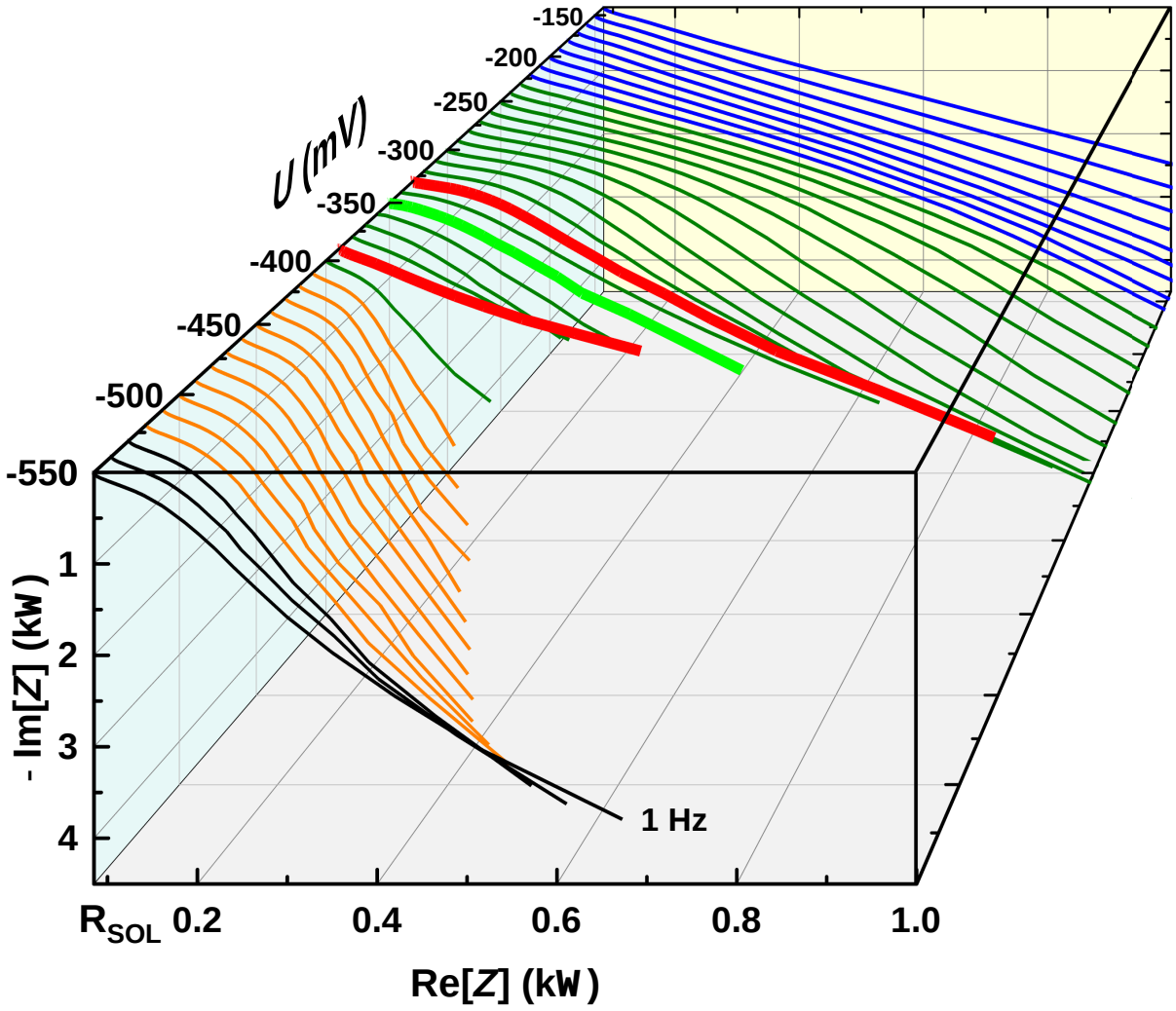

Figure 6.5: Nyquist plots of the impedance measured across the Cu (110) surface in a 10 mM/L HCl solution at electrode potentials between -550 and -100 mV and in a frequency range from 1 Hz to 10 kHz. The first part (black lines) is due to a hydrogen evolution reaction (HER). The orange lines comprise a potential window of vanishing surface reaction, for which EC-STM has shown a pristine adsorbate-free surface structure. The red lines highlight potentials with distinct surface reactions whereas the olive and blue lines emphasize potentials where dissolution processes of *e.g.* Cu^{+} and Cu^{++} take place. The electrode potentials are referenced *vs.* a common Ag/AgCl in 3 M/L NaCl.

The impedance behavior at each offset potential was analyzed with the equivalent electrical circuit model (ECM) as shown in the inset of Fig. 6.6. Three different interface contributions are grouped in a parallel circuit in addition to the resistivity of the solution R_{SOL}. The capacity C_{DL} of the double layer is considered by an ordinary capacitive element with an impedance $Z_{DL}(\omega) = 1/(C_{DL}(\mathrm{i}\omega))$. At finite temperatures, this C_{DL} depends on the applied potential regardless possible surface modifications. Faradaic currents arising from the HER or the dissolution of copper, can be approximated by an ohmic resistor. We consider such currents with a "Warburg" impedance $Z_W(\omega) = 1/(C_W(\mathrm{i}\omega)^{0.5})$ in order to address time dependencies due to diffusion limited processes [75]. The latter mainly contribute at lower frequencies. More advanced "Warburg" elements deal with finite diffusion layers or geometry effects. Such comprehensive models are omitted here since both the HER and the copper dissolution are not in the focus of this work, as we are interested in interface changes arising from adsorption/desorption processes.

The respective impedance response is modeled with a series connection comprised by an ohmic charge transfer resistivity R_{CT} and a constant phase element (CPE). The CPE can be interpreted as a non ideal

capacitor as:

$$Z_{CPE}(\omega) = \frac{1}{C_{CPE}(\mathrm{i}\omega)^{\alpha}}, \tag{6.12}$$

which behaves like an ordinary capacitor when $\alpha = 1$. For values $1 < \alpha < 0.5$ the CPE is regarded as a capacitor with losses. Empirical studies with single crystal metal electrodes have attested that the CPE-behavior of the electrochemical interface results from mono layer adsorption/desorption process [77, 78, 79], while a chaotic behavior due to surface roughening on a larger length scale would occur, in contrary to previous reports in the literature, at lower frequencies.

In this work we use the α value as an independent benchmark parameter to identify surface modifications and in turn to discover thermodynamically stable configurations. The α values are obtained by a numerical fit for each potential which resort on six independent parameters. These are: (1) the constant resistivity of the solution $R_{SOL} = 85\ \Omega$ fitted at -450 mV, (2) the charge transfer resistivity R_{CT}, (3) the CPE capacitance Z_{CPE}, (4) the α value, (5) the double layer capacitance C_{DL}, which appears to be small in comparison to the CPE capacitance, and (6) the Warburg element capacity Z_W.

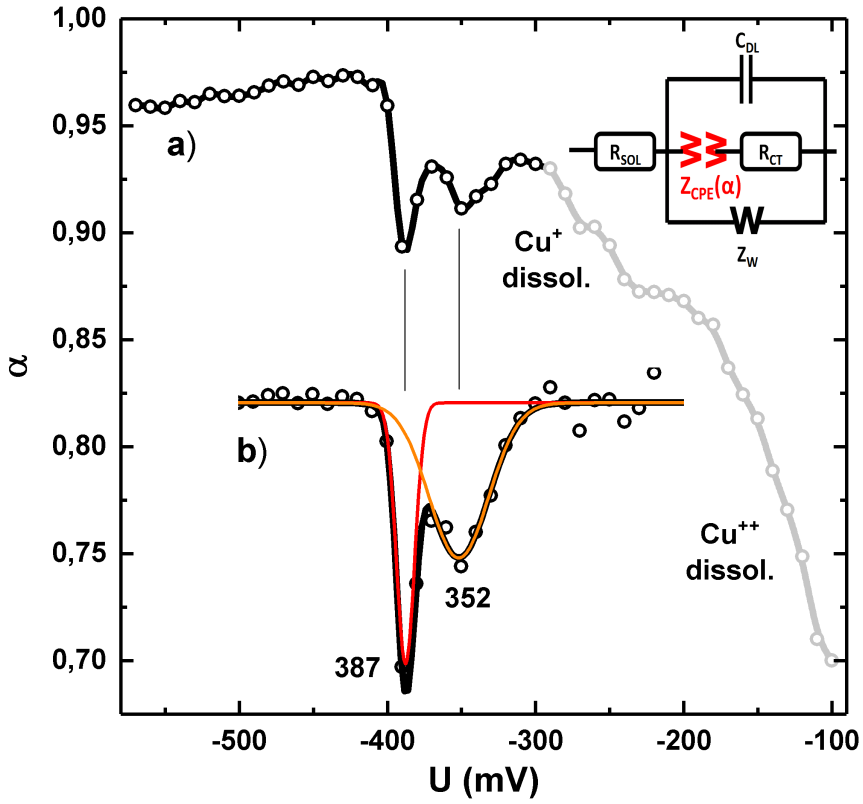

Figure 6.6: a) constant phase element α (empty circles) vs. applied potential U indicating surface modification when deviating from $\alpha = 1$. The solid black line is a numerical fit to the impedance measured across the Cu (110) surface in a 10 mM/L HCl solution (Fig. 6.5), employing an equivalent electrical circuit model (inset). The dissolution processes region is an artificial decrease (gray line). b) Gaussian fits (red and orange lines) after subtraction of the continuous background. Experimental points were vertically downshifted for the sake of clarity. The electrode potential is referenced *vs.* a common Ag/AgCl wire in 3 M/L NaCl. See text for details.

The obtained α values are plotted in Fig. 6.6 as a function of the electrode potential. Between -550 and -390 mV the α values are greater than 0.96. In agreement with our EC-STM results the pristine

surface remains unchanged at these potentials. The two peculiarities, which are marked in the Nyquist plots in Fig. 6.5 by red lines, appear as two distinct downward pointing peaks in α. At potentials higher than -300 mV the α-value starts decreasing due to the dissolution of Cu most likely in form of Cu^{+}-Cl complexes. The Cu^{+}-dissolution is a strongly diffusion limited process and the formation of a CuCl aggregate layer is reported. In cyclic voltametry experiments a peak "C", which is strongly dependent on the scan speed [64, 50, 49]. At even higher potentials the α-value further decrease because of the Cu^{++}-dissolution. It is important to note that ECM is not sufficient to reproduce the diffusion limited dissolution in a correct manner. The continuous decrease of the α value is thus an artifact. However, the overall dependency illustrates that the dissolution process overlaps with surface oxidation features.

The potential behavior of the two surface oxidation features are, therefore, determined with a Gauss peak fit after subtracting the "background" of the dissolution processes (Fig. 6.6 b). Accordingly, the minima of α are determined at -387 and -352 mV *vs.* Ag/AgCl/3M NaCl. These are the potentials corresponding to the highest formation rates of the two oxidation steps which correlate to the constitution of surface grooves/stripes and facets, respectively. The width of both peaks appears substantially different. In reference [49], we have addressed these effects as originated by lateral attractive (at 387 mV) and repulsive (at -352 mV) interaction of the Cl^{-} adsorbate. The negative peaks in α, however, do not match the therein discussed Frumkin-Isotherm line-shapes and therefore we use here a Gauss line shape. Note that the peak potential values are those of the highest formation rates. They are not identical with the $\Delta G_0/e$-values determined in reference [49] because ΔG_0 is the formation energy of the adsorption of an isolated ion. Most important is the overlap of the two processes; *i.e.*, due to the different width of the formation window at room temperatures, both oxidation processes "start" at around -400 mV but the potential of the highest formation rates appear separated.

Fig. 6.7 shows the development of the real part of the RAS spectra for selected potentials between -411 and -170 mV. All spectra were measured at fixed potentials and thus show the respective thermodynamic equilibrium properties of the surface. Starting from the most negative potential the first changes are observed above -380 mV.

The RAS spectra at potentials higher than 380 mV show small but reproducible new resonances marked with (*) in Fig. 6.7, between 2.2 and 2.6 eV. At these potentials we observed also the very characteristic surface stripes along the [001] direction (upper inset in Fig. 6.7 and Fig. 4a in reference [50]). In reference [50] we have interpreted this self organized structure as "grooves" stabilized by a Cl^{-} adsorption. However, in view of our later experiments we use this interpretation with care. Also conceivable is a Cu-Cl ad-row structure; however atomically resolved EC-STM images are still missing and a precise structure analysis is thus difficult. Worth mentioning in this connection is the reported weak bound strength of the Cl-ions [80, 81]. Andryushechkin, *et al.* [52] have discussed a complete loss of atomic resolution in STM while studying sub-monolayer Cl coverages on Cu(110) in UHV.

In the following we will first consider the general line shape changes in the RAS spectra in more detail in order to highlight the supposed surface state origin of the additional resonances. The pristine Cu shows a step like line shape (orange line in Fig. 6.7) at around 2.1 eV. The latter changes gradually to a prominent relatively broad peak with local maximum at 2.25 eV. This change takes place in the potential range of the second oxidation feature which was discussed already in EIS measurements (Fig. 6.6) and was attributed to the faceting of the surface. Accordingly, the RAS line shape also starts changing already at about 400 mV and before we could observe the surface resonances. Indeed, one can see the parallel evolution of the facets also in the EC-STM image (lower right hand corner in the upper EC-STM image in Fig. 6.7). As pointed out above, the potential range of formation is due to repulsive lateral forces [49]. The "stripe phase" with the proposed new electronic surface resonances is therefore only in a very small potential range observable. As shown by the EIS measurements, we obtain the strongest amplitude of the surface resonances after completion of the groove/stripe phase, but before the facets cover the entire surface, at about -350 mV.

The RAS spectra of the faceted surface compare very well with the spectra measured by Martin, *et*

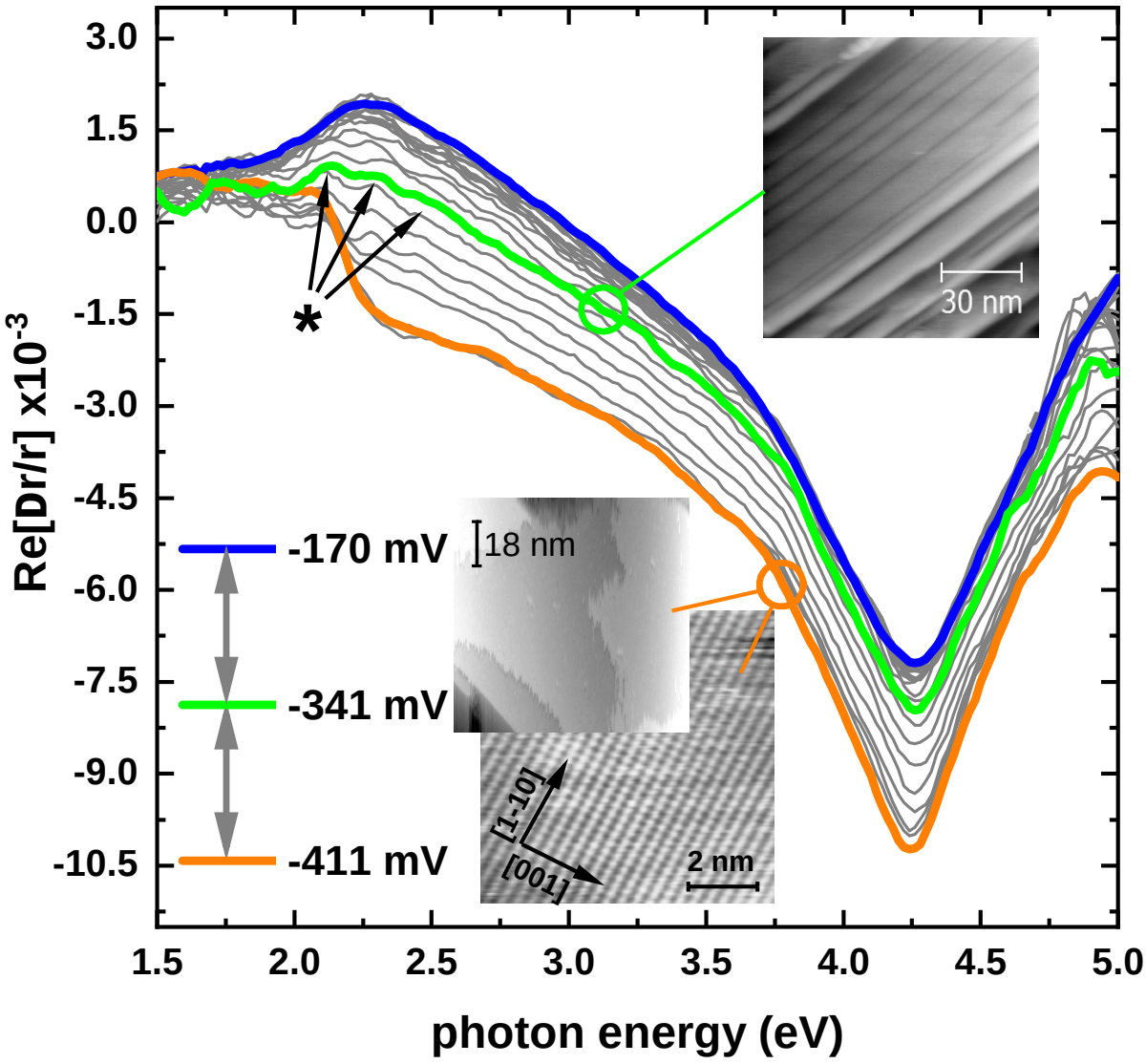

Figure 6.7: Real part of $(r_{[1\bar{1}0]} - r_{[001]})/r$ of Cu(110) at different electrochemical potentials between -411 and -170 mV *vs.* Ag/AgCl/3M NaCl. The orange, green, and blue lines correspond to three characteristic surface configurations which are discussed in detail and were characterized by EC-STM (insets)[50]. The spectra were averaged with a Savitzky−Golay filter considering 5 neighboring points.

al. [82] on Cu (110) surfaces in UHV after thermal annealing. The thermally annealed surfaces show a high density of monoatomic steps which also arrange along the [001] surface direction. As we will discuss below in more detail, we believe that the respective RAS spectra are a result of the surface morphology. The (monoatomic) steps along [001] are likely stabilized by oxidizing species. In our case by Cl^- or in other environments by O^-, S^{2-}, or HSO_4^-, *etc.*

In our electrochemical experiments, we have observed with EC-STM the 1×1 signature of the pristine copper at ≈-400 mV (inset Fig. 6.7 and reference [50]). The respective RAS spectra, like the orange line in Fig. 6.7, should correspond to a "clean" surface. The RAS spectra, nevertheless, do not agree with those obtained at the pristine Cu(110) surface in UHV. In particular, the known surface resonance at 2.1 eV [83, 69] is completely absent. We would explain this difference with the fact that the copper electrode is kept at a negative potential to obtain a pristine surface in HCl. In the literature we found different results about the potential of zero (total) charge (PZC) [84, 85, 86]. However, in agreement with our own results on Cu(111) all of them predict the PZC at more positive potentials. The surface dipole is thus reversed in comparison to pristine metal surfaces in UHV where the electron spill-out leads to the formation of the surface states with the characteristic surface resonance at 2.1 eV. The latter assumption is supported by the close agreement of our RAS spectra measured below ≈-400 mV with those measured

in UHV after deposition of 0.5 mono layers of sodium on Cu (110) [87]. The electronegativity of sodium is even smaller than that of the copper.

As a matter of fact, the Cu(110) is intrinsically anisotropic due to the reduced symmetry of the respective surface unit cell. In general we distinguish two different contributions to a RAS signal. The one which is responsible for the RAS spectra of the pristine surface measured here in HCl, refers to *surface modified bulk resonances* [88, 89, 69]. The second contribution, as observed at more positive potentials after the first Cl^- adsorption, is caused by resonances which involve new electronic states at the surface. Note that both the bulk of the Cu-electrode and the electrolyte are optically isotropic.

The interface optical response can be approximated with a so called "3-phase model". In such model the interface is represented by an anisotropic interface layer of thickness d in-between the half infinite substrate (our cubic single crystal $Cu_{(bulk)}$) and the half infinite ambient (in our case the electrolyte). The substrate and ambient dielectric functions (DF) are ε_s and ε_a. The latter is a real number since the ambient is transparent ($\varepsilon_a = n_a^2$). By means of a thin film approximation $d \ll \lambda$ ($d \lesssim 1$ nm) one can retrieve the measured $\Delta r/r$ as a function of the so called surface dielectric anisotropy (SDA) $\Delta(\varepsilon d) = (\varepsilon_{o,x} - \varepsilon_{o,y})d$ [56, 57]:

$$\frac{\Delta r}{r} = 2\frac{r_x - r_y}{r_x + r_y} = -\mathrm{i}\frac{4\pi\sqrt{\varepsilon_a}}{\lambda(\varepsilon_s - \varepsilon_a)}(\varepsilon_{o,x} - \varepsilon_{o,y})d. \tag{6.13}$$

Eq. 6.13 includes the ambient DF ε_a which is usually taken as $\varepsilon_a = 1$. Due to the low concentration of HCl we use the DF of pure water (ε_a=ε_{H_20}) [58]. The larger refractive index of the surrounding compared to air or vacuum increase the measured reflection anisotropy values a little. The substrate DF was determined by spectroscopic ellipsometry in HCl with a Cu(111) sample at electrochemical potentials where no surface adsorbates are present on the surface. Charges in the surface double layer were modeled in a separate surface layer and the DF so obtained is that of the bulk copper [7].

The measured $\Delta r/r$ is proportional to the anisotropy in the surface but the spectral line-shape is a convolution of the substrate DF and the SDA. Therefore, it is instructive to relate the SDA from the RAS response according to:

$$\Delta(\varepsilon d) = \mathrm{i}\frac{\lambda}{4\pi\sqrt{\varepsilon_a}}(\varepsilon_s - \varepsilon_a)\frac{\Delta r}{r}, \tag{6.14}$$

which represents the surface properties.

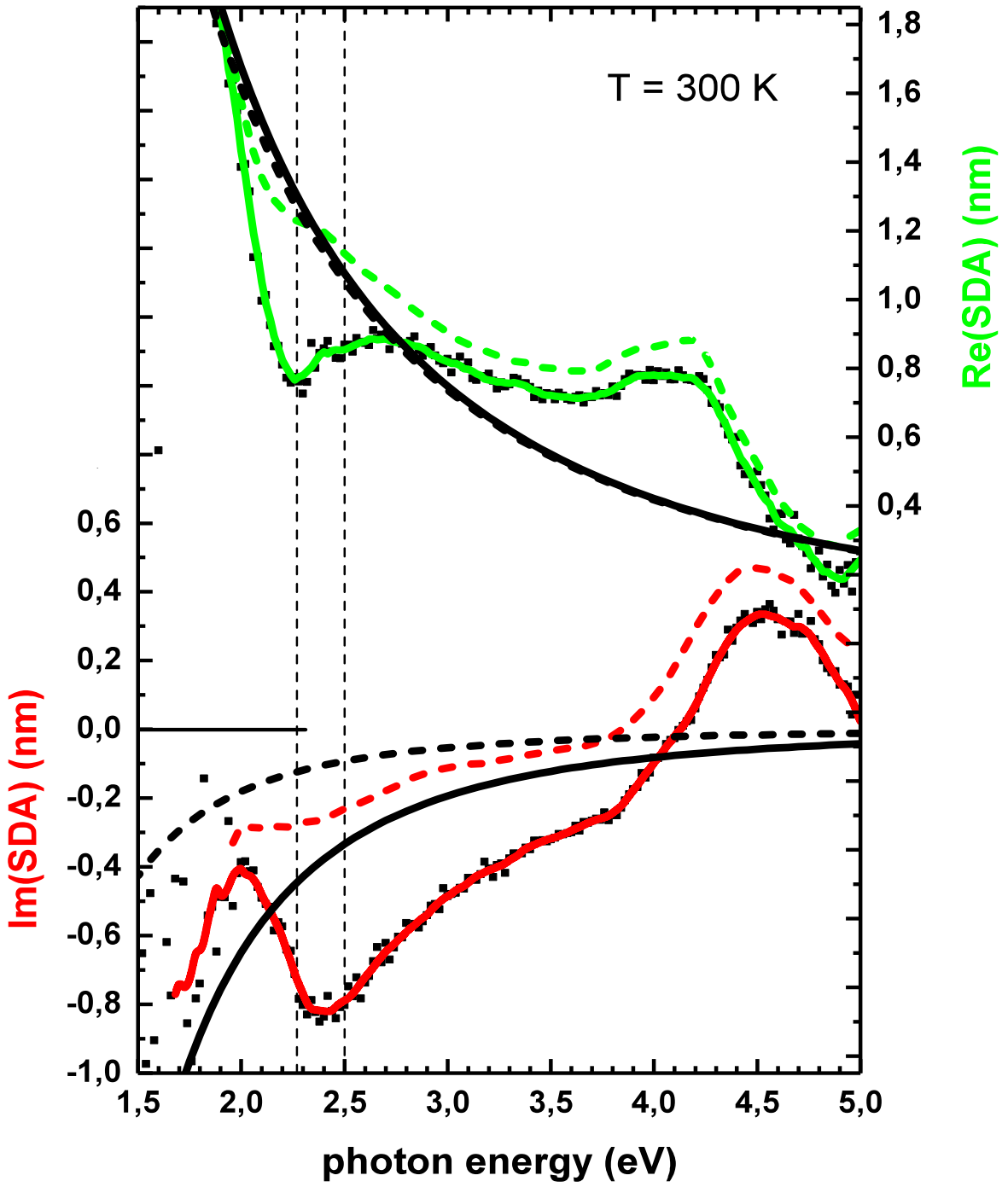

Figure 6.8: Real and imaginary parts of the surface dielectric anisotropy (SDA) of Cu(110) in HCl at -341 mV *vs.* Ag/AgCl/3M NaCl (black squares); the red/green solid lines are guides to the eye. The two vertical lines indicate the energy region of electronic resonances on the surface. The green and red dashed lines represent the SDA of the pristine surface at -411 mV. The dashed and solid black lines are the Drude-like response for clean and modified by HCl surfaces respectively.

Fig. 6.8 shows the SDA of Cu(110) at -341 mV, *i.e.* after the first oxidation (red and green solid lines) in comparison to the respective SDA of the pristine surface (red and green dashed lines). In both cases, the overall line shapes of the SDA are those of an anisotropic Drude-like response of free electrons which is of $1/\omega^2$-type. It is superimposed by surface modified bulk resonances and additionally by the aforementioned surface resonances in the spectra measured at -341 mV. Note that real and imaginary parts of these SDA, have positive and negative values, respectively. This behavior is caused by the natural corrugation of the pristine Cu(110) surface with grooves along the $[1\bar{1}0]$ direction. The SDA shows, therefore, a superimposed Drude-like line-shape as expected if the effective electron mass along the [001] is larger than in $[1\bar{1}0]$ direction. According to this model, the absolute values of the imaginary part of the SDA are smaller than that of the real part for the pristine surface.

The formation of well separated surface rows in [001] direction upon the first Cl^- adsorption increases the scattering of surface electrons in $[1\bar{1}0]$ direction. Within the Drude model, this yields a decrease electron mobility (shorter scattering time) along $[1\bar{1}0]$. The result is a decrease of the imaginary part of the Drude-DF in $[1\bar{1}0]$ direction while the real part remains the same as observed in Fig. 6.8.

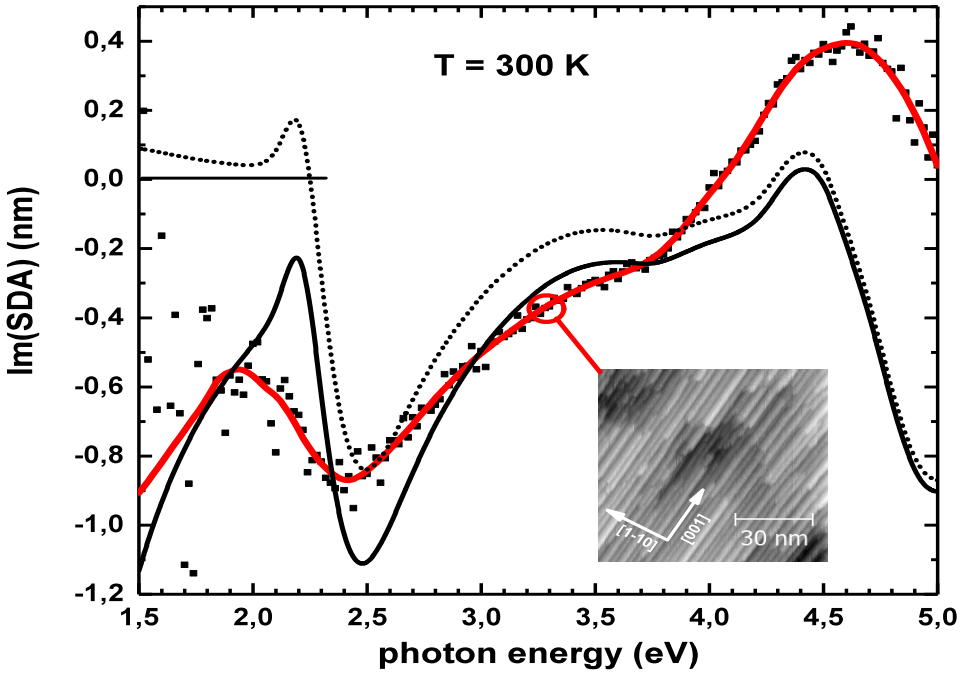

Figure 6.9: Surface dielectric anisotropy (SDA) of Cu(110) in hydrochloric acids after the Cl^- induced faceting (black squares and red solid line is a guide to the eye). The spectrum was recorded at -170 mV *vs.* Ag/AgCl/3M NaCl. The black line is a SDA calculated in an effective medium approach (Eq. 6.15) considering the bulk Cu DF admixed with the surrounding electrolyte for different screening/depolarization parameters along the [001] and $[1\bar{1}0]$ directions[7]. The dashed line reproduces the imaginary part of the surface dielectric anisotropy (SDA) of the pristine surface for comparison (-411mV).

The faceting of the surface upon the second oxidation/adsorption stage induces a SDA line-shape of the SDA which contains only bulk resonances. This connection can be illustrated within an anisotropic effective medium approximation, which accounts for the surface grooves along [001] direction. In the long wavelength limit, an effective macroscopic DF $\langle\varepsilon\rangle$ of a homogeneous medium is regarded as a "mixture" of the two material properties. In our case these are the DF of bulk copper and the surrounding electrolyte

(water). For the interface effective DF, one can use a Maxwell-Garnett type mixture:

$$\frac{\langle\varepsilon\rangle - \varepsilon_{H_2O}}{\langle\varepsilon\rangle + p\ \varepsilon_{H_2O}} = f\frac{\varepsilon_{Cu} - \varepsilon_{H_2O}}{\varepsilon_{Cu} + p\ \varepsilon_{H_2O}}, \tag{6.15}$$

where $f = 0.5$ denotes the volume fraction of the two compounds and p the depolarization factor. For electric fields parallel to the grooves the DF becomes a linear mixture with $p \to \infty$ due to the absence of boundaries. For electric fields perpendicular to the grooves, interface charges induce a screening and the effective dielectric functions is mixed in a reciprocal way ($p \to 0$). The SDA of the faceted surface can be approximated by:

$$\Delta(\varepsilon d) = (\langle\varepsilon_{p\to\infty}\rangle - \langle\varepsilon_{p\to 0}\rangle)d \mathrel{\widehat{=}} (\varepsilon_{[1\bar{1}0]} - \varepsilon_{[001]})d, \tag{6.16}$$

where the thickness d is arbitrarily chosen so as to match amplitudes.

Fig. 6.9 shows a comparison of the calculated and the experimental SDA of the faceted surface. The effective medium model resembles all the features of the measured line-shape although the amplitude and broadening do not match. Note that our model neglects the perturbation of Cu bulk resonances near the surface *e.g.* due to a shift of the d-band or strain [90]. Also changes in the free electron mobility and effective masses are not yet included. As mentioned already, the latter effect is responsible for the $-1/\omega^2$ background. For comparison we include also the imaginary part of the SDA of the pristine surface. It features some parts of this background line-shape due to the anisotropy in the effective mass of the surface electrons. However, the pristine as well as the faceted surface show only surface modified bulk resonances. In particular, the prominent feature, which evolves in the $\Delta r/r$-RAS spectra (Fig. 6.7) from a step like function at about 2.1 eV to a broad positive peak at 2.25 eV, clearly belongs to the surface modified bulk resonances and it is connected to well known bulk d-band resonances [91].

Interestingly, at least another three resonances clearly show up at electrode potentials between -390 and -380 mV and surely arise in addition to both the Drude like response and the signatures of surface modified bulk resonances. Indeed they appear mainly above the potential of the highest formation rate of the first oxidation as measured by EIS. With the faceting of the surface upon the second oxidation/adsorption stage these surface electronic resonances disappear again. Fig. 6.10a illustrates the potential evolution in a close up of the slightly smoothed $\frac{\Delta r}{r}$. The raw data points are exemplary shown as black squares for two spectra. The first peak "a" appears at 2.1 eV and thus at the same photon energy as the known surface state transition at the pristine Cu (110) in UHV [69, 92]. The latter has been attributed to a transition between Shockley-type surface states at the $\bar{Y}$ point of the surface Brillouin zone [69, 18].

Because of the close correlation regarding the line shape (upward peak in $\Delta r/r$) and the peak position at 2.1 eV, we argue that peak "I" share the same origin. Accordingly, we would proposed for the observed surface resonances a model where the $\bar{Y}$ surface states are confined between the groves or add-rows. The next two additional peaks "II" and "III" occur at higher photon energies with a spacing of about 0.15 and 0.2 eV, respectively. The groves or add-rows show in our EC-STM images a regular spacing and keep a distance of $\approx$ 4.6 nm. Only a few of them show up with a minimum distance of $\approx$2.6 nm. (Fig. 6.10c). The second type appears at slightly higher potentials or after later in time and thus seem to be energetically less favored. Within a simple quantum mechanical model for two-dimensional confined surface states [61] one can approximate the expected energy spacing E_n with:

$$E_n(k) = \frac{\hbar^2}{2m^*}\left(k_{||}^2 + \frac{\pi^2 n^2}{L_\perp^2}\right), \tag{6.17}$$

where m^* is the effective electrons mass of the respective surface band, $L_\perp$ is the distance (in-plane confinement) between the groves or add-rows, and $k_{||}$ is the wave vector parallel to the rows in [001] direction. The effective electron mass of the $\bar{Y}$ surface state just below the Fermi level was determined by angular resolved photo emission to $m^* = 0.43m_e$ [93]. By taking $L_\perp = 4.6$ nm and $k_{||}$=0 we obtain an energy spacing of, $\Delta E_{1,2}$ =0.12 eV and $\Delta E_{2,3}$ =0.21 eV, respectively. The "ground" state energy E_1 should increases by $\approx$0.04 eV with respect to the unconfined surface state. The measured surface resonances fit surprisingly well to this simple model. With more realistic continuously changing potential barriers of a finite height the new surface states will shift in energy and arrange in a more regular spacing

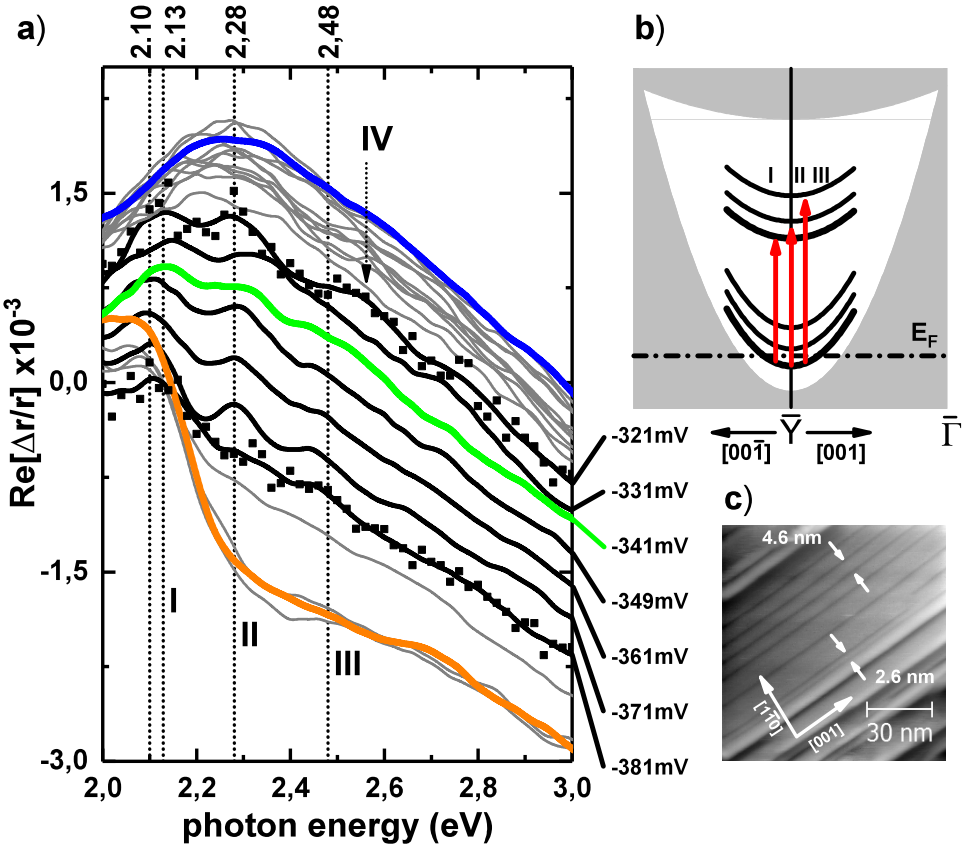

Figure 6.10: a) RAS spectra of Cu (110) in HCl recorded at different applied potentials as indicated. Within -390 to -380 mV, three clear resonances appear, labeled as I, II and III. These transitions are proposed to occur in the band scheme located near point $\overline{Y}$ of the surface Brillione Zone shown in b), from below Fermi level to confined states of the lateral surface quantum wells. c) EC-STM image measured at -341 mV. See text for details.

compared to the $1/n^2$ distribution for a particle in an infinite box. In addition, one has to consider at least partially hybridization of the surface states with the electronic orbitals of the adsorbed anions. Asymmetries in the peak shape and additional humps like the "IV" feature (Fig. 6.10a) show up in particular at higher potentials and may are related to the confinement in-between rows with the ≈2.6 nm spacing. According to Eq. 6.17, then we could expect confinement energies of E_1 =0.13 eV, E_2 =0.51 eV, and E_3 =1.16 eV. The noticeable shift of peak I) from about 2.10 eV at potentials between -380 and -350 mV, to about 2.13 eV at potentials between -350 and -320 mV, could be addressed in our model to the increasing number of rows with spacing of 4.6 nm.

Without photoemission experiments or additional atomically resolved EC-STM images plus band structure calculations for the respective structure models, we can just speculate about the strength of the hybridization effect. As mentioned already, the peak at 2.1 eV measured at the pristine Cu (110) surface in vacuum, was identified to be a transition between surface states at $\overline{Y}$ with an occupied surface state about 0.3 or 0.4 eV below the Fermi level and an unoccupied surface state about 1.7 eV above [69, 18]. If we just speculate, that the hybridization effect is small, the additional bands due to confinement should emerge at higher energies relative to the unperturbed states. In such a scenario, the observed resonances could originate from transitions as illustrated in Fig. 6.10b. However, there could also be other scenarios if we consider, for example, the existence of Cu-Cl-hybrid-states. As in the case for the Cu(110)-(2×2)O [18, 94], surface transitions among them would split in several resonances due to a confinement between or in the rows. But the strong similarity between peak "I" in our experiments and the 2.1 eV surface transition at the pristine Cu(110) surface must be assumed to be accidental.

Finally, we would like to note that a possible splitting or shift of electronic transitions due to the applied electric fields is not sufficient to explaining the observed resonances. The spectral changes evolve within an electrode potential range from -390 to -310 mV. Parts of it drop in the electrolyte, *i.e.* into the diffuse layer with a Debye length of about 3 nm. The potential drop in the area of the discussed surface states is thus smaller than 80 mV while the observed splitting *e.g.* for peak "III" is more than 300 meV. Empty image potential states, which extend into the diffuse layer region, on the other hand, have a typical binding energy of less than 100 meV with respect to the vacuum level and are thus located about 4 eV above the Fermi level.

6.3 Kinetic Reaction Analysis by *in - situ* spectroscopy ellipsometry and Chronoamperometry

As discussed in section 6.1 (Fig.6.3) there exist changes in the RAS transient slope at different processes that occur on the surface. These changes can be studied in more detail using static techniques, such as EIS and CA. The latter allows us to investigate at starting fixed potentials (U_1), promoted surface modifications by induced potential changes from U_1 to U_2, which are generally treated in the following way: a) U_1 should be considered within a region where no adsorption occurs at the copper surface, so there are no visible changes due to surface processes (*e.g.*, adsorption, dissolution, HER, etc.), b) U_2 should be regarded as an overpotential (n) in such a way that it increases (in our case more positive potentials than U_1) within our HER and Cu^{++} dissolution-bounded potential window.

Based on the considerations mentioned above, we used the results of the experiments performed previously, based on *in - situ* EC-STM and EIS techniques. For the latter, a model to describe all the processes that occur due to different relaxation times was employed; and for the ECM, the CPE value was retrieved from the capacitance change obtained at different potentials (potential window). Taking the values for which the capacitance value did not change were corroborated with the help of the *in - situ* EC-STM results; attesting that no adsorption occurs. Based on these observations the value of U_1 was determined for both Cu (111) and Cu (110) (see Figs. 6.11a and 6.11b, respectively). Therefore U_2 was varied to larger values than U_1.

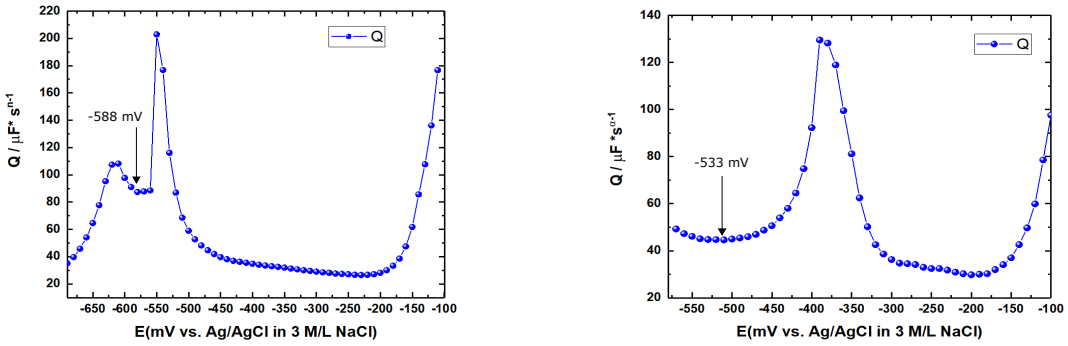

(a) Capacity of Cu (111)

(b) Capacity of Cu (110)

Figure 6.11: Capacity of a) Cu (111) and b) Cu (110), taken from the ECM of the EIS experiments. The arrows indicate the potentials where no adsorption occurs.

Chronoamperometry of Cu (111) and (110)

Taking the experimental data from Figs. 6.11a and 6.11b as a basis to define U_1, we performed CA experiments by jumping from U_1 to U_2 with increments of 10 mV, see Fig. 6.12, which shows that at overpotentials (U_2) near U_1 there is no change (no adsorption occurs), while increasing the overpotential U_2 to more positive values, a potential is reached in which a peak after 3 to 4 seconds appears (red

line in Fig 6.12) because the applied potential U_2 was large enough to observe the adsorption of Cl^-. Following this increase in U_2 it is observed that this hump moves towards shorter times as seen in Fig. 6.12, up to the point where the peak of Cl^- adsorption overlaps with the peak associated to a double layer (helmholtz double layer), which always appeared from U_2 values close to U_1. This peak appears due to the double layer that always forms in our window of potentials. Note that this double layer is formed in time scales of nano-seconds or even less.

These results clearly indicate that Cl^- diffuses from the bulk solution to the copper surface, so that a small overpotential does not occur until the overpotential is large enough to overcome the potential barrier that is needed to adsorb Cl^-.

The same procedure was performed on the Cu (110) sample. The interesting point about this sample is that at overpotentials near to U_1, it behaves similarly as Cu (111), but a peak is never observed to appear at any potential. The only feature that can be observed in that an specific potential (see red dashed line in Fig. 6.13), there is a change in the position of the current, like a step function, and it holds for the rest of the over potentials (U_2) see Fig. 6.13.

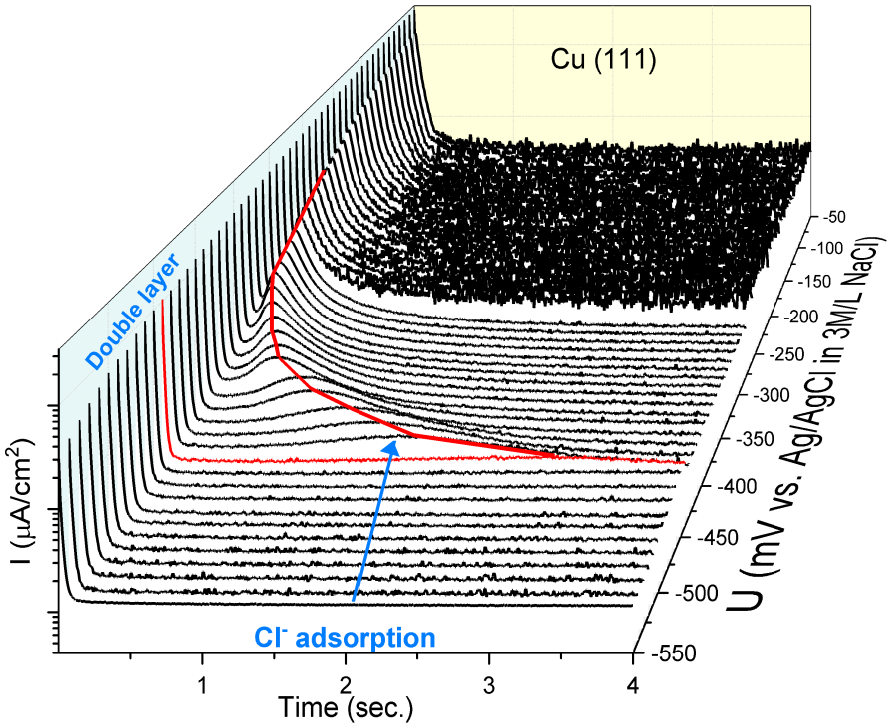

Figure 6.12: Chronoamperometry on Cu (111) surface recorded at different applied potentials as indicated. Thick red line is a guide to the eye that follows the shift of the related Cl^- adsorption when jumping to more positive potentials, while the thin red line indicates the potential at which Cl^- adsorption starts.

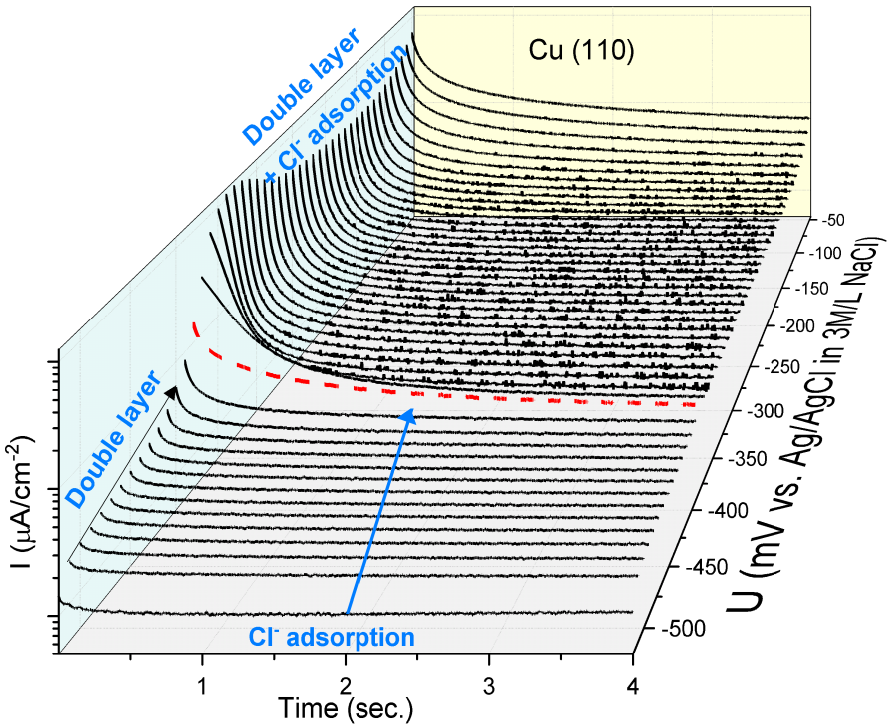

Figure 6.13: Chronoamperometry on Cu (110) surface recorded at different applied potentials as indicated. The red dashed line indicates the potential at which Cl^- adsorption starts, this dashed line indicates a change in the current, like a step function. Contrasting to the Cu (111) case (Fig. 6.12) no peak is observed.

As these experiments were inconclusive, we used *in-situ* ellipsometry. This was motivated by the fact that, among Δ and Ψ parameter measured by ellipsometry, the Δ parameter is extremely sensitive to any change on the surface.

In - situ SE of Cu (111) and (110)

For this experiment U_1 and U_2 were measured during the time that both were applied in order to track changes in Δ since it is very sensitive to superficial changes. The experiment on Cu (111), for which it is clear that during the time potential U_1 is applied there is no change in Δ, neither for overpotentials U_2 near U_1. While for overpotentials U_2 large enough, changes appear that are in agreement with those seen in Fig. 6.12, where the same hump (red line) appears and tracks the same behavior observed in CA.

These results support the theory that holds Cl^- diffuses from bulk solution. It is worth mentioning that the changes in Δ are about 0.8°, and that Δ is proportional to the coverage θ of surface adsorbates or electronic or ionic charges.

The same procedure performed for the copper sample (111) was used for Cu (110), as can be observed in Fig. 6.14 for overpotentials very close to U_1, there is no change in Δ, as expected.

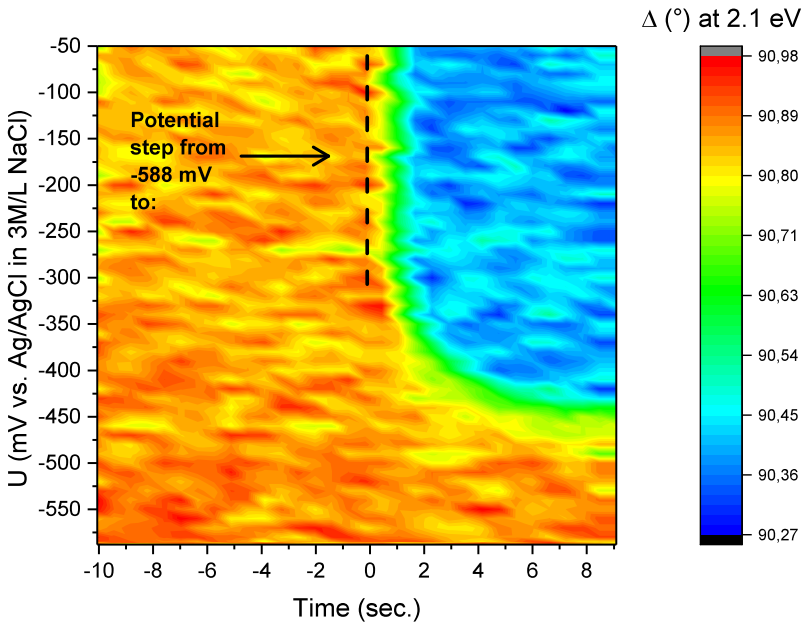

Figure 6.14: Contour plot of Δ parameter measured by kinetic ellipsometry at photon energy of 2.1 eV for Cu (111) in a HCl solution during CA at different applied potentials. The vertical dashed line indicates that from -10 to 0 second correspond to the U_1 (-558 mV). Note the striking similarity in behavior as described in Fig. 6.12.

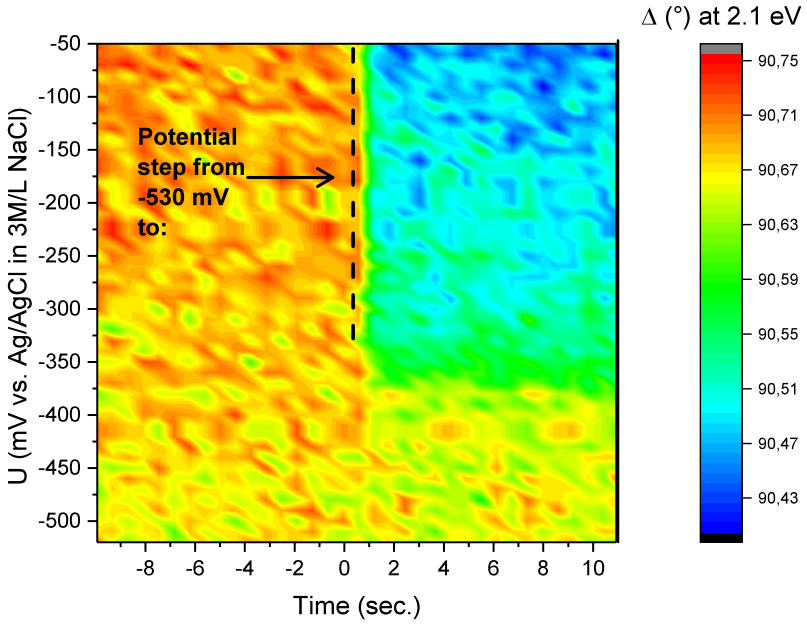

Figure 6.15: Contour plot of Δ parameter measured by kinetic ellipsometry at photon energy of 2.1 eV for Cu (110) in a HCl solution during CA at different applied potentials. The vertical dashed line indicates that from -10 to 0 second correspond to the U_1 (-530 mV). Note also the striking similarity in behavior as described in Fig. 6.13.

.

Until the overpotential is large enough, there is an abrupt change in Δ (Fig.6.15), as observed in CA Fig. 6.13. This change in Δ remains constant at more positive overpotentials. It is worth mentioning that the change in Δ is approximately 0.3 °, giving a better idea of the order/disorder transition when compared to corresponding change observed in Cu (110).

7 Conclusion

7.1 Conclusions and perspectives

In this final part of the thesis, tree main experimental contributions are listed. In essence, at least for the knowledge of the author, in this work a systematic and detailed study of the application of five experimental techniques that complement each other has been employed. The two typical crystalline surfaces Cu (111) and (110) were chosen for which they have been studied in more detail electrochemically at the University Linz. The specific results are as follows:

- Single-wavelength RAS transients were used to investigate the electrochemical adsorption/desorption process on Cu(110) surfaces in hydrochloric acid. It was found that the adsorption/desorption of Cl^- ions and the subsequent surface modifications, reassemble the thermodynamics of Frumkin-type isotherms (Flory-Huggins isotherm statistics). Accordingly, the respective currents as retrieved with CV measurements and the first derivative of the RAS-transients to the potential coincide, a fact that was confirmed theoretically as well as experimentally. Specifically, we detected two anodic and two cathodic adsorption/desorption processes. According to previously reported EC-STM experiments, these four processes are correlate to: (i) the formation of stripes/grooves along [001] direction of Cu(110), and (ii) a faceting of the surface. For the formation of the stripe phase, a numerical analysis based on the Flory-Huggins isotherm statistics reveals an overall attractive lateral interaction between Cl_ adsorbate species. Based on the measured electrochemical current, the surface coverage is less than a monolayer at these potentials (window span of 50 mV). With increasing potentials and coverages, we deduced an overall repulsive interaction between the adsorbates in parallel to the faceting. These, however, overlap strongly and the faceting is barely visible with CV measurements. Additionally, both surface oxidation steps overlap with a Cu([CuCl2]) dissolution, which is superimposed in CV but visible with RAS experiments. In cathodic scans, the atomically clean and ordered surface recovers in two distinct steps: on the one hand, we found a correlation between current peaks measured in CV and the derivative of the RAS-transients, which prove that the electrochemical reactions induce surface modifications. On the other hand, both reactions depended very much on the time for which the Cu surface was kept at potentials with an ongoing [CuCl2] dissolution. Furthermore, we deduced different formation potentials and lateral interaction values in the anodic and cathodic transients, although the scan speed of 1 mV/s is regarded as quasistatic. We conclude that the reaction paths of both, the cathodic defaceting and removal of the stripe structure due to Cl desorption, differ significantly from the anodic reactions, and contains the redeposition of [CuCl2], CuCl aggregates or other species. We conclude that the combination of kinetic RAS and CV is a valuable tool to assess details on the surface modifications

during electrochemical processes, and can even complement other optical approaches, like Raman spectroscopy in electrochemical environments.

- By means of simultaneous electrochemical impedance spectroscopy (EIS) and *in-situ* reflectance anisotropy spectroscopy (RAS) measurements, we could distinguish three thermodynamically stable surface structures of Cu(110) in HCl solution in the electrochemical potential window between the hydrogen evolution reaction (HER) and the dissolution of copper. The three phases are build upon two distinct surface oxidation steps related to the adsorption of Cl. We assign such three phases to specific surface morphologies which have been reported before by means of EC-STM. With increasing anodic potentials, the pristine surface with wide mono atomically flat traces transform first into a stripe/groove like surface morphology along the [001] direction. The latter rows arrange in regular structure with a spacing of 4.6 nm (some of them 2.6 nm). The second resolved oxidation correlates to a faceting of the surface. The EIS experiments clearly demonstrate, however, that the two oxidation steps strongly overlap. The potential of the maximum formation rate are, nevertheless, slightly different (-387 and -352 mV *vs.* Ag/AgCl/3M NaCl). In between we could identify a narrow potential window with thermodynamically stable surface stripes or grooves.

  With a series of RAS spectra around the latter potentials, we could distinguish the anisotropic (opto-electronic) properties of the three phases. At cathodic potentials we obtain a pristine surface but the RAS spectra differ considerably from those measured on pristine surfaces in ultra high vacuum (UHV). The different line shape originates from an inversed surface dipole moment at the respective potentials. The RAS spectra of the pristine as well as the faceted surface show both signatures of surface modified copper bulk resonances. The SDA, which has been calculated from the $\Delta r/r$-RAS spectra, further illustrates the contribution of Drude like free electrons with an anisotropic different effective electron mass and mobility. Misinterpretations regarding SS transitions in some previous publications arise from some similarities of the RAS spectra of the faceted surface to those measured at pristine surfaces in UHV.

  In the very narrow potential window between the two oxidation steps, we could identify at least another three surface resonances, which are not explainable by surface modified bulk transitions. The relatively amplitudes are small but appear reproducible with a Kramers-Kronig consistent line shape. Worth mentioning is the fact that by thermodynamic reasons it seems to be not possible to prepare a homogeneous surface in the respective phase. Part of the surface is already faceted and thus does not contribute to the SS. One of the surface resonance emerges between 2.10 eV and 2.13 eV. Regarding spectral position and line shape, it is very similar to a known surface state resonance which was observed in UHV experiments on the pristine Cu (110) surface. The latter is attributed to a transition between surface states at the $\overline{Y}$ point of the Brillouin zone. We found at least two more surface resonances at higher photon energies *i.e.* at ≈2.28 eV and ≈2.48 eV. The spacing between the transition features agrees well with energy levels of surface states enclosed in 4.6 nm "box". Based on such finding we propose a model containing confined surface states between regular stripes/grooves along the [001] direction. The relatively sharp new features in the $\Delta r/r$-RAS spectra are interpreted as transitions between these states. A possible scenario among others assumes that the ground state of the known occupied surface state remains below the Fermi level. The observed resonances may arise from transitions to the known unoccupied $\overline{Y}$ state which is splitted now in several sub-bands.

A

Optical Analysis

A.1 Appendix

A.1.1 RAS spectrometer optical analysis

The Jones vector of the incident light on the sample, after passing through the polarizer, is:

$$E = \frac{|E|}{\sqrt{2}} \begin{bmatrix} 1 \\ 1 \end{bmatrix} \tag{A.1}$$

where E is the intensity of the photonic electromagnetic field. After being transmitted through the PEM that provides a delay δ, the elliptically polarized beam is represented by the following matrix:

$$\frac{|E|}{\sqrt{2}} \begin{bmatrix} 1 & 0 \\ 0 & e^{-i\delta} \end{bmatrix} \begin{bmatrix} 1 \\ 1 \end{bmatrix} = \frac{|E|}{\sqrt{2}} \begin{bmatrix} 1 \\ e^{-i\delta} \end{bmatrix}. \tag{A.2}$$

Assuming normal incidence, the optical response of the sample surface is characterized by the Jones matrix which is given by:

$$M = \begin{bmatrix} r_1 cos^2\theta + r_2 sen^2\theta & \Delta r sen\theta cos\theta \\ \Delta r sen\theta cos\theta & r_2 cos^2\theta + r_1 sen^2\theta \end{bmatrix} \tag{A.3}$$

where r_1 and r_2 are the complex reflectivities along the two optical axes and θ is the orientation of the optical axis of the sample; in our case, for maximum anisotropy: $\theta = 45°$. The matrix that describes the polarization after reflecting on the surface:

$$\frac{|E|}{2\sqrt{2}} \begin{bmatrix} r_1 + r_2 & \Delta r \\ \Delta r & r_2 + r_1 \end{bmatrix} \begin{bmatrix} 1 \\ e^{i\delta} \end{bmatrix} = \frac{|E|}{2\sqrt{2}} \begin{bmatrix} r_1 + r_2 - \Delta r e^{-i\delta} \\ -\Delta r + (r_2 + r_1)e^{-i\delta} \end{bmatrix}. \tag{A.4}$$

The corresponding Jones matrix describing the light after being transmitted by the analyzer is:

$$S = \frac{|E|}{2\sqrt{2}} \begin{bmatrix} 0 & 1 \end{bmatrix} \begin{bmatrix} r_1 + r_2 - \Delta r e^{-i\delta} \\ -\Delta r + (r_2 + r_1)e^{-i\delta} \end{bmatrix} = \frac{|E|}{2\sqrt{2}} \left[-\Delta r + (r_2 + r_1)e^{-i\delta} \right] \tag{A.5}$$

The intensity reaching the detector is:

$$SS^* = \left[\frac{|E|}{2\sqrt{2}}(-(r_1 - r_2) + (r_2 + r_1)e^{-i\delta}) \right] \left[\frac{|E|}{2\sqrt{2}}(-(\overline{r_1} - \overline{r_2}) + (\overline{r_2} + \overline{r_1})e^{-i\delta}) \right] \tag{A.6}$$

If we define:

$$R = \frac{1}{2} \left[|r_1|^2 + |r_2|^2 \right] \tag{A.7}$$

$$\Delta R = \frac{1}{2} \left[|r_1|^2 - |r_2|^2 \right] \tag{A.8}$$

$$r_1\overline{r_2} - \overline{r_1}r_2 = |r_1||r_2|sen(\theta_1 - \theta_2) \tag{A.9}$$

and assuming that $\theta_1 \approx \theta_2$, we get:

$$\Delta\theta = \theta_1 - \theta_2 \approx 0 \rightarrow sen(\Delta\theta) \approx \Delta\theta \tag{A.10}$$

Simplifying,

$$I(t) = SS^* = \frac{|E|^2}{4} \left[2R + \Delta R cos\delta + R\Delta\theta sen\delta \right] \tag{A.11}$$

The optical signal normalized is therefore:

$$I_N(t) = \frac{|E|^2}{4} \left[2 + \frac{\Delta R}{R} cos\delta + \Delta\theta sen\delta \right] \tag{A.12}$$

The delay imposed by the PEM is of the form $\delta = \pi sen(\omega t)$; and we finally have:

$$I_N(t) = \frac{|E|^2}{4} \left[2 + \frac{\Delta R}{R} cos(\pi sen(\omega t)) + \Delta\theta sen(\pi sen(\omega t)) \right], \tag{A.13}$$

In this last equation, $\Delta R/R$ and $\Delta\theta$, are the real and imaginary part of the overall RAS response.

Let us expand the following therms of Equation A.13

$$cos(xsen\theta) = J_0(x) + 2\sum_{p=1}^{\infty} J_{2p}(x)cos(2p\theta) \tag{A.14a}$$

$$sen(xsen\theta) = 2\sum_{p=0}^{\infty} J_{2p+1}(x)sen[(2p+1)\theta] \tag{A.14b}$$

If we consider Equations A.14a and A.14b, Equation A.13 is reduced to:

$$I_N(t) = \frac{|E|^2}{4}\left[2 + \frac{\Delta R}{R}\left(J_0(\pi) + 2J_2(\pi)cos(2\omega t)\right) + \Delta\theta[2J_1(\pi)sen(\omega t)]\right] \tag{A.15}$$

Therefore, $\frac{\Delta R}{R} = Re\left(\frac{\Delta r}{r}\right)$ is obtained by twice thr frequency of the PEM and $\Delta\theta = Im\left(\frac{\Delta r}{r}\right)$ with the fundamental frequency of the PEM.

The DC detection are typically perform with lock - in techniques or Fourier transform signal processing.

A.1.2 Principles of Spectroscopic Ellipsometry

There are different types of spectroscopic ellipsometry instruments and, depending on the type of the instruments, precision and error in measurements vary. In order to perform appropriate ellipsometry data analysis, it is necessary to understand the characteristics of measurement methods as well. In actual spectroscopic ellipsometry instruments, we need to correct instrument imperfections to minimize measurement errors (calibration of the ellipsometry instrument).

Principles of Ellipsometry Measurement

Here we will see what quantity ellipsometry measures. It is necessary to define the coordinate system in ellipsometry, which is of significant importance for the interpretation of ellipsometry measurements. This appendix introduce the Jones and Mueller matrices corresponding to a measurement sample. As we will see in next section of the appendix, these matrices enable us to describe ellipsometry measurements mathematically.

Measured Values in Ellipsometry

In ellipsometry, p- and s-polarized light waves are irradiated onto a sample at the Brewster angle , and the optical constants and film thickness of the sample is measured from the change in the polarization state by light reflection or transmission. FigureA.1 illustrates the measurement principle of ellipsometry. As we have seen in Chapter 3, the state of polarization is expressed by superimposing waves propagating along two orthogonal axes. In ellipsometry measurement, the polarization states of incident and reflected light waves are described by the coordinates of p- and s-polarizations. The incident vectors E_{ip} and E_{is} in Fig.A.1 are identical to those defined in Fig. 2.15. From comparison with Fig. 2.15, it can be seen that the directions of the electric field vectors for p- and s-polarizations are reversed on both incident and reflection sides in Fig.A.1, in order to make the understanding of ellipsometry easier. When the vectors are defined by the directions shown in Fig.A.1, all the equations described in Chapter 2 remain the same. Notice that the vectors on the incident and reflection sides overlap completely when $\theta = 90°$(straight-through configuration). In Fig.A.1, the incident light is linear polarization oriented at $+45°$relative to the E_{ip} axis. In particular, $E_{ip} = E_{is}$ holds for this polarization since the amplitudes of p- and s-polarizations are the same and the phase difference between the polarizations is zero.

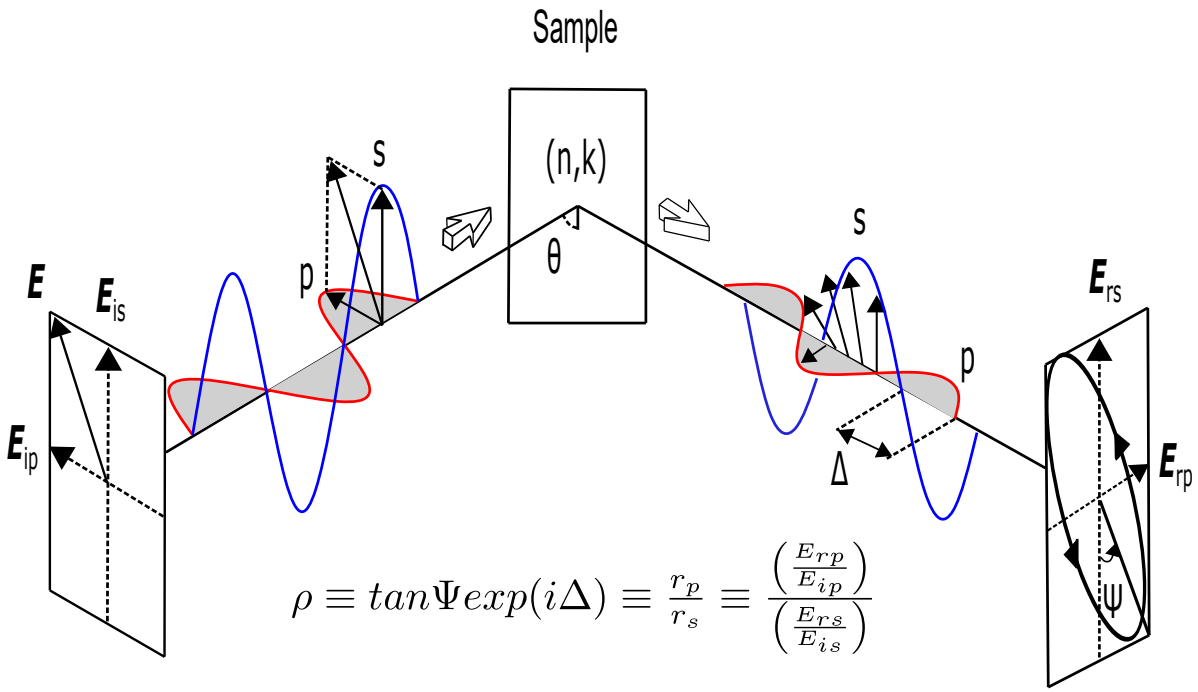

Figure A.1: Measurement Principle SE. Adapted from [32].

The amplitude reflection coefficients for p- and s-polarizations differ significantly due to the difference in electric dipole radiation.Thus, upon light reflection on a sample, p- and s-polarizations show different changes in amplitude and phase. As shown in Fig.A.1, ellipsometry measures the two values (Ψ, Δ) that express the amplitude ratio and phase difference between p- and s-polarizations, respectively. In ellipsometry, therefore, the variation of light reflection with p- and s-polarizations is measured as the change in polarization state. In particular, when a sample structure is simple, the amplitude ratio Ψ is characterized by the refractive index n, while Δ represents light absorption described by the extinction coefficient k. In this case, the two values (n,k) can be determined directly from the two ellipsometry parameters (Ψ, Δ) obtained from a measurement by applying the Fresnel equations. This is the basic principle of ellipsometry measurement. The (Ψ, Δ) measured from ellipsometry are defined from the ratio of the amplitude reflection coefficients for p- and s-polarizations:

$$\rho \equiv tan\Psi exp(i\Delta) \equiv \frac{r_p}{r_s} \tag{A.16}$$

When we measure light transmission, instead of light reflection, (Ψ, Δ) are defined as

$$\rho \equiv tan\Psi exp(i\Delta) \equiv \frac{t_p}{t_s}, \tag{A.17}$$

If we apply the definitions of the amplitude reflection coefficients r_p and r_s, we can rewrite Eq.A.16 as follows:

$$\rho \equiv tan\Psi exp(i\Delta) \equiv \frac{r_p}{r_s} \equiv \frac{\left(\frac{E_{rp}}{E_{ip}}\right)}{\left(\frac{E_{rs}}{E_{is}}\right)}, \tag{A.18}$$

As confirmed from Eq. A.18, r_p and r_s are originally defined by the ratios of reflected electric fields to incident electric fields, and $tan\Psi exp(i\Delta)$ is defined further by the ratio of r_p to r_s. In the case of Fig.A.1, Eq.A.18 can be simplified to $tan\Psi exp(i\Delta) = \frac{E_{rp}}{E_{rs}}$ since $E_{ip} = E_{is}$. In Fig. A.1, therefore, Ψ represents the angle determined from the amplitude ratio between reflected p- and s-polarizations, while Δ expresses the phase difference between reflected p- and s-polarizations. Although Ψ is determined from the 4th quadrant in Fig. A.1. other also provide the same Ψ as Ψ is defined from the absolute value of the amplitude ratio ($0° \leq \Psi \leq 90°$). If we use polar coordinates to represent the amplitude reflection coefficients, it follows from Eq.A.16 that

$$tan\Psi = \frac{|r_p|}{|r_s|} \quad \Delta = \delta_{rp} - \delta_{rs}. \tag{A.19}$$

If we recall that $R_p = |r_p|^2$ and $R_s = |r_s|^2$. We can get the following equation:

$$\Psi = tan^{-1}(|\rho|) = tan^{-1}\left(\frac{|r_p|}{|r_s|}\right) = tan^{-1}\left[\left(\frac{R_p}{R_s}\right)^{1/2}\right]. \tag{A.20}$$

We can obtain Δ from ρ as follows:

$$\Delta = arg(\rho) = \begin{cases} tan^{-1}[Im(\rho)/Re(\rho)] & for\ Re(\rho) > 0, \\ tan^{-1}[Im(\rho)/Re(\rho)] + 180° & for\ Re(\rho) < 0, \quad Im(\rho) \geq 0, \\ tan^{-1}[Im(\rho)/Re(\rho)] - 180° & for\ Re(\rho) < 0, \quad Im(\rho) < 0, \end{cases} \tag{A.21}$$

In Eq. A.21, if $\mathrm{Re}(\rho) = 0$, $\Delta = 90°[Im(\rho) > 0]$ and $\Delta = -90°[Im(\rho) < 0]$. In general, the range of Δ in ellipsometry is expressed by either $-180° \leq \Delta \leq 180°$ or $0° \leq \Delta \leq 360°$. We can convert the range of Δ from $-180° \leq \Delta \leq 180°$ to $0° \leq \Delta \leq 360°$ by simply adding $360°$ to the region of $-180° \leq \Delta \leq 0°$.

The above equation correspond to the ones when the definition of $N \equiv n - ik$ is used. For the definition of $N \equiv n + ik$, we need to rewrite Eq. A.16 as $\rho \equiv tan\Psi exp(i\Delta)$ for the definition of $N \equiv n + ik$.

Coordinate Sysytem in Ellipsometry

When the incident light is linear polarized at $45°(E_{ip} =_{is})$, the (E_x, E_y) coordinates can be transformed easily into the (E_{rp}, E_{rs}) coordinates used in ellipsometry (Fig.A.2). In this case, the representation of the polarization states also holds without any change, except for the coordinate axis conversion of $E_x \longrightarrow E_{rp}$ and $E_y \longrightarrow E_{rs}$. In this conversion, the amplitudes are transformed using $E_{x0} \longrightarrow |r_p|$ and $E_{y0} \longrightarrow |r_s|$ and the initial phases are rewritten as $\delta_x \longrightarrow \delta_{rp}$ and $\delta_y \longrightarrow \delta_{rs}$. In Fig.A.2 represents the polarization states of reflected light waves obtained from this coordinate transformation. The polarization states in ellipsometry measurement can be expressed not only by (Ψ, Δ) but also by the Stokes vectoand (ϵ, θ) coordinates. If we replace $\delta_x - \delta_y$ with Δ, we can understand easily that reflected light becomes

linear polarized when $\Delta = 0°$ and $180°$. On the other hand, reflected light waves become right and left circular polarizations when $\Delta = 90°(270°)$ and $90°$, respectively. In the case of the (ϵ, θ) coordinates, the states of polarization can be expressed easily from the Poincaré sphere, all the elliptical and circular polarizations show counterclockwise rotation. Thus values of the Stokes vectors shown in Fig. A.3 can be obtained easily by substituting the values of (Ψ, Δ) and (ϵ, θ).

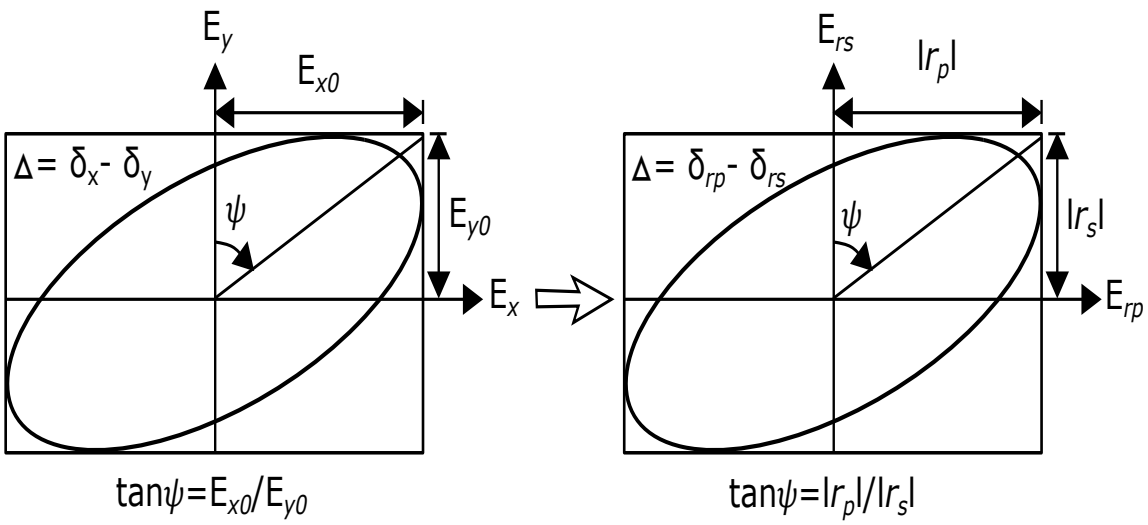

Figure A.2: Coordinate transformation from (a) the (E_x,E_y) coordinates to (b) the (E_{rp}, E_{rs}) coordinates. Adapted from [32].

Polarization	Polarization state	Stoke vectors	$\Psi(\deg)$ $\Delta(\deg)$	$\epsilon(\deg)$ $\theta(\deg)$
Linear polarization oriented at -45°	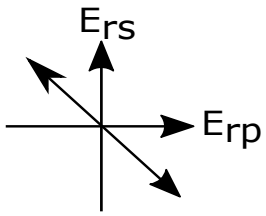	$\begin{bmatrix} 1 \\ 0 \\ -1 \\ 0 \end{bmatrix}$	$\Psi = 45°$ $\Delta = 180°$	$\epsilon = 0°$ $\theta = -45°$
Linear polarization oriented at -65°	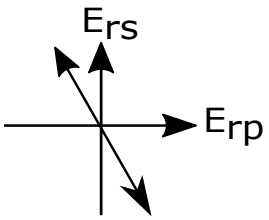	$\begin{bmatrix} 1 \\ -0.643 \\ -0.766 \\ 0 \end{bmatrix}$	$\Psi = 25°$ $\Delta = 180°$	$\epsilon = 0°$ $\theta = -65°$
Right-circular polarization	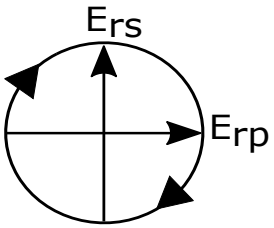	$\begin{bmatrix} 1 \\ 0 \\ 0 \\ 1 \end{bmatrix}$	$\Psi = 45°$ $\Delta = -90°$	$\epsilon = 45°$ $\theta = 0°$
Left-circular polarization	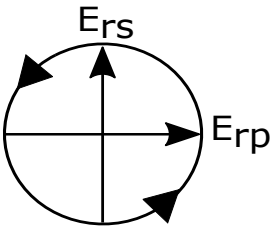	$\begin{bmatrix} 1 \\ 0 \\ 0 \\ -1 \end{bmatrix}$	$\Psi = 45°$ $\Delta = 90°$	$\epsilon = -45°$ $\theta = 0°$
Elliptical polarization (Ψ, Δ)=$(45°, 135°)$	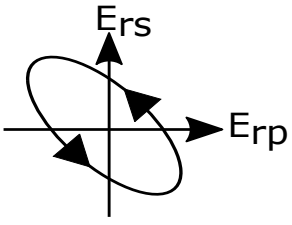	$\begin{bmatrix} 1 \\ 0 \\ -0.707 \\ -0.707 \end{bmatrix}$	$\Psi = 45°$ $\Delta = 135°$	$\epsilon = -22.5°$ $\theta = -45°$

E_{ip} = E_{is} for incident light.

Figure A.3: Representation of the polarization states of reflected light in ellipsometry measurement. Adapted from [32].

Jones and Mueller Matrices of Samples

In ellipsometry measurement, the Jones matrix that corresponds to light reflection by a sample is given by

$$S = \begin{bmatrix} r_p & 0 \\ 0 & r_s \end{bmatrix} \tag{A.22}$$

For example, when linearly polarized light oriented at 45° is reflected by a sample, this light reflection is expressed as

$$\begin{bmatrix} E_{rp} \\ E_{rs} \end{bmatrix} = \begin{bmatrix} r_p & 0 \\ 0 & r_s \end{bmatrix} \begin{bmatrix} E_{ip} \\ E_{is} \end{bmatrix} = \begin{bmatrix} rp \\ rs \end{bmatrix} \tag{A.23}$$

In the above calculation, $E_{ip} = E_{is} = 1$ is assumed Eq.A.23 shows the straightforward fact that the incident waves E_{ip} and E_{is} are reflected by a sample with the coefficients of r_p and r_s, respectively. Notice that A.23 represents the light reflection illustrated in Fig. A.1. A similar calculation can also be performed using the Muller matrix. If we use Eq. A.16, Eq. A.22 can be rewritten as

$$S = r_s \begin{bmatrix} r_p/r_s & 0 \\ 0 & 1 \end{bmatrix} = r_s \begin{bmatrix} tan\Psi exp(i\Delta) & 0 \\ 0 & 1 \end{bmatrix} = \frac{r_s}{cos\Psi} \begin{bmatrix} sin\Psi exp(i\Delta) & 0 \\ 0 & cos\Psi \end{bmatrix} \tag{A.24}$$

From Eq. A.23, it is obvious that

$$E_{rp} = r_p \quad E_{rs} = r_s. \tag{A.25}$$

If we substitute $E_x = E_{rp} = r_p$ and $E_y = E_{rs} = r_s$ into (Electric field B), we can express the normalized Stokes parameter using the amplitude reflection coefficients as follows:

$$\frac{S_1}{S_0} = \frac{r_p r_p^* - r_s r_s^*}{r_p r_p^* + r_s r_s^*} \tag{A.26a}$$

$$\frac{S_2}{S_0} = \frac{2Re(r_p^* r_s)}{r_p r_p^* + r_s r_s^*} \tag{A.26b}$$

$$\frac{S_3}{S_0} = \frac{2Im(r_p^* r_s)}{r_p r_p^* + r_s r_s^*} \tag{A.26c}$$

Conversely, using [(Ψ, Δ) system], we can calculate (Ψ, Δ) values from the Stokes parameters:

$$\Psi = \frac{1}{2} cos^{-1}\left(\frac{-S_1}{S_0}\right) \tag{A.27a}$$

$$\Delta = \begin{cases} tan^{-1}(-S_3/S_2) & for \quad cos\Delta > 0, \\ tan^{-1}(-S_3/S_2) + 180° & for \quad cos\Delta < 0, \quad sin\Delta \geq 0, \\ tan^{-1}(-S_3/S_2) - 180° & for \quad cos\Delta < 0, \quad sin\Delta < 0, \end{cases} \tag{A.27b}$$

In Eq. A.27b, when cos$\Delta = 0$, it follows that $\Delta = 90°(sin\Delta > 0)$ and $\Delta = -90°(sin\Delta < 0)$. The Jones matriz shows in Eq. A.22 represents the light reflection by an optically isotropic sample. When a sample shows optical anisotropy including birefringence and dichroism, the Jones matrix corresponding to a sample is described by the following matrix:

$$S_{ani} = \begin{bmatrix} r_{pp} & r_{ps} \\ r_{sp} & r_{ss} \end{bmatrix} \tag{A.28}$$

It can be seen from Eq.A.28 that the off-diagonal elements of the Jones matrix are no longer zero in samples that show optical anisotropy. Accordingly, the characterization of anisotropic samples generally becomes complicated.

Bibliography

[1] EE Barritt, CI Smith, DS Martin, K Gentz, K Wandelt, and P Weightman. Evidence for the observation of surface states at the cu (110)/electrolyte interface. *EPL (Europhysics Letters)*, 92(5):57005, 2010.

[2] K Hingerl, RE Balderas-Navarro, A Bonanni, and D Stifter. Influence of anisotropic in−plane strain on critical point resonances in reflectance difference data. *Journal of Vacuum Science & Technology B: Microelectronics and Nanometer Structures Processing, Measurement, and Phenomena*, 19(4):1650–1657, 2001.

[3] LF Lastras-Martínez, RE Balderas-Navarro, A Lastras-Martínez, and K Hingerl. Stress-induced optical anisotropies measured by modulated reflectance. *Semiconductor science and technology*, 19(9):R35, 2004.

[4] RE Balderas-Navarro, NA Ulloa-Castillo, K Arimoto, G Ramírez-Meléndez, LF Lastras-Martínez, H Furukawa, J Yamanaka, A Lastras-Martínez, JM Flores-Camacho, N Usami, et al. Reflectance anisotropies of compressively strained si grown on vicinal si 1- x c x (001). *Applied Physics Letters*, 102(1):011902, 2013.

[5] VL Berkovits, IV Makarenko, TA Minashvili, and VI Safarov. Optical transitions on gaas [110] surface. *Solid state communications*, 56(5):449–450, 1985.

[6] A Lastras-Martınez, RE Balderas-Navarro, and LF Lastras-Martınez. Linear electro-optic reflectance modulated spectra of gaas (001) around e1 and e1+ δ1. *Thin Solid Films*, 373(1-2):207–210, 2000.

[7] Miao-Hsuan Chien, Saul Vazquez-Miranda, Reza Sharif, Kurt Hingerl, and Christoph Cobet. In situ optical quantification of adsorbates and surface charges on copper crystals and their impact on the hydrogen evolution reaction in hydrochloric electrolytes. *The Journal of Physical Chemistry C*, 122(16):8984–8997, 2018.

[8] Richard C Alkire, Dieter M Kolb, Jacek Lipkowski, and Phil N Ross. *Diffraction and spectroscopic methods in electrochemistry*, volume 18. John Wiley & Sons, 2006.

[9] Dieter Landolt. *Corrosion and surface chemistry of metals*. CRC press, 2007.

[10] Itaru Kamiya, DE Aspnes, H Tanaka, LT Florez, JP Harbison, and R Bhat. Surface science at atmospheric pressure: reconstructions on (001) gaas in organometallic chemical vapor deposition. *Physical review letters*, 68(5):627, 1992.

[11] Knut Deppert, J Jonsson, and Lars Samuelson. Application of reflectance difference to monitor gaas wet etching. *Semiconductor science and technology*, 9(5):1148, 1994.

[12] V. L. Berkovits, A. O. Gusev, V. M. Lantratov, T. V. L'vova, A. B. Pushnyi, V. P. Ulin, and D. Paget. Photoinduced formation of dimers at a liquid/(001)gaas interface. *Phys. Rev. B*, 54:R8369–R8372, Sep 1996.

[13] B Sheridan, DS Martin, JR Power, SD Barrett, CI Smith, CA Lucas, RJ Nichols, and P Weightman. Reflection anisotropy spectroscopy: A new probe for the solid-liquid interface. *Physical review letters*, 85(21):4618, 2000.

[14] HL Messiha, CI Smith, NS Scrutton, and P Weightman. Evidence for protein conformational change at a au (110)/protein interface. *EPL (Europhysics Letters)*, 83(1):18004, 2008.

[15] Hans Lomholt Skriver and NM Rosengaard. Surface energy and work function of elemental metals. *Physical Review B*, 46(11):7157, 1992.

[16] Glenn A Burdick. Energy band structure of copper. *Physical Review*, 129(1):138, 1963.

[17] Sun Lidong. *Optical Anisotropy of Cu(110) Surface and Its Application to Surface Analysis*. PhD thesis, Johannes Kepler University, Altenbergerstrasse 69, 4040 Linz, Austria, 2002.

[18] J Harl, G Kresse, LD Sun, M Hohage, and P Zeppenfeld. Ab initio reflectance difference spectra of the bare and adsorbate covered cu (110) surfaces. *Physical Review B*, 76(3):035436, 2007.

[19] Richard P Olenick, Tom M Apostol, and David L Goodstein. *Beyond the mechanical universe: from electricity to modern physics*. Cambridge University Press, 1986.

[20] Wolfgang Schmickler and Elizabeth Santos. *Interfacial electrochemistry*. Springer Science & Business Media, 2010.

[21] Bockris JO'M, Maria Gamboa-Aldeco, and M Szklarczyk. Ionic adsorption at the solidsolution interphase using three in situ methods. *Journal of Electroanalytical Chemistry*, 339(1-2):355–400, 1992.

[22] Larry R Faulkner and Allen J Bard. *Electrochemical methods: fundamentals and applications*. John Wiley and Sons, 2002.

[23] LI Daikhin, AA Kornyshev, and M Urbakh. Double layer capacitance on a rough metal surface: surface roughness measured by debye ruler. *Electrochimica acta*, 42(19):2853–2860, 1997.

[24] Jun-Sheng Yu and Zu-Xun Zhang. Double potential-step chronoamperometry and chronocoulometry at an ultramicrodisk electrode: Theory and experiment. *Journal of Electroanalytical Chemistry*, 439(1):73–80, 1997.

[25] Sambhaji M Pawar, Jongmin Kim, Akbar I Inamdar, Hyeonseok Woo, Yongcheol Jo, Bharati S Pawar, Sangeun Cho, Hyungsang Kim, and Hyunsik Im. Multi-functional reactively-sputtered copper oxide electrodes for supercapacitor and electro-catalyst in direct methanol fuel cell applications. *Scientific reports*, 6:21310, 2016.

[26] DE Aspnes. Above-bandgap optical anisotropies in cubic semiconductors: A visible–near ultraviolet probe of surfaces. *Journal of Vacuum Science & Technology B: Microelectronics Processing and Phenomena*, 3(5):1498–1506, 1985.

[27] Hinds Instruments. Pem-90 photoelastic modulators. *PEMlabs, Hind Instruments, Inc.[Online]. Available: http://www. hindspem. com/media/PEM100% 20Brochure. pdf*, 2006.

[28] JDE McIntyre and David E Aspnes. Differential reflection spectroscopy of very thin surface films. *Surface Science*, 24(2):417–434, 1971.

[29] DS Martin, NP Blanchard, P Weightman, DS Roseburgh, RJ Cole, J-K Hansen, J Bremer, and O Hunderi. Optical reflectance anisotropy of ag (110): Evidence for contributions from surface-modified bulk band transitions. *Physical Review B*, 76(11):115403, 2007.

[30] IK Kim and DE Aspnes. Toward n κ d spectroscopy: Analytic solution of the three-phase model of polarimetry in the thin-film limit. *Applied physics letters*, 88(20):201107, 2006.

[31] G Chiarotti, P Chiaradia, C Goletti, and F Arciprete. Optical properties of semiconductor surfaces. In *EPIOPTICS 2000*, pages 24–38. World Scientific, 2001.

[32] Hiroyuki Fujiwara. *Spectroscopic ellipsometry: principles and applications*. John Wiley & Sons, 2007.

[33] C Kittel. Introduction to solid state physics, 6th edn., translated by y. *Uno, N. Tsuya, A. Morita and J. Yamashita,(Maruzen, Tokyo, 1986) pp*, pages 124–129, 1986.

[34] David E Aspnes. Optical properties of thin films. *Thin solid films*, 89(3):249–262, 1982.

[35] Goran A Niklasson, CG Granqvist, and O Hunderi. Effective medium models for the optical properties of inhomogeneous materials. *Applied Optics*, 20(1):26–30, 1981.

[36] DE Aspnes, JB Theeten, and F Hottier. Investigation of effective-medium models of microscopic surface roughness by spectroscopic ellipsometry. *Physical Review B*, 20(8):3292, 1979.

[37] H Fujiwara, Joohyun Koh, PI Rovira, and RW Collins. Assessment of effective-medium theories in the analysis of nucleation and microscopic surface roughness evolution for semiconductor thin films. *Physical Review B*, 61(16):10832, 2000.

[38] Joungchel Lee, RW Collins, VS Veerasamy, and J Robertson. Analysis of amorphous carbon thin films by spectroscopic ellipsometry. *Journal of non-crystalline solids*, 227:617–621, 1998.

[39] S Van Gils, C Le Pen, A Hubin, H Terryn, and E Stijns. Electropolishing of copper in h3po4 ex situ and in situ optical characterization. *Journal of The Electrochemical Society*, 154(3):C175–C180, 2007.

[40] Achim Walter Hassel, Koji Fushimi, and Masahiro Seo. An agar-based silver— silver chloride reference electrode for use in micro-electrochemistry. *Electrochemistry communications*, 1(5):180–183, 1999.

[41] Harland Tompkins and Eugene A Irene. *Handbook of ellipsometry*. William Andrew, 2005.

[42] Hong Zhao, Jinho Chang, Aliaksei Boika, and Allen J Bard. Electrochemistry of high concentration copper chloride complexes. *Analytical chemistry*, 85(16):7696–7703, 2013.

[43] JJ Fritz. Chloride complexes of copper (i) chloride in aqueous solution. *The Journal of Physical Chemistry*, 84(18):2241–2246, 1980.

[44] I Puigdomenech and C Taxén. Thermodynamic data for copper. *Implications for the corrosion of copper under repository conditions. Swedish Nuclear Fuel and Waste Management Company Report*, pages 00–13, 2000.

[45] Björn Beverskog, Ignasi Puigdomenech, and Studsvik Eco. *Pourbaix diagrams for the system copper-chlorine at 5-100 C*. Citeseer, 1998.

[46] Roger Parsons. Marcel pourbaix, lectures on electrochemical corrosion, plenum press, new york and london (1973), 1974.

[47] M Pourbaix. Recent applications of electrode potential measurements in the thermodynamics and kinetics of corrosion of metals. *Corrosion*, 25(6):267–284, 1969.

[48] M Kruft, B Wohlmann, C Stuhlmann, and K Wandelt. Chloride adsorption on cu (111) electrodes in dilute hcl solutions. *Surface science*, 377:601–604, 1997.

[49] S. Vazquez-Miranda, V. Solokha, R. E. Balderas-Navarro, K. Hingerl, and C. Cobet. Adsorbate Isotherm Analysis by Reflection Anisotropy Spectroscopy on Copper (110) in Hydrochloric Acid. *J. Phys. Chem. C*, 124:5204–5212, 2020.

[50] Gholamreza Barati, Vladyslav Solokha, Klaus Wandelt, Kurt Hingerl, and Christoph Cobet. Chloride-induced morphology transformations of the cu (110) surface in dilute hcl. *Langmuir*, 30(48):14486–14493, 2014.

[51] Klaus Kern, Horst Niehus, Axel Schatz, Peter Zeppenfeld, Jürgen Goerge, and George Comsa. Long-range spatial self-organization in the adsorbate-induced restructuring of surfaces: Cu {100}-(2× 1) o. *Physical review letters*, 67(7):855, 1991.

[52] BV Andryushechkin, VV Cherkez, TV Pavlova, GM Zhidomirov, and KN Eltsov. Structural transformations of cu (110) surface induced by adsorption of molecular chlorine. *Surface Science*, 608:135–145, 2013.

[53] C Goletti, Gianlorenzo Bussetti, A Violante, B Bonanni, M Di Giovannantonio, G Serrano, S Breuer, K Gentz, and K Wandelt. Cu (110) surface in hydrochloric acid solution: Potential dependent chloride adsorption and surface restructuring. *The Journal of Physical Chemistry C*, 119(4):1782–1790, 2015.

[54] Hans Joachim Lewerenz. On the structure of the helmholtz layer and its implications on electrode kinetics. *ECS Transactions*, 50(52):3–20, 2013.

[55] P Weightman, DS Martin, RJ Cole, and T Farrell. Reflection anisotropy spectroscopy. *Reports on Progress in Physics*, 68(6):1251, 2005.

[56] D. E. Aspnes. Spectroscopic Ellipsometry of Solids. In B. Seraphin, editor, *Opt. Prop. Solids - New Dev.*, chapter 15, pages 799–846. North-Holland, Amsterdam, 1976.

[57] D. E. Aspnes, A. A. Studna, L. T. Florez, Y. C. Chang, J. P. Harbison, M. K. Kelly, and H. H. Farrell. Temporal and spectral dependences of the anisotropic dielectric responses of singular and vicinal (001) GaAs surfaces during interrupted molecular-beam epitaxy growth. *J. Vac. Sci. Technol. B*, 7(4):901–906, 1989.

[58] R. A. Synowicki, G. K. Pribil, G. Cooney, C. M. Herzinger, S. E. Green, R. H. French, M. K. Yang, J. H. Burnett, and S. Kaplan. Fluid refractive index measurements using rough surface and prism minimum deviation techniques. *J. Vac. Sci. Technol. B*, 22(6):3450–3453, 2004.

[59] Otto Wiener. Die theorie des mischkorpers fur das feld der stationaren stromung. *Abhandlungen der Sachsischen Gesellschaft der Akademischen Wissenschaften in Mathematik und Physik*, 32:507–604, 1912.

[60] Roger Jansson and Hans Arwin. Selection of the physically correct solution in the n-media bruggeman effective medium approximation. *Optics communications*, 106(4-6):133–138, 1994.

[61] Harald Ibach. *Physics of surfaces and interfaces*, volume 12. Springer, 2006.

[62] M. Denk, M. Hohage, L.D. Sun, P. Zeppenfeld, N. Esser, and C. Cobet. Reflectance difference spectroscopy of water on Cu(110). *Surf. Sci.*, 627:16–22, sep 2014.

[63] A. Baghbanpourasl, W. G. Schmidt, M. Denk, C. Cobet, M. Hohage, P. Zeppenfeld, and K. Hingerl. Water adsorbate influence on the Cu(110) surface optical response. *Surf. Sci.*, 641:231–236, 2015.

[64] C Deslouis, OR Mattos, MM Musiani, and B Tribollet. Comments on mechanisms of copper electrodissolution in chloride media. *Electrochimica acta*, 38(18):2781–2783, 1993.

[65] Y. Gründer, a. Drünkler, F. Golks, G. Wijts, J. Stettner, J. Zegenhagen, and O. M. Magnussen. Cu(111) in Chloride Containing Acidic Electrolytes: Coadsorption of an Oxygenated Species. *Journal of Electroanalytical Chemistry*, 712:74–81, jan 2014.

[66] B. Cord, R. Courths, and H. Wern. Observation of new surface states on Cu(110) with the use of angle-resolved photoelectron spectroscopy. *Phys. Rev. B*, 31(2):1164–1167, 1985.

[67] A. Goldmann, V. Dose, and G. Borstel. Empty electronic states at the (100), (110), and (111) surfaces of nickel, copper, and silver. *Phys. Rev. B*, 32(4):1971–1980, 1985.

[68] E. E. Barritt, C. I. Smith, D. S. Martin, K. Gentz, K. Wandelt, and P. Weightman. Optical response of the Cu(110)/electrolyte interface. *J. Phys. Conf. Ser.*, 286:012028, mar 2011.

[69] K Stahrenberg, Th Herrmann, N Esser, and W Richter. Surface optical properties of clean cu (110) and cu (110)-(2× 1)-o. *Physical Review B*, 61(4):3043, 2000.

[70] L. D. Sun, M. Hohage, P. Zeppenfeld, and R. E. Balderas-Navarro. Origin and temperature dependence of the surface optical anisotropy on Cu(110). *Surf. Sci.*, 589(1-3):153–163, sep 2005.

[71] V. Mazine and Y. Borensztein. Monitoring the Transitions of the Charge-Induced Reconstruction of Au(110) by Reflectance Anisotropy Spectroscopy. *Phys. Rev. Lett.*, 88(14):147403, mar 2002.

[72] P. Weightman, C. Smith, D. S. Martin, C. Lucas, R. Nichols, and S. Barrett. Comment on Monitoring the Transitions of the Charge-Induced Reconstruction of Au(110) by Reflection Anisotropy Spectroscopy. *Phys. Rev. Lett.*, 92(19):199707, may 2004.

[73] D. M. Kolb, W. Boeck, K.-M. Ho, and S. Liu. Observation of Surface States on Ag(100) by Infrared and Visible Electroreflectance Spectroscopy. *Phys. Rev. Lett.*, 47(26):1921–1924, dec 1981.

[74] Li-Jun Wan and Kingo Itaya. In situ scanning tunneling microscopy of cu (110): atomic structures of halide adlayers and anodic dissolution. *Journal of Electroanalytical Chemistry*, 473(1-2):10–18, 1999.

[75] Mark E Orazem and Bernard Tribollet. *Electrochemical impedance spectroscopy*. John Wiley & Sons, 2017.

[76] AS Bondarenko and GA Ragoisha. Progress in chemometrics research. *Nova Science Publishers, New York*, pages 89–102, 2005.

[77] Jakub Tymoczko, Viktor Colic, Aliaksandr S Bandarenka, and Wolfgang Schuhmann. Detection of 2d phase transitions at the electrode/electrolyte interface using electrochemical impedance spectroscopy. *Surface Science*, 631:81–87, 2015.

[78] T Pajkossy and DM Kolb. Anion-adsorption-related frequency-dependent double layer capacitance of the platinum-group metals in the double layer region. *Electrochimica acta*, 53(25):7403–7409, 2008.

[79] AJ Motheo, A Sadkowski, and RS Neves. Electrochemical immittance spectroscopy applied to the study of the single crystal gold/aqueous perchloric acid interface. *Journal of Electroanalytical Chemistry*, 430(1-2):253–262, 1997.

[80] S. Huemann, N. T. M. Hai, P. Broekmann, K. Wandelt, H. Zajonz, H. Dosch, and F. Renner. X-ray diffraction and STM study of reactive surfaces under electrochemical control: Cl and I on Cu(100). *J. Phys. Chem. B*, 110(49):24955–24963, dec 2006.

[81] Y. Gründer, D. Kaminski, F. Golks, K. Krug, J. Stettner, O. M. Magnussen, a. Franke, J. Stremme, and E. Pehlke. Reversal of chloride-induced Cu(001) subsurface buckling in the electrochemical environment: An in situ surface x-ray diffraction and density functional theory study. *Phys. Rev. B*, 81(17):174114, may 2010.

[82] D. Martin, A. Maunder, and P. Weightman. Thermal behavior of the Cu(110) surface studied by reflection anisotropy spectroscopy and scanning tunneling microscopy. *Phys. Rev. B*, 63(15):1–8, mar 2001.

[83] P. Hofmann, K. C. Rose, V. Fernandez, A. M. Bradshaw, and W. Richter. Study of Surface States on Cu(110) Using Optical Reflectance Anisotropy. *Phys. Rev. Lett.*, 75(10):2039–2042, sep 1995.

[84] L. Campanella. Zero charge potential of metals. *J. Electroanal. Chem. Interfacial Electrochem.*, 28(1):228–232, 1970.

[85] M. L. Foresti, G. Pezzatini, and M. Innocenti. Electrochemical behaviour of the Cu(110)—water interface. *J. Electroanal. Chem.*, 434(1-2):191–200, 1997.

[86] B. Ter-Ovanessian, C. Alemany-Dumont, and B. Normand. Single frequency electrochemical impedance investigation of zero charge potential for different surface states of Cu-Ni alloys. *J. Appl. Electrochem.*, 44(3):399–410, 2014.

[87] Theodor Herrmann. *Optische Spektroskopie an Metallen und ferromagnetischen Filmen.* Doktorarbeit, Technischen Universitt Berlin, 2010.

[88] J.-K. Hansen, J. Bremer, and O. Hunderi. The electronic structure of Cu(110) and Ag(110) surfaces studied by reflection anisotropy spectroscopy. *Surf. Sci.*, 418:L58–L61, 1998.

[89] U. Rossow, L. Mantese, and D. E. Aspnes. Interpretation of surface-induced optical anisotropy of clean, hydrogenated, and oxidized vicinal silicon surfaces investigated by reflectance-difference spectroscopy. *J. Vac. Sci. Technol. B*, 14(4):3070–3074, 1996.

[90] L. D. Sun, M. Hohage, P. Zeppenfeld, R. E. Balderas-Navarro, and K. Hingerl. Surface-induced d-band anisotropy on Cu(110). *Surf. Sci.*, 527(1-3):L184–L190, mar 2003.

[91] K. Stahrenberg, Th. Herrmann, K. Wilmers, N. Esser, W. Richter, and M. Lee. Optical properties of copper and silver in the energy range 2.5-9.0 eV. *Phys. Rev. B*, 64(11):115111, aug 2001.

[92] LD Sun, M Hohage, P Zeppenfeld, and RE Balderas-Navarro. Rds investigation of adsorption and surface ordering processes on cu (110). *physica status solidi (c)*, 0(8):3022–3026, 2003.

[93] M. Nagira, M. Sawada, M. Higashiguchi, K. Yaji, T. Moko, T. Ueno, U. Miura, K. Shimada, A. Kimura, H. Namatame, and M. Taniguchi. Surface quantum well state at the striped Cu(1 1 0)(2 1)O surface studied by angle resolved photoemission spectroscopy. *Surf. Sci.*, 601(18):4041–4044, 2007.

[94] L. D. Sun, M. Hohage, and P. Zeppenfeld. Oxygen-induced reconstructions of Cu(110) studied by reflectance difference spectroscopy. *Phys. Rev. B*, 69(4):1–6, 2004.

List of Figures

List of Tables